Accessing the Tribological Contact on the Nanoscale by means of Scanning Probe Techniques

Dissertation
zur Erlangung des akademischen Grades
DOKTOR-INGENIEUR

vorgelegt von
M. Tech. Aditya Kumar
aus Indien

eingereicht dem
Department Maschinenbau
der Universität Siegen

Referent: Univ.- Prof. Dr. rer. nat. habil. X. Jiang
Korreferent: Univ. - Prof. Dr. -Ing. habil. C. Zhang

April 2012

Zusammenfassung

Tribologie ist ein Forschungsfeld, das für eine lange Zeit aktiv erforscht wurde, aber nur wenig grundlegendes Verständnis der verschiedenen Beobachtungen erreicht wurde. Der Hauptgrund dafür liegt in der enormen Komplexität der Phänomene, die auf die Kräfte zwischen zwei sich gegeneinander bewegende Körper im Kontakt zurückgeführt werden kann. Allerdings erfordert die zentrale Rolle der Tribologie in der modernen Gesellschaft eine Forschung in diesem interdisziplinären Feld im Rahmen der Optimierung der Leistung sowie der Lebensdauer vieler Produkte. Der heutige technologische Fortschritt in der Raster-Sonden- Technik eröffnet die Möglichkeit, Kontakt-Phänomene im Bereich einzelner Oberflächenunebenheiten zu studieren. In dieser Arbeit wurden die Einflüsse von Oberflächenrauheit, mechanische Eigenschaften, Adhäsionskräfte und externe Parameter (verwendete Normallast, Kratz-Geschwindigkeit und Belastungsraten) auf die Reibung identifiziert.

In dieser Arbeit wurden mit Hilfe der Rasterkraftmikroskopie (AFM) Adhäsionskräfte zwischen unterschiedlich großen Siliziumdioxid-Mikrometer Kugeln und verschiedenen rauen Oberflächen (Silizium und Diamant-Kohlenstoff (DLC)) gemessen. Die Oberflächenrauigkeit, Rauigkeit Geometrie und die Größe der haftenden Partikel spielen eine entscheidende Rolle um die Adhäsionskräfte zu bestimmen. Die Adhäsionskraft steigt linear mit der Größe der haftenden Partikel für glatte Oberflächen. Die anfängliche Adhäsionskraft nimmt mit steigender Oberflächenrauheit ab und steigt anschließend. Die Ergebnisse wurden mit bereits bestehenden und vorgeschlagenen Modellen verglichen.

Es wird experimentell der Einfluss der angewandten Normallast auf das tribologische Verhalten von kugelförmiger Sonde auf verschieden rauen Oberflächen (Quarzglas, Aluminium, DLCs und Si-CBNO Beschichtungen) mittels Nanoindenter und AFM untersucht. Der Reibungskoeffizient nimmt in einem ausreichend niedrigen Normallastbereich ab, wobei der Kontakt elastisch ist. Jedoch, mit einer erhöhten normalen Belastung umfasst der Kontakt eine plastische Verformung und der Reibungskoeffizient ist konstant mit zunehmender Last gefolgt von einem steigenden Reibungskoeffizienten. Die Oberflächenrauigkeit und die mechanischen Eigenschaften (Härte und Elastizitätsmodul) haben signifikanten Einfluss auf die Reibung, da sie den Anteil der plastischen Verformung bestimmen. Eine zusätzliche laterale Kraft verursacht von intrinsischer Adhäsionskraft ist zu erkennen. Nach dem Entfernen des zusätzlichen Adhäsionskraft-Faktors ist der

Reibungskoeffizient konstant bei einer ausreichend niedrigen aufgebrachten Normallast im elastischen Kontaktbereich. Allerdings, beinhaltet der Kontakt mit einer erhöhten normalen Belastung eine plastische Verformung und der Reibungskoeffizient nimmt mit steigender Normallast zu. Der Reibungskoeffizient steigt mit Verringerung der Belastungsrate und Kratzgeschwindigkeit. Der kritische Lastbereich für den Übergang von vorwiegend elastisch zu elastisch-plastischen Kontakt oder elastisch- plastischen zu vorwiegend plastischer Kontakt zwischen dem Indenter und der Probe steigt mit zunehmender Größe der Spitze und der Kratzgeschwindigkeit und nimmt ab mit der Oberflächenrauigkeit und der Belastungsrate. Die Ergebnisse wurden mit bestehenden Modellen verglichen.

Acknowledgements

There are lots of people I would like to thank for a huge variety of reasons.

Firstly, I would like to express my deepest gratitude and indebtness to my thesis supervisors, **Prof. Jiang** and **Dr. Staedler**, who have the attitude and substance of genius; they continually and convincingly conveyed a spirit of adventure and excitement in regard to research with a positive and methodological approach and timely constructive criticisms. But, the words of thanks will not be and should not be complete, if I do not appreciate the steerings towards life that they have rendered me; their perceptions and mentations will always be an invaluable asset to me throughout my life.

I would next like to render my sincere thanks to **Prof. Zhang** for readily agreeing to be a co-referee for my thesis. I would also like to thank **Prof. Weinberg** and **Prof. Fritzen** for readily accepting to be my examiners. The help extended by all of my colleagues at LOT, University of Siegen is greatly appreciated. Special thanks should be given to **Srikanth** for the spirit he incited in our lab. I am very much thankful to my project mates, **Carsten**, **Jan**, and **Regina** for creating an exceptionally friendly atmosphere in the lab and for their cooperation and support till the submission of my thesis. I am very grateful to **Thomas**, **Petra**, and **Claudia** for their help and cooperation for my day to day lab activities. Thanks to **Mrs. Faber** and **Andrea** for their help in all the administrative works. Thanks also to **Michael**, **Jing**, **Zhang Lei**, and other LOT members for their help and moral support. Inexpressible, still I utter my thanks to my dear friends **Shabi**, **Majid**, and **Sanjib** who have shared my joys and sorrows during my stay at Siegen. I would like to say a big ‘thank-you’ to all my Siegen friends and to all those who made my moments here memorable, and I will never forget the affection shown to me.

I cannot end without thinking my family, on whose constant love and blessings, I have always relied upon and I hope to continue, in my small way, like this.

Publications and Conferences

1. J. Shi, A. Kumar, L. Zhang, X. Jiang, Z.L. Pei, J. Gong, C. Sun, Effect of Cu addition on properties of Ti-Al-Si-N nanocomposite films deposited by cathodic vacuum arc ion plating, Surface Coating and Technology 206, Issues 11-12, (2012), 2947-2953.
2. H. Abu Samra, A. Kumar, J. Xia, T. Staedler, X. Jiang, R. Verucchi, and I. Aronov, Development of a new generation of amorphous hard coatings based on the Si-B-C-N-O system for applications in extreme condition, Surface Engineering, Nov 2011 (in Press).
3. Z. Q. Yao, B. He, L. Zhang, C. Q. Zhuang, T. W. Ng, S. L. Liu, M. Vogel, A. Kumar, W. J. Zhang, C. S. Lee, S. T. Lee, and X. Jiang, Energy band engineering and controlled p-type conductivity of CuAlO2 thin Films by nonisovalent Cu-O alloying, Applied Physics Letters 100, (2012), 062102-1-4.
4. Aditya Kumar, Thorsten Staedler, and Xin Jiang, Role of relative size of surface asperity and adhering particle on adhesion force, manuscript under preparation, 2012.
5. Aditya Kumar, Thorsten Staedler, and Xin Jiang, Effect of normal load and roughness on the friction coefficient in elastic and plastic contact regime, manuscript under preparation, 2012.
6. A. Kumar, N. Huang, Thorsten Staedler, C. Sun, and X. Jiang, Mechanical Characterization of Aluminum doped Zinc Oxide (Al:ZnO) Nanorods prepared by Sol-Gel Method, manuscript under preparation, 2012.
7. Aditya Kumar, Hisham Abu Samra, Thorsten Staedler, and Xin Jiang, Indentation and scratch behavior of nanocrystalline Mo_2N/BN composite coatings at the micro/nano-scale, manuscript under preparation, 2012.
8. Aditya Kumar, Thorsten Staedler, and Xin Jiang, Effect of loading rate and/or scratching speed on the tribological contact during nanoindentation, manuscript under preparation, 2012.
9. Aditya Kumar, Thorsten Staedler, and Xin Jiang, Nanotribology in the Predominantly Elastic and Plastic Contact Regime, 3rd European conference on Tribology, ECOTRIB 2011 and Viennano 2011,Vienna, Austria, June 7-9, 2011.
10. Thorsten Staedler, Aditya Kumar, and Xin Jiang, Probing the Mechanical Interaction between Particles based on Nanoindentation, 3rd European conference on Tribology, ECOTRIB 2011 and Viennano 2011, Vienna, Austria, June 7-9, 2011.
11. H. Abu Samra, A. Kumar, J. Xia, T. Staedler, X. Jiang, R. Verucchi, and I. Aronov, Development of a new generation of amorphous hard coatings based on the Si-B-C-N-O

system for applications in extreme condition at Asia-Pacific-Interfinish 2010, Singapore.

12. Aditya Kumar, Thorsten Staedler, and Xin Jiang, Effect of Roughness and/or Normal Load on the Tribological Contact during Nanoindentation, the 11th International Conference on Tribology ROTRIB'10, Nov 04-06, 2010, Romania.
13. A. Kumar, N. Huang, T. Staedler, C. Sun, and X. Jiang, Mechanical Characterization of Aluminum doped Zincoxide (ZnO:Al) Nanorods, 3rd German-Japanese Symposium on Nanostructures, 3rd International Symposium on Nanostructures, Feb 28-March 02, 2010, Wenden Olpe, Germany.

Contents

Abstract

Tribology represents a research field which has been extensively explored for a long time but a little fundamental understanding of various observations has been achieved. The main reason for this lies in the enormous complexity of the phenomena acting on the forces between two contacting bodies which are moved with respect to each other. However, the understanding of the central role of tribology in the modern society in the context of optimization of the performance as well as the lifetime of many products demands dedicated research in this interdisciplinary field. Today the technological progress in the scanning probe techniques opens up the potential to study contact phenomena on the single asperity level. In this thesis work, the influence of surface roughness, mechanical properties, adhesion force, and external parameters (applying normal load, scratching speed, and loading rate) on friction are identified.

Adhesion force between silica microspheres of different sizes and different rough surfaces (silicon and diamond-like carbon (DLC)) is measured using atomic force microscopy (AFM). The surface roughness, asperity geometry, and size of adhering particles play an important role in determining the adhesion force. Adhesion force between adhering particle and smooth surface linearly increases with size of the adhering particle. On increasing surface roughness, the adhesion force is found to show decreasing trend initially, followed by an increasing trend. The results are compared with existing as well as proposed models.

The influence of applied normal load on the tribological behavior between spherical probe and various rough surfaces such as fused silica, aluminum, DLCs, and Si-C-B-N-O coatings, is experimentally investigated using Nanoindenter and AFM. At a sufficient low level of applied normal load, wherein the contact is elastic, the friction coefficient decreases with load. At higher load, the contact involves the plastic deformation and friction coefficient will be constant. At very high load, friction coefficient increases with applied load. The surface roughness and mechanical properties (hardness and elastic modulus) have significant influence on the friction as they determine the degree of plastic deformation. An additional lateral force due to the intrinsic adhesive force is seen. After eliminating this additional adhesive force term, at a sufficient low level of applied normal load, wherein the contact is elastic, the friction coefficient is constant. By eliminating the adhesion component from friction, at increased normal loads the contact involves plastic deformation and the friction coefficient increases with increasing normal load.

The friction coefficient increases on decreasing the loading rate and increasing the scratching speed. The critical load range for a transition from either predominantly elastic to elastic-plastic contact or elastic-plastic to predominantly plastic contact between the indenter and sample increases with increasing the size of tip and the scratching speed, and it decreases with surface roughness and loading rate. The results are compared with existing models.

Symbols

%	percentage
>	greater than
<	less than
R_a	arithmetic average
rms	root-mean square
σ_s	standard deviation of the height of the surface from the mean height of asperities
z, z_i	height of the surface above the mean height (asperities)
L	sampling length
rms_m	rms-slope
m_s	asperities slope
rms_κ	rms-curvature
κ	asperity curvature
h	fix interval length of two consecutive asperities
n	total number of asperities sampled
$\Phi(z)$	cumulative probability function
$\phi(z)$, $\phi(z')$	Gaussian probability function
sk	skewness
ku	kurtosis
σ	tensile stress
σ_{ij}	stress tensor
ε	strain
ε_{ij}	strain tensor
E	elastic modulus or Young's modulus
c_{ijkl}	stiffness tensor or the elasticity tensor
G	shear modulus
P	applied normal load
R	radius of loading sphere, indenter, tip, adhering particles, colloidal probes
ξ	total displacement ($\delta_e + \delta_0$)
ν	Poisson's ratio
δ_e	elastic displacement of indenter into sample
E^*	reduce elastic modulus
δ_0	initial penetration depth (indenter)
E_1	Young's modulus of sphere (indenter)
E_2	Young's modulus of flat plane
ν_1, ν_i	Poisson ratio of sphere (indenter)
ν_2, ν_f	Poisson ratio of flat-plane
ν_s	Poisson ratio of substrate
A	real or true contact area
C_e	constant
Ω	constant
C_p	constant
δ_p	plastic displacement of indenter into sample
$A(\delta_c)$	projected area of indenter
δ_c	contact depth of indenter
δ	displacement of indenter
S	contact stiffness

B_1	constant
Λ	constant
δ_f	final displacement of indenter
δ_{Pmax}	maximum displacement of indenter
P_{max}	maximum applied load
Θ_g	geometric factor
H	hardness
δ_{eff}	effective indentation depth
E_{eff}	combined modulus of the film, substrate and indenter
t_f	film thickness
α_m	constant
I_0	function of t_f/a
A	contact radius
E_f	elastic modulus of film
E_s	elastic modulus of substrate
E_i	elastic modulus of indenter
H_s	hardness of the substrate
H_f	hardness of the thin film
H_{eff}	effective hardness of the thin film/substrate
α_k	empirically derived parameter
A_f	contact area carried by the film
A_s	contact area carried by the substrate
A_T	total contact area
σ_f	material yield stress for film
σ_{sb}	material yield stress for substrate
η	primary roughness parameter
a_0	Hertzian contact radius
χ	secondary roughness parameter
n_s	asperities density
κ_s	curvature constant
γ	Dupré energy of adhesion or work of adhesion
F_{ad}	pull-off force or adhesion force
A_H	Hamaker constant
R	radii of asperity of the plane surface
H_0	distance of the closest approach between surfaces
k_1	coefficient related to y_{max} and rms
y_{max}	height of asperities
y_{1max}	height of primary asperities
y_{2max}	height of secondary asperities
λ	peak-to-peak distance (asperities)
λ_1	peak-to-peak distance (primary asperities)
λ_2	peak-to-peak distance (secondary asperities)
ρ	number density of the asperities
Q^*_{max}	nondimensional tangential force
μ	friction coefficient
τ	shear per unit area
u	indentation depth
F_{fr}	lateral or friction force
N	number of summits in nominal surface area
A_0	nominal surface area

d_s	separation distance of two bodies
n_a	number of summits in contact
z_s	asperities height exceeds the d_s
$\bar{p}$	total nominal pressure
$f(z_s - d_s)$	asperities height distribution function
$g(z_s - d_s)$	asperities height distribution function
ψ	plasticity index
ω	interface
ω_c	critical interface
K	hardness coefficient
ω_c^*	dimensional less critical interfacial
Q_{max}	static friction or tangential force
F_{ext}	external normal force
F_s	intermolecular adhesion force
P_c	critical load (KE model)
P^*	nondimensional load
L_c	critical load (BKE model)
C_v	hardness coefficient
Y_0	yield strength
σ_y	material yield strength
ε_y	material yield strain
C_1	constant
C_2	constant
C_3	constant
u_s	scratch depth
u_0	initial indentation depth of indenter
dW/dx	rate of work done by scratching
dW_p/dx	rate of work done by scratching (plastic deformation)
dW_f/dx	rate of work done by scratching (frictional sliding)
$p(u)$	force per unit length of cylinder
k_0	constant
$\dot{\varepsilon}_s$	deformation velocity in the scratching
v	scratching velocity
b	scratching width
$\dot{\sigma}_s$	decompression rate
P_m	mean contact pressure
q	constant
d	displacement of indenter
d_0	initial penetration depth of indenter
k	spring constant
k_B	Boltzmann's constant
T	temperature
f	resonant frequency
Q	quality factor of the resonant frequency peak of the cantilever
A_m	amplitude
L_a	length of the moment arm
t_c	thickness of cantilever
h_c	height of tip
w	width of cantilever
N_c	the contact load

T	horizontal component of applied load
M	torsion moment
M_u	torsion moment when cantilever tip is scanning upward direction of a sloped surface
M_d	torsion moment when cantilever tip is scanning downward direction of a sloped surface
T_u	horizontal component of applied load when cantilever tip is scanning upward direction of a sloped surface
T_d	horizontal component of applied load when cantilever tip is scanning downward direction of a sloped surface
f_u	friction force when cantilever tip is scanning upward direction of a sloped surface
f_d	friction force when cantilever tip is scanning downward direction of a sloped surface
F_u	adhesion force when cantilever tip is scanning upward direction of a sloped surface
F_d	adhesion force when cantilever tip is scanning downward direction of a sloped surface
Θ	angle of slope surface
φ	torsion angle
l	cantilever length
J	torsion constant of the cross section
C	constant
f^{flat}	friction force when cantilever tip is scanning flat surface
M_o	measured voltage output
β	calibration constant (in newton-meters per volt)
M^{flat}	torsion moment when cantilever tip is scanning flat surface
T^{flat}	horizontal component of applied load when cantilever tip is scanning flat surface
α	calibration constant (in newtons per volt)
W	torsion loop
Δ	half-width of the loop
Δ_o	measured half-width of the loop
W_o	measured torsion loop
Δ_o^*	measured half-width of the loop for slope surface
Δ_o^{flat}	measured half-width of the loop for flat surface
W_o^{flat}	measured torsion loop for flat surface
ΔP_{err}	deviation between set applied load and actual load
ΔF_{fr}	deviation in lateral force
C_m	machine compliance
C_c	contact compliance
C_{total}	total compliance
C_0, C_1, C_2, C_3, C_4, C_5	constant
ΔP	size of ramping load scratch segment
Δt	scratching time
Δx	lateral displacement of tip
dP/dt, $\Delta P/\Delta t$	loading rate
dx/dt, $\Delta x/\Delta t$	scratching speed or lateral displacement rate of tip
R_c	radius of adhering particle (colloidal probe)
R_s	interacting particles (particles on surface)

R_{eq}	equivalent radius
W_{12}	work of adhesion per unit area
γ^{LW}	apolar (Lifshitz-Van der Waals) surface energy component
γ^{+}	electron-acceptor surface energy parameter
γ^{-}	electron-donor surface energy parameter
k_1	constant
n_{sa}	number of secondary asperities in contact
μ_T	frictional properties of the materials
k_0	constant
m	constant
P_0	constant internal load
F_0	finite friction force at zero load
μ_0	constant
k_2	constant
w_t	scratch track width
nN	nanometer
mN	millinewton
μN	micronewton
Si	silicon
C	carbon
B	boron
N	nitrogen
Co	cobalt
Fe	iron
O	oxygen
˚C	degree centigrade
mm	millimeter
Nm	nanometer
μm	micrometer
Ar+	argon ion
V	voltage
kW	kilowatt
Pa	pascal
GHz	gigahertz
mT	millitesla
WC	tungsten carbide
Ni	nickel
Ti	titanium
BF_3	boron fluoride
N_2	nitrogen
Ar	argon
He	helium
H_2	hydrogen
$Si(CH_3)_4$	tetramethylsilicate
W	watt
N/m	newton per meter
nN/V	nanonewton per voltage
Hz	hertz (per second)
μm/sec	micrometer per second
GPa	gigapascal
μN/s	micronewton per second

Abbreviations

AFM	atomic force microscopy
CVD	chemical vapor deposition
DLC	diamond like carbon
ECR	electron cyclotron resonance
FEM	finite element modeling
MWCVD	microwave plasma assisted chemical vapor deposition
XRD	X-ray diffraction
SEM	scanning electron microscopy
SAM	self assembled monolayer
PSPD	Position Sensitive Photo Detector
FIB	focus ion beam
LFM	lateral force microscopy

Chapter 1 Introduction

The tribological mechanisms and dynamics of the interactions of two contacting solids during relative motion, ranging from atomic- to micro scale, need to develop fundamental understanding of adhesion, friction, wear, indentation, and lubrication processes. The understanding of tribology is crucial for modern applications such as machining, polishing, brakes, clutches, automobiles, aircrafts engines, gears, bearing, seals, etc. The purpose of research in tribology is to minimize and eliminate the losses resulting from friction and wear at all levels of technology. Research in tribology is necessary for achieving a greater plant efficiency, better performance, fewer breakdown, and significant savings. Tribology has been actively explored for a long time; however, a little fundamental understanding of various processes has been achieved. The main reason lies in the enormous complexity of the phenomena acting on the forces between two contacting bodies which are moved with respect to each other.

Today the technological progress in scanning probe techniques to measure surface topography, adhesion, friction, wear, and mechanical properties on a nanometer scale leads to development of a new field as nanotribology. Nanotribological studies are needed to develop fundamental understanding of interfacial phenomena on an atomic or nano scale and to understand the interfacial phenomena lies in micro/nanostructures used in magnetic storage systems, micro/nanoelectromechanical systems (MEMS/NEMS), and other applications. These studies are also valuable to understand the interfacial phenomena in macrostructures and provide a bridge between science and engineering.

The tribological contact of two bodies may be defined with influencing parameters such as applied normal load, adhesion characteristics, mechanical properties, surface roughness, and external parameters (loading rate, scratching speed). Although there are many developed models for rough surface topography and they also exhibit a fundamental understanding of contact deformation regime between contacting bodies, but the behaviour of friction with respect to contact regime is still not fully understandable i.e. effect of applied normal load, surface roughness, adhesion force, and mechanical properties on friction has not been fully understood for different contact modes both at nano and/or micro scale. The loading rate and scratching speed are found to be a very important parameters and it is needed to thoroughly study the friction behavior with respect to the loading rate and scratching speed.

The approach in this thesis work is to establish a relationship between surface roughness, mechanical properties, and external parameters (normal load, loading rate, and scratching speed) on adhesion force and friction, followed by development of a relationship between adhesion force and friction using atomic force microscopy (AFM) and Nanoindenter. The tribological tests are carried out in predominantly elastic, elastic-plastic, and fully plastic contact regime. Goal here is to identify whether a distinction between materials and topographical contribution to the frictional response of the system is possible. The challenge here is to derive an understanding for the analytical description of surface asperities in the contact zone that already show yielding and those that are still in an elastic loading condition.

1.1 Overview of the thesis

Chapter 2 presents a general background about tribological phenomena. In Chapter 2, influencing parameters on tribology such as surface roughness, mechanical properties, and surface forces or adhesion forces are discussed in detail. The tribological phenomenon is then discussed in detail and how these parameters as well as external parameters influence the tribology. Chapter 3 describes the main experimental details of the work. In this chapter, initially the preparation techniques of analyzed samples and probes along with the radius calibration of probes are discussed. The instruments, those are mainly used in this thesis work, are described in detail. The basic aspects involved in AFM and Nanoindentation technique are presented. A description of normal load as well as lateral force calibration for AFM and Nanoindenter has been presented. Further in this chapter, data analysis for surface roughness, mechanical properties, adhesion force, and tribological test are presented. Chapter 4 presents the results and discussion. The chapter 4 begins with surface roughness of analyzed samples and probes, which followed by the mechanical properties of analyzed samples. Subsequent part is the discussion about the adhesion force results. In this part of chapter, the experimental results correlating particle radius, surface roughness, and adhesion forces and comparative studies with exiting models are presented. The chapter 4 ends with the discussion about tribological results. In this part of chapter 4, the effect of surface roughness, mechanical characterization, adhesion force, and external parameters (loading rate, and scratching speed) on friction in predominantly elastic, elastic-plastic, and purely plastic contact deformation regime are presented. Besides from tribological results, their interpretation and comparative studies with exiting models are also presented. Chapter 5 presents the conclusion of this thesis work. This chapter also provides suggestions for future research concerning the adhesion force, tribological phenomena, and related topics. All cited references are numbered in the

order they appear in the main text under the separate heading References. Tables and figures are numbered according to the order they appear in a particular chapter.

Chapter 2 Theoretical Background

When two bodies are in contact each other at a point or in a line, the compressive forces deform the contact surface and resulting in a change of real contact area between the bodies. The real contact area between two bodies depends on their surface roughness, mechanical properties, adhesion force, and external parameters (applying normal load, loading rate, elevated temperature, relative humidity, etc). In relative motion of two contacting bodies, real contact area governs the stress field between two bodies and that results into the modification of tribological properties. By that tribological properties depend on the surface roughness, mechanical properties, adhesion force, and external parameters (applying normal load, scratching speed, loading rate, elevated temperature, relative humidity, etc). Among these external parameters, the relative humidity and elevated temperature also influence on other parameters, as relative humidity alters the adhesion force and elevated temperature affects the surface roughness, mechanical properties, and adhesion forces. The relative humidity and elevated temperature will not consider in this thesis because they affect not only on friction, they influence other parameters and make the present problem more complicated. Surface roughness, mechanical properties, and adhesion forces are important to discuss and how they individually impact on tribology. Goal of this thesis is to identify whether or not a distinction between materials, surface forces, and topographical contribution to the frictional response of the system is possible.

In this chapter, first the surface geometric structure or surface roughness, mechanical properties, and surface forces or adhesion forces are individually defined. Next, the tribological phenomenon is discussed in detailed and how these parameters as well as external parameters influence the tribology.

2.1 Roughness

A surface is usually made up of hills and valley often called surface asperities of different lateral and vertical sized, and are distributed on the surface. A typical surface texture is shown in figure 2.1. The topographical characteristics of random rough surfaces, which are relevant to their behavior when they are into contact, are needed to briefly discuss here.

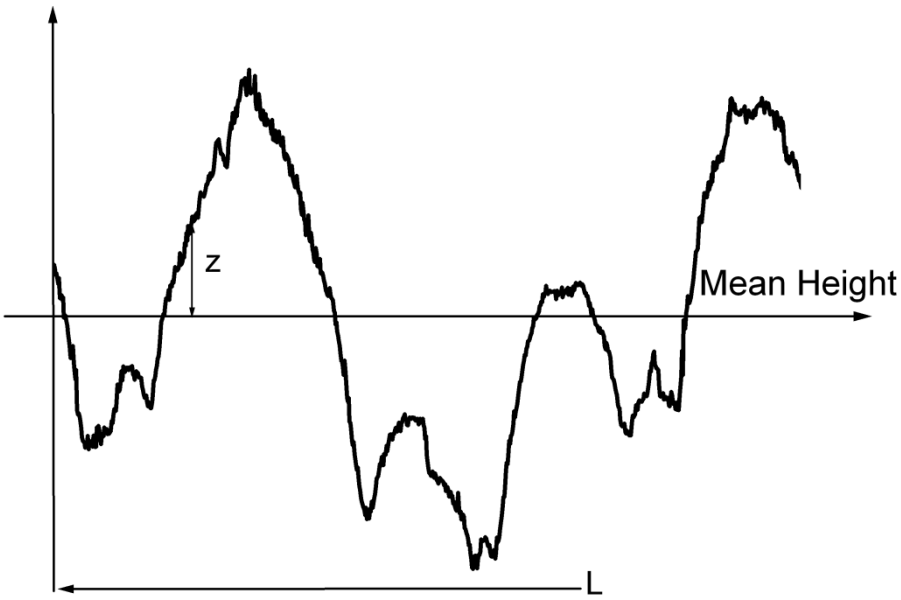

Figure 2.1: Surface profile of nanoscale rough surface, which produces a magnified trace of the surface profile by AFM.

Surface roughness is mainly defined as arithmetic average (R_a) and root-mean-square (rms) or standard deviation of the height (σ_s) of the surface from the mean height of asperities. They are defined by

$$R_a = \frac{1}{L}\int_0^L |z| dx \tag{2.1}$$

$$rms = \sqrt{\frac{1}{L}\int_0^L z^2\, dx}. \tag{2.2}$$

where z is a height of the surface above the mean height and L is a sampling length. In general the surface roughness is defined by R_a, but the surface roughness defined by rms is statistically more meaningful. The R_a value by itself gives no information about the shape of the surface profile, i.e. distribution of the derivations from the mean. It is also easy to define the asperity geometry in terms of rms. Apart the variation in height of asperities, spatial variation must also be considered. These are mainly rms-slope (rms_m) and rms-curvature (rms_κ) and they are defined as follows. If z_{i-1}, z_i, and z_{i+1} are three consecutive heights, the slope is defined by

$$m_s = (z_{i+1} - z_i)/h \tag{2.3}$$

and the curvature by

$$\kappa = (z_{i+1} - 2z_i + z_{i-1})/h^2 \tag{2.4}$$

where h is fix interval length of two consecutive heights. The rms-slope and rms-curvature are calculated as

$$rms_m = \sqrt{(\frac{1}{n}) \sum_{i=1}^{i=n} m_s^2} \tag{2.5}$$

$$rms_\kappa = \sqrt{(\frac{1}{n}) \sum_{i=1}^{i=n} \kappa^2} \tag{2.6}$$

where n = L/h is total number of asperities. Alternative approach for defining the characteristic is elementary statistics, and this approach is more meaningful and understandable. If the probability height of a particular point in the surface, which lies between z and z + dz, is denoted by $\phi(z)$, then the probability that the height of a point on the surface is greater than z is given by the cumulative probability function:

$$\Phi(z) = \int_z^\infty \phi(z')dz'. \tag{2.7}$$

It has been found that many real surfaces exhibit a height distribution which is close to the normal or Gaussian probability function:

$$\phi(z) = \frac{1}{rms\sqrt{2\pi}} \exp\left(-\frac{z^2}{2rms^2}\right)$$

The cumulative probability will be

$$\Phi(z) = \frac{1}{2} - \frac{1}{(2\pi)^{\frac{1}{2}}} \int_0^{z/\sigma} \exp\left(-z'^2/2rms^2\right) d(z'/rms). \tag{2.8}$$

When the surface profile deviates from normal or Gaussian distribution, two additional parameters (skewness and kurtosis) are introduced. The skewness (sk) refers to whether the distribution is symmetrical with respect to its dispersion from mean or not. The kurtosis (ku) refers to the weight of the tails of a distribution.

$$sk = \frac{1}{rms^3} \int_{-\infty}^{\infty} z^3 \ \phi(z)dz \tag{2.9}$$

$$ku = \frac{1}{rms^4} \int_{-\infty}^{\infty} z^4 \ \phi(z)dz \tag{2.10}$$

For the Gaussian distribution, sk = 0 and ku = 3. As mentioned above, the quantities rms, rms_m, and rms_k are mostly dependent on the sample size as well as the instrument resolution. These parameters cannot be used to characterize a rough surface since they are scale dependent and use of these parameters in any statistical theory of tribology can lead to error in the results. Roughness measurements show that the most surfaces are composed of small asperities that sit on large asperities, which sit on even larger asperities in a hierarchical manner. To characterize this intrinsic multiscale structure of surface roughness, one must develop techniques that are independent of any length scale. The hierarchical structure allows fracture geometry to be used to characterize a surface by scale-independent parameters [1]. Fractural technique shows up a number of difficulties. Many surfaces don't show the scaling hierarchical behavior that fractal characterization demands. Another problem is that a fractal characterization is meaningful only when extending dimension of the surface is several orders of magnitude of fractal dimension. The roughness in term of rms is more appropriate and suitable in tribological characterization, if rms of analyzed samples is done at similar length scale and with similar instrumental resolution. In this thesis, the surface roughness in term of rms has been used.

2.2 Mechanical properties of samples

Knowledge of the mechanical properties of materials is crucial for an understanding of tribological behavior at nano-scale. The mechanical properties influence the behavior of two contacting bodies such as the real contact area, the onset plastic deformation, and shearing forces. Prior to detailed study of tribological behavior, it is needed to understand the mechanical properties such as hardness and elastic modulus. The hardness here is no direct physical material property; however, it is defined as the maximum applied load divided by the residual indentation area. An elastic modulus is the mathematical description of a material's tendency to be deformed elastically (non-permanently) when a force or load is applied to it. It is defined as the slope of its stress-strain curve in the elastic deformation region. These quantities are determined using the Nanoindentation, a local load on a surface using a diamond indenter with a defined geometry. In this sub-chapter, the theoretical bases, which permit a determination of the hardness and the elastic modulus, are presented.

2.2.1 Mechanical characterization of isotropic half-space

In this section, the basics of the characterization of mechanical properties of an uncoated isotropic half-space are discussed. Mechanical properties such as elasticity, plasticity, breaking strength, and internal tensions, etc. are based on the interaction of individual atoms of the materials. Isotropic materials are characterized by properties which are independent of direction in space. Isotropic solid material follows the Hooke's law of elasticity (equation 2.11).

$$\sigma = E\epsilon \tag{2.11}$$

where σ is tensile stress, ε is strain, and E is the elastic modulus of the material. When working with a three-dimensional stress state, a 4^{th} order tensor containing 81 elastic coefficients must be defined to link between the stress tensor σ_{ij} (i, j = 1, 2, 3) and the strain tensor ε_{kl}.

$$\sigma_{ij} = \sum_{k,l} c_{ijkl}\epsilon_{kl} \tag{2.12}$$

where c_{ijkl} is the stiffness tensor or the elasticity tensor. Due to the symmetry of the stress tensor, strain tensor, and stiffness tensor, only 21 elastic coefficients are independent. As stress is measured in units of pressure and strain is dimensionless, c_{ijkl} is also measured in units of pressure. Physical equations involving isotropic materials must, therefore, be independent of the coordinate system. The strain tensor is a symmetric tensor. Since the trace of any tensor is independent of any coordinate system, the most complete coordinate-free decomposition of a symmetric tensor is to represent it as the sum of a constant tensor and a traceless symmetric tensor. For isotropic materials, only two independent components are remained (c_{11} and c_{12}). The elastic properties of isotropic materials are usually described by the elastic modulus or Young's modulus ($E = c_{11}$), the shear modulus ($G = (c_{11} - c_{12})/2$), and Poisson's ratio $\nu = - c_{11}/c_{12}$. These elastic properties are interrelated in following relation

$$E = 2G(1 + \nu). \tag{2.13}$$

Hertz's analysis for a sphere loading on a semi-infinite half-space is considered the first solution of contact of two elastic bodies [2]. The approach of two remote points in the sphere and half-space is given by

$$P = \sqrt{\frac{16RE^{*2}}{9}}\xi^{3/2} \tag{2.14}$$

where $\xi = \delta_e + \delta_0$, δ_e is elastic displacement, P is applied load, and R is radius of loading sphere, and δ_0 is initial penetration depth. E^* is the reduce elastic modulus which is given by

$$\frac{1}{E^*} = \frac{1-\nu_1^2}{E_1} + \frac{1-\nu_1^2}{E_2}, \tag{2.15}$$

E_1 and E_2 are Young's modulus of sphere and flat plane and ν_1 and ν_2 are Poisson ratio of sphere and flat-plane, respectively. Hertz determines a relation area of contact (A) by

$$A = \pi\left(\frac{3PR}{4E^*}\right)^{2/3}. \tag{2.16}$$

Hertz theory describes the contact area for smooth macroscopic contacts. It is applicable only to homogeneous, isotopic, linear elastic materials that exhibit no attractive surface forces (adhesion) and assumes that the contact radius is much smaller than the sphere radius, so that the sphere can be approximated as a parabolic. In several cases, ξ is considered as δ_e which leads to wrong results. Hertz is valid only for the case of an infinite rigid sphere. Hertz theory is not suitable at small deformation scales because the adhesion force between the loading probe and the surface of testing material is comparable, and cannot be neglected [3]. In general, the elastic contact can always describe in following form [4]

$$P = C_e\delta_e^{\Omega} \tag{2.17}$$

where constant C_e and Ω are dependent on geometry of indenter, Poisson's ratio and mechanical properties of indenter and flat surface. Ω value will be 1 and 1.5 for flat punch indenter and parabolic indenter, respectively. In case of geometrically similar indenters such a pyramidal, conical, Vickers, Berkovich, the elastic contact equation (2.17) can be written as

$$P = C_e\delta_e^2. \tag{2.18}$$

Indentation tests on many materials results in both elastic and plastic deformation of the material. Plastic deformation is irreversible deformation. The mechanical property of material in the plastic deformation is measured in term of hardness. During plastic deformation the original position of atoms of material changes. A solid body begins to deform plastically when the stress satisfies a yield condition. For a local load, plastic deformation is expressed by a final impression on indenter on the surface. The ideal plastic behavior in case of conical indenter can be described by following equation [5].

$$P = C_p \delta_p^2 \tag{2.19}$$

where, C_p is contact and δ_p is plastic displacement of indenter. C_p is dependent on geometry of indenter, Poisson's ratio and mechanical properties of indenter and flat surface. In case of elasto-plastic behavior, the indenter displacement (δ) will be

$$\delta = \delta_e + \delta_p. \tag{2.20}$$

For a conical indenter, elasto-plastic contact can have following relation

$$P = \left(\frac{1}{\sqrt{C_e}} + \frac{1}{\sqrt{C_p}}\right)^{-2} \delta^2 \tag{2.21}$$

The projected area ($A(\delta_c)$) of indenter is function of penetration depth (δ_c) and it depends on materials parameters of half-space and geometry of the indenter. For conical indenter the initial unloading contact stiffness (S) is calculated as slope of initial portion of unloading curve (figure 2.2).

$$S = \frac{dP}{d\delta} = \frac{2\sqrt{A(\delta_c)}}{\sqrt{\pi}} \frac{E^*}{(1-\nu^2)} \tag{2.22}$$

Above relationship (equation 2.22) is valid when the discharge in unloading of indenter is purely elastic and contact area ($A(\delta_c)$) is equal to the optically measured area of the hardness impression. Doerner et al. [6] measured S by fitting a straight line about one third upper portion of unloading curve. The problem with this is that for nonlinear loading data, the measured stiffness depends on how much of the data is used in the fit. Oliver and Pharr method [7] proposed that the entire unloading data are well described by a simple power law relation

$$P = B_1(\delta - \delta_f)^{\Lambda} \tag{2.23}$$

where constant B_1 and Λ are determined by a least square fit. Pharr et al. [8] showed that the above equation (2.22) is valid for any rigid indenter that can be described as a body of revolution of a smooth function. The above equation (2.22) is valid for at least some indenters, those cannot be described as bodies of revolution, has been confirmed by the finite element calculation of King [9]. According to Oliver and Pharr method [7], the overall penetration depth (δ) is sum of elastic component (δ_e) and portion which the indenter

penetration into the material under load (δ_c), also refer as contact depth. The schematic diagram of load vs. displacement is shown in figure 2.2.

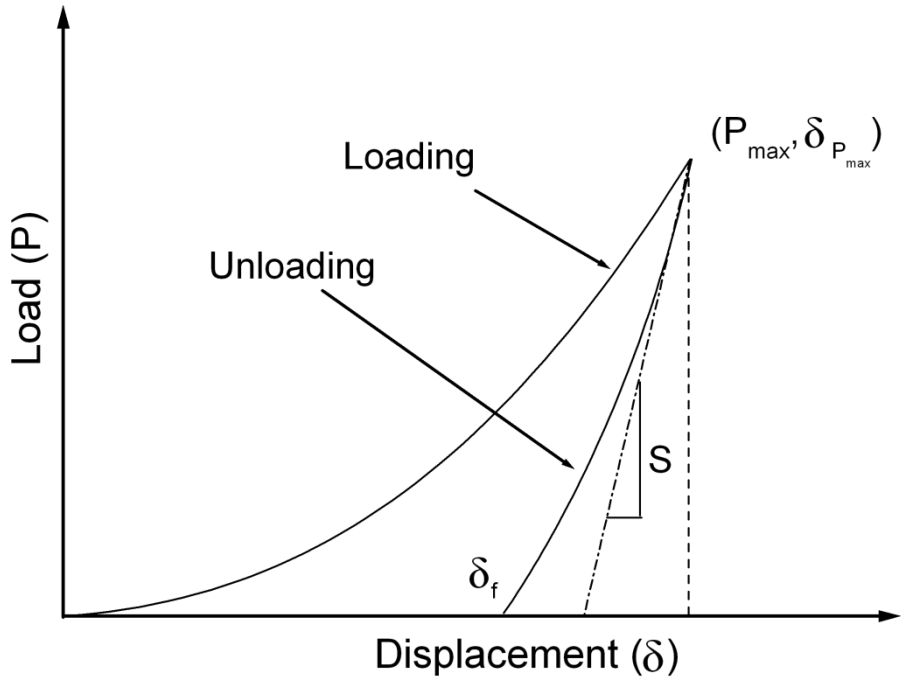

Figure 2.2: Load vs. displacement curve.

Using equation (2.17) and (2.18) and a geometric factor (θ), the contact depth will result into

$$\delta_c = \delta_{P_{max}} - \delta_e = \delta_{P_{max}} - \theta_g \frac{P_{max}}{S}. \quad (2.24)$$

θ_g is 0.72 for conical, 0.75 for paraboloid, and 1 for a flat punch. Oliver and Pharr model defined the hardness (H) of a material as

$$H = \frac{P_{max}}{A(\delta_c)} \quad (2.25)$$

The elastic modulus and hardness values can only determined if the area function of indenter ($A(\delta_c)$) is known. For a Vicker or Berkovich indenter with ideal pyramidal geometry, the projected contact-area-to-depth relationship is given as [6, 10]

$$A(\delta_c) = 24.5\delta_c^2 \quad (2.26)$$

and effective indentation depth (δ_{eff}) can be obtained from the following equation

$$\delta_{eff} = \left(\frac{A}{24.5}\right)^{1/2} \tag{2.27}$$

A is obtained from the shape calibration and true contact depth [6]. It is observed that ideal geometry underestimates the contact area which leads to overestimation of hardness and elastic modulus. Oliver and Pharr method [7] proposed a method for determining the area function that requires no imaging. This method is based on one assumption that the Young's modulus is independent of the indentation depth. They proposed a method of determine load frame compliance. The method for determining of load frame compliance and method for area function will discuss in Instrumental sub-chapter of chapter 3. The Oliver and Pharr method is well suitable for rigid indenter and isotropic half-space system. The standard commercially available diamond Berkovich indenter is usually used. In an indentation into an elastic material, the surface of the material is typically drawn inwards and downwards underneath the indenter and sinking-in occurs. When the contact involves plastic deformation, the material may either sink-in or pile-up around the indenter. In those cases, the projected contact area will be underestimated or overestimated. McElhaney et al. [11] determined the correct contact area using the contact stiffness and SEM image of residual impression from large indentations. The FEM based work showed that the ratio of the residual depth and the total depth is a useful parameter for determining the extent of piling-up during indentation. This work assumed that the mechanical properties are independent of indentation depth.

2.2.2 Mechanical characterization of coated (film/substrate system) isotropic half-space

In this section, the mechanical characterization of thin film is discussed. The main difficulty in measuring mechanical properties of thin films is substrate effect on mechanical properties. This problem is usually solved by indenting only up to 10 % of thickness of thin film and this is, however, not a strict rule. Several studies have done in this aspect. King et al. [12] proposed an expression for combined modulus (E_{eff}) of the film, substrate, and indenter

$$\frac{1}{E_{eff}} = \frac{(1-\nu_f^2)}{E_f}\left(1 - e^{-\alpha_m t_f/\sqrt{A(\delta_c)}}\right) + \frac{(1-\nu_s^2)}{E_s}\left(e^{-\alpha_m t_f/\sqrt{A(\delta_c)}}\right) + \frac{(1-\nu_i^2)}{E_i} \tag{2.28}$$

where f, s, and i refer to the film, substrate, and indenter, respectively. t_f is film thickness, α_m is constant and dependent on material properties. Gao et al. [13] proposed closed-form solution as

$$E_{eff} = E_s + (E_f - E_s)I_0 \tag{2.29}$$

where I_0 is a function of t_f/a and a is contact radius. I_0 is defined as

$$I_0 = \frac{2}{\pi}\tan^{-1}\frac{t_f}{a} + \left[(1-2\nu)\frac{t_f}{a}\ln\left(1+\frac{1}{(t_f/a)^2}\right) - \frac{t_f/a}{1+(\frac{t_f}{a})^2}\right]\left(\frac{1}{2\pi(1-\nu)}\right) \quad (2.30)$$

I_0 will be zero for zero thickness film and it will be unity for very thick film. Due to complex nature of the plastic zone at interface of film and substrate, the measurement of combined hardness value of a film-substrate system is difficult process. Bückle et al. [14] proposed an expression for combined hardness (H_{eff}) of the film, substrate, and indenter

$$H_{eff} = H_s + \alpha_k(H_f - H_s) \quad (2.31)$$

where H_s and H_f are hardness of the substrate and the thin film with α_k being an empirically derived parameter. Johnson et al. [15] expressed the combined hardness of the film-substrate system using law of mixtures for contact area (equation 2.32).

$$H_{eff} = H_f\frac{A_f}{A_T} + H_s\frac{A_s}{A_T} \quad (2.32)$$

where A_f and A_s are the relative parts of the contact carried by the film and the substrate, respectively, and A_T is the total contact area. In literature several studies have been done based on law of mixtures for volume of deformation [16, 17]. Bhattacharya et al. [18] developed empirical equations for film-substrate combinations for which the substrate is either harder or softer than film. For a soft film on a hard substrate H_{eff} is

$$H_{eff} = H_s + (H_f - H_s)\exp\left(-\frac{\sigma_f}{\sigma_{sb}}\frac{E_s}{E_f}\left(\frac{\delta}{t_f}\right)^2\right) \quad (2.33)$$

where σ_f and σ_{sb} are material yield stress for film and substrate, respectively. For hard films on a soft substrate, H_{eff} becomes

$$H_{eff} = H_s + (H_f - H_s)\exp\left(-\frac{\sigma_{sb}}{\sigma_f}\frac{H_f}{H_s}\sqrt{\frac{E_s}{E_f}}\frac{\delta}{t_f}\right) \quad (2.34)$$

Tsui et al. [19] proposed an empirical expression for correcting for pile-up effects for the case of soft materials on hard substrates. Stone et al. [20] observed that the hardness increases as indentation depth approaches the interface. Bull et al. [21] proposed a model based on energy deformation. Despite the huge analytical foundation and experimental work, there has no complete understanding the substrate effect on mechanical properties and there is no one

relationship as yet proposed for an entire range of materials. In the absence of any rigorous relationship, the conventional 10 % of the thickness rule appears to be that most generally used. Finite element modeling work showed that this work for about 30 % in the case of soft coatings on hard substrates.

2.2.3 Surface roughness effect

Surface roughness is a very important issue in Nanoindentation based mechanical characterization. The surface roughness causes an error in determining the projected area of the indenter and therefore an error in mechanical properties is measured. In literature several analytical models [22-32] proposed usually involve elastic or purely plastic contact in order to take surface roughness into account. This aspect will discuss in later part of this chapter in tribological phenomena. This section is concerned of the effect of surface roughness on the hardness measurements. The surface roughness can be quantified by a roughness parameter (η), which is defined as

$$\eta = \frac{\sigma_s \cdot R}{a_0^2} = \sigma_s \left(\frac{16RE^{*2}}{9P^2}\right)^{1/3} \tag{2.35}$$

where σ_s is standard deviation of the height of the surface from the mean height of asperities or root-mean square (rms) and a_0 is contact radius for smooth surface under the applied load P, i.e. given by Hertz theory. The second parameter (χ) is introduced by Greenwood et at. [24] as

$$\chi = \frac{8}{3} n_s \sigma_s \left(\frac{2R}{\kappa_s}\right)^{1/3} \tag{2.36}$$

where n_s is asperities density, κ_s is constant curvature. The parameter χ depends on surface roughness but not on the applied load. From the analysis in ref [33], it is seen that effect of surface roughness on the contact pressure and contact area is governed primarily by η. The effect of surface roughness on elastic contact behavior is neglected if η is less than 0.05. The value of η increases with increasing the radius of the indenter and increases with decreasing the load. Therefore the surface roughness has significant role at low level of applied load with spherical indenters. For sharp indenters such as Berkovich indenter, the effect of surface roughness is less severe. The mechanical properties of analyzed samples in this thesis work have been measured with a sharp diamond Berkovich indenter.

2.3 Adhesion concept

When two surfaces of the same materials come together, there is a negative potential energy associated with the contact. This energy is the work of cohesion of the interface. If two surfaces are different materials then the energy is called as work of adhesion. Adhesion is a term relating to the force required to separate two bodies in contact with each other [34]. The magnitude of different contributions to adhesion is presented in figure 2.3. Four main contributions to adhesion can be identified [35]. The weakest influence arises from molecular interaction followed by electrostatic attraction, capillarity, and the action of excess charges. Whereas the action of capillarity and excess charges is continuum quantities, molecular attraction and electrostatic forces are caused by quantum mechanical interactions (e.g. Van der Waals forces and /or interlocking forces of molecules).

The shortest range of interaction is governed by the molecular forces. To induce strong attraction, the spacing between the solids must be reduced to a distance lower than about 10 nm. Mostly, this is not the case, since natural and technical surfaces are not atomically smooth. Molecular forces between electrically neutral particles can occur in different ways [35]. For rotating symmetric non polar particles, an attractive interaction is caused by quantum fluctuations in the electronic structures of two closely neighboring particles leads to dipole moments, which attracts mutually. This type of attraction is known as the Van der Waals interaction and consists of repulsive and attractive contribution. In case of polar molecules, important reason for molecular attraction is hydrogen bonding due to dipole-dipole interaction between an electronegative atom and a hydrogen atom bonded to another electronegative atom (fluorine, oxygen or nitrogen). The dipole-dipole interaction between the polar compounds (e.g. salt) is also responsible for molecular attraction.

The electrostatic forces can be divided into two different contributions [35]. First is classical Coulomb attraction, which is induced by the bulk excess charges present on the surface. This force vanishes after proper grounding of the samples. The second contribution arises from the electrostatic contact potential resulting in the electrical double-layer force, which remains constant after grounding.

Capillarity is closely associated with adhesion, cohesion, and surface tension [35]. A wetting liquid is pulled upwards in a capillary due to surface tension. The necessary energy comes from the interaction of the liquid with the capillary wall. In sliding systems, two surfaces are

brought in close contact. The resulting slits and pores act as capillaries. The water inside these slits leads to an increase of the normal force and to resistance against shear. The resistance via shear will be due to the viscosity of the water within the bridge, and is also dependent on the shear rate and the gap width. The capillary bridge is formed only if the liquid wets both surfaces. The capillary action depends strongly on the interfacial properties of liquid and solid as well as liquid and vapor.

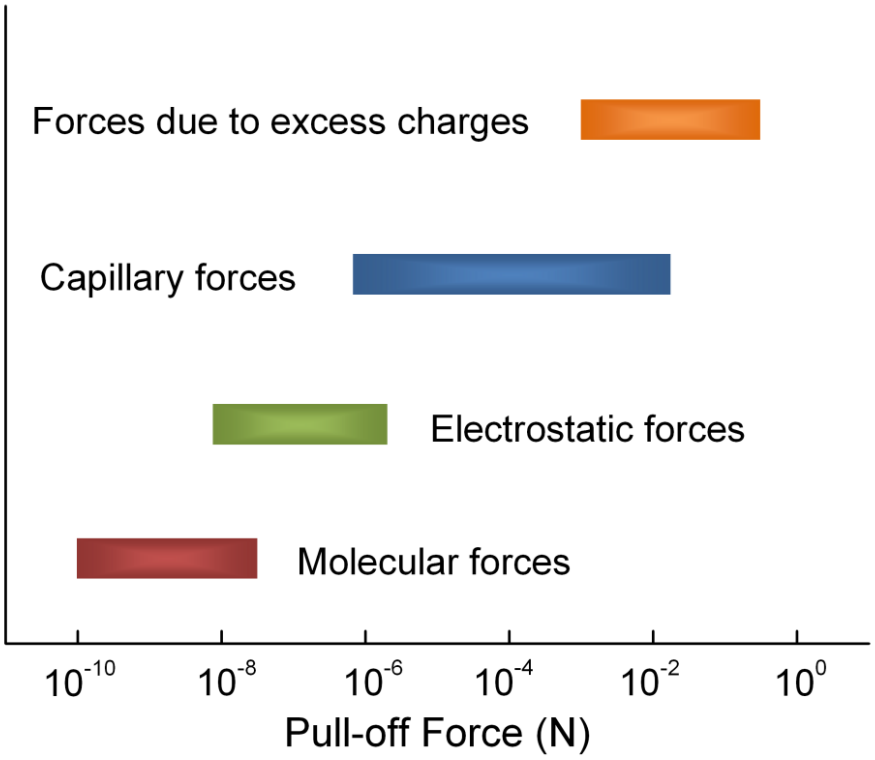

Figure 2.3: Forces contributing to adhesion.

The adhesion between surfaces is governed by the deformation of two bodies in contact and the surface forces acting between both bodies. These two phenomena are inherently coupled as the both events are dependent with each other. This interdependence makes the theory of adhesion a complex problem that is still under debate. Much of present understanding of elastic adhesion mechanics (adhesion and deformation) of spheres on planer substrates is based on the theoretical work of Johnson, Kendall, and Roberts (JKR) [36] and Derjaguin, Mullar, and Toporov (DMT) [37].

JKR model proposed a new theory that account for adhesion between two elastic bodies. According to JKR, the experimentally measured contact area is larger than the one predicted by Hertz theory at low loads, and by the observation of finite contact area at zero applied load.

The model derived the following equation to describe the contact area (A) between a sphere and a plane with adhesion acting.

$$A = \pi\left(\frac{3R}{4E^*}(P + 3\Delta\gamma\pi R + \sqrt{6\Delta\gamma\pi RP + (3\Delta\gamma\pi R)^2}\right)^{2/3}, \quad (2.37)$$

where γ is the Dupré energy of adhesion or work of adhesion. It is, in fact, energy per unit area and it represents the work done in completely separating a unit area of the interface. This theory includes infinite tensile stress at the contact area perimeter, a non-zero contact area at zero loads and a minimum stable normal load which still exhibits a non-zero contact area. According to JKR model, the adhesion force is given as

$$F_{ad(JKR)} = 3\pi\Delta\gamma R. \quad (2.38)$$

Later, DMT model derived a separate expression to include adhesion in the contact of elastic bodies. They assumed that the deformed contact profile remained the same as in the Hertz theory, however, with an overall higher load due to adhesion. This is due to all attractive interactions between the sphere and the plane, like a dead weight, and therefore contact radius is

$$A = \pi\left(\frac{3R}{4E^*}(P + 2\Delta\gamma\pi R\right)^{2/3}. \quad (2.39)$$

According to DMT model, the adhesion force is

$$F_{ad} = 4\pi\Delta\gamma R. \quad (2.40)$$

Although the apparent discrepancy between JKR and DMT models results into a heated debate, this controversy is settled when it is determined that both models are valid at opposite ends of the same spectrum of contact behavior. When surface forces are short ranged compare to the resulting elastic deformations due to compliant materials, large sphere radii, and strong and short-range adhesion forces, the JKR model works accurately. In case of stiff materials, small sphere radii and wear, long-range adhesion forces, the DMT works accurately. Here, one interesting point is that the pull-off force or adhesion force (F_{ad}) derived by both JKR and DMT models is independent of the elastic modulus and it is mainly dependent on the work of adhesion ($\Delta\gamma$) and the radius of curvature (R).

2.3.1 Dependence on applied load and contact time

No dependency of the adhesion force on the applying load or the contact time is expected by the JKR and DMT models, wherein the deformation is predominantly elastic. If one of the contacting bodies shows the visco-elastic deformation, then the contact area and adhesion force increases with contact time. When plastic deformation occurs, load depending adhesion force can be seen [38]. Schaefer et al. [39] studied adhesion force between polystyrene particles and a silicon surface and observed an increase of adhesion with increasing load. Biggs et el.[40] observed the load and contact time dependence on adhesion for polystyrene particles on mica surface in dry nitrogen atmosphere. For slower scan speeds an increasing hysteresis was observed, indicating significant deformation of the surfaces. Gady et al [41] investigated adhesion between polystyrene particles and polyurethane, permuthane, and polyurethane coated with a 5 μm layer of permuthane and observed no significant effect of load within certain limit of load. Reitsma et al. [42, 43] measured the adhesion between polystyrene particles on silica surface as a function of applied load and loading time in nitrogen atmosphere. An increase of adhesion with increasing load indicates the elasto-plastic deformation, whereas an increase of adhesion with loading time reveals visco-elastic deformation. Heim et al. [44] and Ecke et al. [45] studied the interaction of silica particle to silica particle and silica particle to silicon substrate and found that adhesion force independent of loading force within a range, surrounding air pressure, and the relative humidity within a range. This issue can be solved by keeping the applied load constant and in predominantly elastic deformation regime.

2.3.2 Influence of surface roughness

When measuring the adhesion forces between atomically smooth surfaces, a good agreement finds with traditional models. JKR and DMT both models neglect the surface roughness, which causes a non-uniform pressure distribution across the real contact area. Regardless of surface preparation method, most of the engineering surfaces show some finite roughness. Earlier several studies have showed that the existence of nanoscale roughness is known to dramatically reduce adhesion between two contacting bodies due to a decrease in the real area in contact and increase in the distance between bulk surfaces [36, 46-49].

The classical Rumpf's model [50] is most commonly used model of adhesion force in the nanoscale roughness, which is based on contact of a single hemispherical asperity whose

center lies on the surface plane and interacting with a much larger spherical particle along a line normal to the surface plane connecting their centers as shown in figure 2.4.

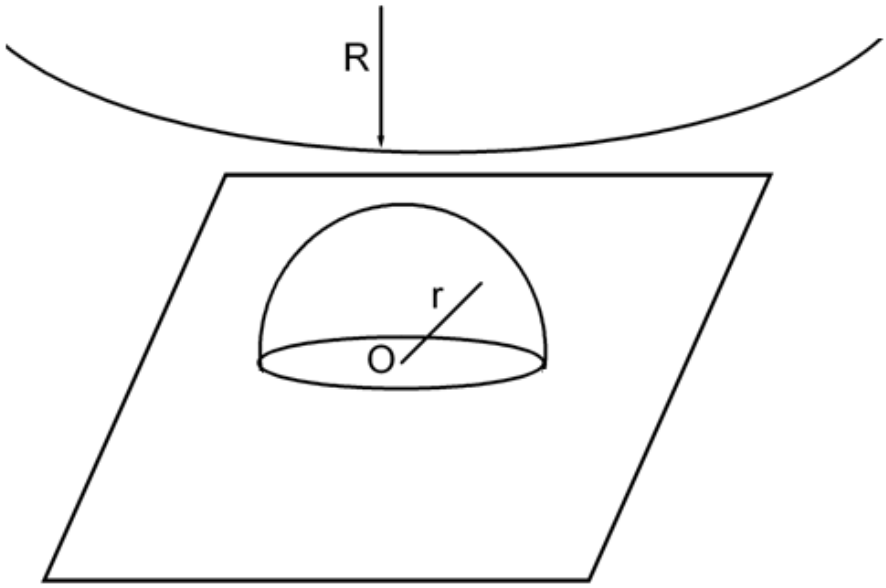

Figure 2.4: Schematic diagram of the geometry proposed by Rumpf [50] is for the interaction of an adhering particle with a rough surface. Diagram shows a hemispherical asperity of radius r and origin at the surface interacting.

Rumpf's model is consisting two terms that describing the total Van der Waals interaction: the first one represents the interaction of the adhering particle in contact with the asperity and second is for the noncontact force between the adhering particle and flat surface separated by the height of the asperity. Using the geometry and Derjaguin's approximation [51] for both contact and noncontact attractive forces, the following equation (2.41) for adhesion force is obtained.

$$F_{ad} = \frac{A_H}{6H_0^2}\left[\frac{rR}{r+R} + \frac{R}{(1+r/H_0)^2}\right] \tag{2.41}$$

where A_H is the Hamaker constant, R and r are the radii of the adhering particle and asperity of the plane surface, respectively, and H_0 is the distance of the closest approach between surfaces. The value of H_0 is usually taken to be 0.3 nm, but different values have been suggested for a group of material based on first principles [52]. Rumpf's model described the methodologies to predict the adhesion force between surfaces of known asperity geometry but unfortunately a little has been said about how well those geometries correlate with known surface roughness profiles. Later, Rabinovich et al. [53, 54] proposed to link the average radius of hemispherical asperities (r) to the measured root-mean-square roughness (rms) as

$$r = 1.485\text{rms}. \tag{2.42}$$

The limitation of Rumpf [50] and modified Rumpf model by Rabinovich et al. [53] is that the center of the hemispherical asperity is at the surface. As the surface roughness decreases, the radius of asperity must increases. For ideal perfectly flat surface, the surface roughness approaches to zero and then the radius of asperity tends to infinity. For this situation to be valid, if the asperity is still modeled as a sphere, the center of the asperity cannot be at the surface. Instead the center must be located some distance below the surface such that the observed asperity height is equivalent to the radius in the Rumpf geometric model.

Rabinovich et al. (Rabinovich model [53]) extended the modified Rumpf model by introducing a new parameter. This model considered that the center of asperities lies below the average surface plane. According to this model, the breadth of asperities is also an important parameter. Figure 2.5 depicts surface roughness as close-packed hemispherical asperity caps and troughs.

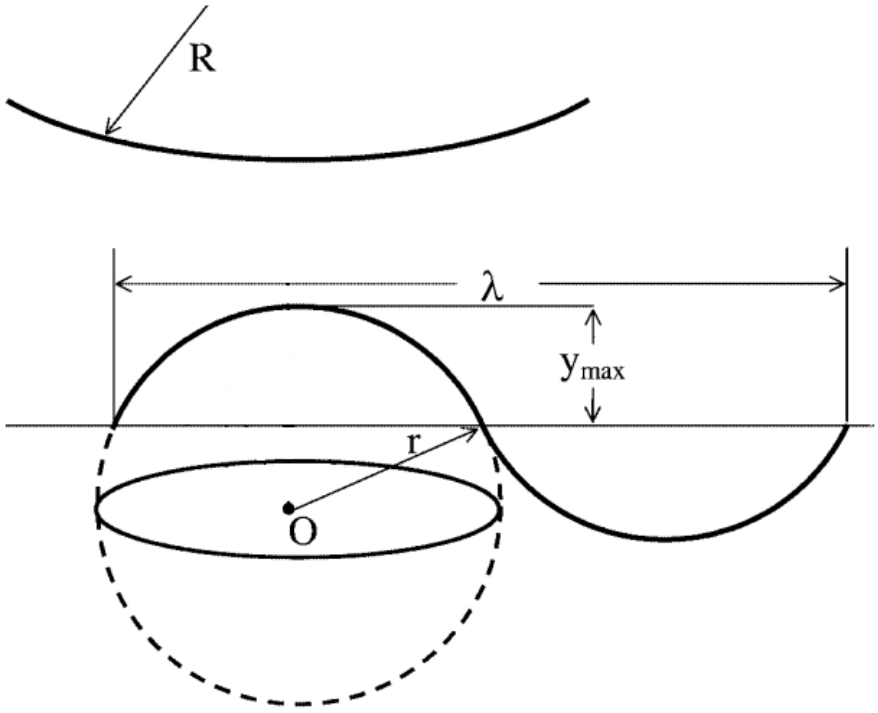

Figure 2.5: Schematic diagram of the geometric model used to calculate adhesion force between a spherical adhering particle and a surface in the Rabinovich model [53]. It shows a hemispherical asperity of radius r, peak-to-peak distance λ, and origin below the average surface.

As in the Rumpf model, a single particle interacting with a single asperity along a line connecting their centers and perpendicular to an average surface plane will be considered. However the asperity will be characterized by radius (r) and peak-to-peak distance (λ). Finally the following equation for adhesion force is obtained,

$$F_{ad} = \frac{A_H R}{6H_0^2}\left[\frac{1}{1+\left(\frac{32Rk_1 rms}{\lambda^2}\right)} + \frac{R}{\left(1+\frac{k_1 rms}{H_0}\right)^2}\right], \tag{2.43}$$

where k_1 is a coefficient related to y_{max} and rms, and λ is the peak-to-peak distance of the surface asperities.

The Rabinovich model [54] is additionally modified to account for the second order asperities on samples of very nanorough surfaces. The geometry of this model is shown schematically in figure 2.6. In this model, roughness is described by asperities with heights y_{1max} and y_{2max} as well as peak-to-peak distance λ_1 and λ_2.

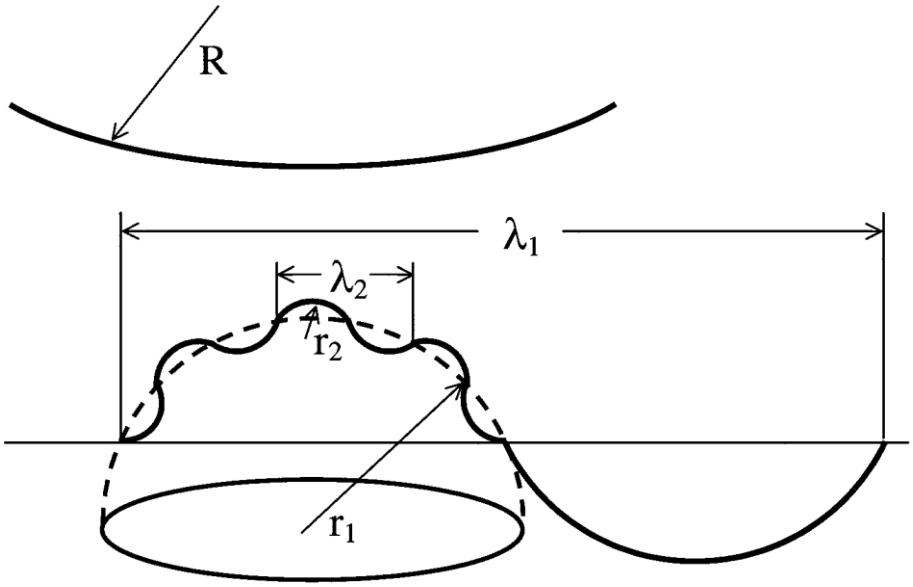

Figure 2.6: Important parameters proposed by Rabinovich model [54]. The model diagram shows small asperities superimposed on big asperities, while the origins of big asperities are positioned below the average surface. λ_2 and r_2 are roughness parameters, whereas λ_1 and r_1 refer to waviness.

To calculate the adhesion force in the framework of this model, equation is considered valid for each superimposed roughness scale. As a result, similar to derivation of equation, but also

accounting for the contact interaction of sphere with rms_2 and noncontact interaction with the rms_1 and flat substrate, the following formulas are obtained:

$$F_{ad} = \frac{A_H R}{6H_0^2}\left[\frac{1}{1+\left(\frac{58R(rms_2)}{\lambda_2^2}\right)} + \frac{1}{\left(1+\frac{58Rrms_1}{\lambda_1^2}\right)\left(1+\frac{1.82rms_2}{H_0}\right)^2} + \frac{H_0^2}{\left(H_0+1.82(rms_1+rms_2)\right)^2}\right]. \quad (2.44)$$

As λ_l becomes comparable to R, there is less and less material in average surface plane that is not already contained in the asperity. Hence for such a situation, the third term in equation is largely redundant and must be dropped, yielding

$$F_{ad} = \frac{A_H R}{6H_0^2}\left[\frac{1}{1+\left(\frac{58R(rms_2)}{\lambda_2^2}\right)} + \frac{1}{\left(1+\frac{58Rrms_1}{\lambda_1^2}\right)\left(1+\frac{1.82rms_2}{H_0}\right)^2}\right]. \quad (2.45)$$

Basically above equation is applicable at any value of rms_1. In the limit of small values of rms_1, when $rms_1 << \lambda_l^2/58R$, equation reduces to equation (2.43). According to Rabinovich model, the adhesion force or normalized adhesion force (F_{ad}/R) decreases sharply with increasing surface roughness in the nanometer scale (< 2 nm); followed by a gradual and slow decrease with further increase in roughness. Rabinovich et al. gives reasonable estimates for pull-off forces with particles comparable in size with the asperities on the surface. It underestimates the adhesion if the particles are much larger than the asperities.

Further, Katainen et al. [55] (Katainen model) is extended the Rumpf model in which the interaction is considered between a large, blunt sphere and hemispherical asperities on the surface. This model assumed multiple contacts underneath the sphere and the average number of asperities that come into contact is the product of the contact area with the number density of the asperities.

$$F_{ad} = \frac{A_H A}{6H_0^2}\left[\rho r + \frac{1}{\pi H_0\left(1+\frac{y_{max}}{H_0}\right)^3}\right]. \quad (2.46)$$

where A is contact area and ρ is the number density of the asperities. They studied adhesion forces for blunt particles on surfaces up to 10 nm rms roughness. Measurements with particles both smaller and larger than surface features are presented. According to this finding, the adhesion of particles smaller than or similar in size to the asperities depends mainly on the

size and shape of the asperities and only weakly on the size of the particle. For large particles the particle size also has a significant effect on the adhesion. Several other studies have dealt with the effect of roughness on adhesion force [56-65], particularly after the colloidal-probe technique was introduced by Ducker et al. [66]. Most of these studies reveal that the adhesion force decreases with increasing roughness due to the decreasing the contact area.

2.4 Tribological Phenomena

Friction is usually defined by a friction coefficient (μ). Amontons 1st law enables to define a coefficient of friction (μ) as the ratio of the friction force or lateral force (F_{fr}), the resistance which opposed the motion, to the applied normal load (P) (equation (2.47)).

$$\mu = \frac{F_{fr}}{P} \tag{2.47}$$

Several studies have shown that the friction force for a single asperity contact is proportional to true contact area [67] (equation (2.48)).

$$F_{fr} = \tau \cdot A \tag{2.48}$$

where τ is shear per unit area and A is true contact area. Friction influences by the contact geometry and elasto-plastic properties, according to Hertz theory for a nonadhering rigid perfectly spherically body (R) in contact with a perfectly smooth half-space or flat surface, the friction coefficient will be

$$\mu = \pi\tau \left(\frac{3R}{4E^*}\right)^{2/3} P^{-1/3}, \tag{2.49}$$

where P is applied load. This relation is referring as Hertz's 1/3th rule. For a given load and radius of sphere, the friction value is mainly dependent on the mechanical properties of contact partners. Hertz theory describes the contact area for smooth macroscopic contacts and it is still used now-a-days in many applications. Hertz model is applicable only to homogeneous, isotopic, linear elastic materials that exhibit no attractive surface forces (adhesion) and it assumes that the contact radius is much smaller than the sphere radius such that the sphere can be approximated as a paraboloid.

Adhesion term in measuring contact area between two smooth bodies is mainly introduce by JKR and DMT model, both work at different level of applied load and size of adhering

particles. The details of JKR and DMT models have already been discussed in previous sub-chapter. The JKR and DMT both models neglect the surface roughness, which causes a non-uniform pressure distribution across the real contact area. All engineering surfaces are not perfectly smooth and possess finite roughness. When two rough surfaces are pressed together, a contact is made by the asperities on both surfaces. This leads to the smaller real contact area than the nominal contact area. In order to determine the real contact area and separation between contacting surfaces, several studies has been done. The most convenient one is probabilistic approach, which is based on incorporating the behavior of a single asperity in a statistical model of a multiple asperity contact. The pioneer work in this aspect is the one by Greenwood and Williamson (GW model) [23].

The GW model is a classical work and based on the Hertz solution [2] for a single elastic sphere. In the GW model, the contact of two rough surfaces is represented by an equivalent single rough surface in contact with a smooth plane. It is assumed that the asperities population has random height distribution and spherical summits all having a constant radius. Additional assumption of the GW model is neglecting the bulk deformation and interaction between neighboring asperities. If there are N summits in the nominal surface area A_0, the number of summits in contact at separation d is given by

$$n_a = N \int_d^{\infty} \phi(z_s)\, dz_s. \tag{2.50}$$

GW model assumed that the asperity summits are spherical with a constant curvature (κ_s). For asperities whose height (z_s) exceeds the separation (d_s), the total real area of contact (A) and the total nominal pressure $\bar{p}$ (=P/A_0) are

$$A = N \int_{d_s}^{\infty} f(z_s - d_s)\phi(z_s) dz_s, \tag{2.51}$$

$$\bar{p}A_0 \equiv P = N \int_{d_s}^{\infty} g(z_s - d_s)\phi(z_s) dz_s \tag{2.52}$$

where the function $f(z_s - d_s)$ and $g(z_s - d_s)$ depend upon the material properties of the surfaces. If the deformation is entirely within the elastic limit, then applying Hertz theory in equation (2.51) and (2.52) will results into

$$f(z_s - d_s) = \pi(z_s - d_s)/\kappa_s, \tag{2.53}$$

$$g(z_s - d_s) = \left(\frac{4}{3}\right) E^* \kappa_s^{-1/2} (z_s - d_s)^{3/2} \tag{2.54}$$

GW evaluated above integrals numerically for elastically deforming asperities (equation (2.54)) and a Gaussian distribution of asperity heights. Finally the ratio of the real to apparent contact area is given by

$$\frac{A}{A_0} = \left(\frac{\pi}{\sigma_s \kappa_s}\right)^{1/2} \left(\frac{P}{A_0 E^*}\right). \tag{2.55}$$

Thus the real contact area is proportional to the load and real mean contact pressure becomes nearly constant as

$$\bar{p} = \frac{P}{A} = 0.56 E^* \sqrt{\sigma_s \kappa_s}. \tag{2.56}$$

The novelty of the GW study is that the mode of deformation (elastic or plastic) depends mainly on a plasticity index (ψ) which can be proposed as the main contact property. The plasticity index is defined as

$$\psi = \left(\frac{E^*}{H}\right) \sqrt{\sigma_s \kappa_s}. \tag{2.57}$$

According to the GW model, the predominately elastic contact is expected if $\psi < 0.6$. For $\psi > 1$, which is the case for most of the rough surfaces, plastic flow will occur even at trivial nominal contact pressures. It was shown by Greenwood and Tripp [24], using symmetry considerations, that the contact between two rough surfaces can be modeled by a contact between an equivalent single rough surface and a flat. Hence GW model is mainly suitable for pure elastic contacts. There are also available some literature for predominately plastic contact models emerged from the work of Abbott and Firestone [68] that related the bearing area of a rough surface to its geometrical intersection with a flat.

The prediction made by GW model is mainly suitable for predominantly elastic contacts and it is also neglected the adhesion phenomena. Besides elastic contact models, several studies have been done for fully plastic contact as an example Abbott et al. [68]. The models, predominately elastic and predominately plastic contact, are not considered a wide intermediate range of interest where elastic-plastic contact prevails. In order to bridge this gap, the first attempt was made by Chang et al. [25, 26] (CEB model). This model is based on the GW model and volume conservation law for asperities. According to the CEB model,

asperities are within elastic Hertzian contact until a critical interface (ω_c) is reached, above which volume conservation of asperity tip is imposed and a uniform average contact pressure is assumed. With interface (ω) greater than ω_c, plastic deformation is occurred. The ω_c at the inception of plastic deformation is

$$\omega_c = \left(\frac{\pi KH}{2E^*}\right)^2 R \tag{2.58}$$

where K is a hardness coefficient, given by $K = 0.454 + 0.41\nu$. The dimensional less critical interfacial (ω_c^*) is another form of the plasticity index, presented by the GW model, in the form

$$\psi = \left(\omega_c^* \frac{\sigma}{\sigma_s}\right)^{-1/2}. \tag{2.59}$$

The CEB model predicts a fully plastic contact when $\psi \geq 2$. The assumption made by CEB model leads a discontinuity in the contact load at the transition from elastic to elastic-plastic contact. In CEB model, the static friction for dry rough surfaces is based on the adhesion force term in to defining the friction introduced by Tabor. It defines the static friction coefficient in the form

$$\mu = \frac{Q_{max}}{F_{ext}} = \frac{Q_{max}}{P - F_s} \tag{2.60}$$

where Q_{max} is the static friction or tangential force needed to shear the junctions between the contacting surface asperities, F_{ext} is the external normal force, P is the contact load, and F_s is the intermolecular adhesion force. CEB friction model is employing the stress field of Hamilton [69] to calculate the maximum tangential load, which can be supported by a single spherical asperity before plastic yield first occurs either below or at the asperity contact interface. Then the total tangential load, which could be cause of first yield of an entire population of contacting asperities of rough surfaces, would calculate in the statistical model. This tangential load is assumed to be the static friction force at sliding inception of contacting rough surfaces. For smooth surfaces the static friction coefficient depends on the applied normal load, which is contradictory of classical law of Amontons. The CEB friction model underestimates the static friction coefficient, especially for higher plasticity contact, because it neglects the ability of plastically deformed asperities to resist additional tangential loading. Several modifications (e.g. Evseev et al.[27], Chang et al. [28], and Zhao et al. [29]) in

original CEB model were made. The CEB model was also extended to different contacting surface geometries, asperity shapes, and asperity height probability density function by Kogut et al. [29], Horng et al. [30], Yu et al.[30]. However, all these works do not provide a solution to the basic problem of lacking accuracy in the elastic-plastic contact regime.

Kogut et al. (KE model) [31, 32] provided an improved elastic-plastic model for the contact of rough surfaces that is based on an accurate finite element method (FEM) solution of a single asperity contact. It provides the contact parameters such as separation, real area of contact, and real contact pressure as function of the plasticity index and contact load. The dimensional less critical interfacial (ω_c^*) is another form of the plasticity index, presented by GW model, in the form of

$$\psi = \left(\omega_c^* \frac{\sigma}{\sigma_s}\right)^{-1/2} = \frac{2E^*}{\pi KH}\sqrt{\frac{\sigma_s}{R}}. \tag{2.61}$$

It can be seen that the plasticity index depends on surface roughness and material properties. Rougher and softer surfaces can have higher plasticity index; for an example, polished smooth aluminum sample shows a high plasticity index value. According to KE model, the plasticity index ψ is the main dimensionless parameter that affects the contact of rough surfaces. Up to $\psi = 0.6$ the contact is predominately elastic, $\psi = 1.4$ is the critical value for the transition from elastic to elastic-plastic, and $\psi = 8$ is considered to the transition of the contact problem from elastic-plastic to predominately plastic. Jackson et al. (JG model) [70] extended the single asperity contact KE model to a very high deformation up to values of a/R =0.41, where a and R are the contact radius and radius of the sphere. According to JG model, the fully plastic average contact pressure or hardness, which is commonly approximated to be a constant factor of about three times the yield strength, actually varies with the deformed contact geometry, which in turn is dependent upon the material properties (example yield strength). On the basis of his previous finding [70], Jackson et al. [71] introduced a statistical multi-asperity model for contacting rough surfaces covering a large range of the plasticity index up to 100. Several other contact models for rough surfaces can be found in the literature [72-79]. However a common feature in all these investigations is the assumption of a frictionless asperity contact.

Kogut et al. (KE friction model) [80] presented a semi analytical approximated solution for the sliding inception of a deformable sphere in either elastic or elastic-plastic contact with a rigid flat under combined normal and tangential loading. The KE friction model followed the

sliding inception as a plastic yield failure mechanism using the von Mises Yield criterion similarly the CEB model. In this model, an entire plastic volume is allowed to evolve and expand to the sphere surface before the sliding inception. The model assumed that the contact area, the interference, and the contact pressure distribution due to the normal preload (under slip condition) remain constant during the additional tangential loading. A limiting normal preload, of about 14 times the critical load for yielding inception is found, above which the contact cannot bear any additional tangential load. According to KE model, the static friction coefficient is having the relation with applied normal load in the following manner,

$$\mu = 0.516\left(\frac{P}{P_c}\right)^{-0.345} \tag{2.62}$$

for $0 < P/P_c \leq 1.03$, and

$$\mu = -0.007\left(\frac{P}{P_c}\right)^{2.104} + 0.083\left(\frac{P}{P_c}\right)^{1.405} - 0.380\left(\frac{P}{P_c}\right)^{0.701} + 0.822 \tag{2.63}$$

for $0 < P/P_c \leq 13.86$, where $P_C = \frac{(\pi K)^3}{6}\left(\frac{H}{E}\right)^2 HR^2$. The KE friction model described the friction force reaches a maximum at about P^* (P/P_c) = 10 and then decreased to zero when P^* reached 14. A limiting normal preload, of about 14 times the critical load for yielding inception was found, above which the contact cannot bear any additional tangential load. This finding is not realistic and indeed correlate only with some limited experiments for $P^* < 10$.

Recently, Brizmer et al. (BKE friction model) [81] presented an analytical solution for elastic-plastic spherical contact under combined normal and tangential loading in full stick condition. In this model the sliding inception is associated with a loss of the tangential stiffness of the loaded asperity. According to the KE model, the static friction coefficient is having the relation with applied normal load in the following manner

$$\mu = 0.27\coth\left(0.27(P^*)^{0.35}\right) \tag{2.64}$$

where $P^* = P/L_c$ and $L_c = (8.88\ \nu - 10.13(\nu^2 + 0.089))(\pi C_v Y_0)^3\ (R(1-\nu^2))^2/6E^2$ and C_v is function of Poisson's ratio and given as $C_v = 1.234 + 1.256\nu$. In the summary of the BKE model, the static friction coefficient decreases sharply with increasing normal load in the early elastic-plastic loading range where $P^* \leq 20$. At higher normal loads ($P^* > 50$), where the static friction force, Q_{max}^* becomes nearly proportional to P^*, the rate of decreasing the friction

coefficient diminishes, and at $P^* = 200$ the static friction coefficient approaches a constant value (validating the Coulomb's friction law at such high dimensionless loads) of about 0.27.

Ovcharenko et al. [82] investigated experimentally the static friction in spherical elastic-plastic spherical contact, showing good correlation with the corresponding the BKE friction model [81] for dimensionless normal loads, $P^* > 50$. At low level of loads, the finding reveals the large discrepancies between experimental and the theoretical model. Ovcharenko et al. observed that in the elastic regime of deformation and as possible polished smooth surface, the friction coefficient increases with decreasing dimensionless normal load up to a certain level and then sharply increases with further decreasing of the dimensionless normal load. The actual level of the static friction coefficient in this elastic regime of deformation seems to depend on the sphere material, its diameter, and surface roughness or plasticity index. Cohen et al. [83, 84], therefore, developed a theoretical model for elastic-plastic spherical contact with real rough surfaces.

Cohen et al.(CKE model) [83] presents an empirical equation for static friction coefficient as a function of the normal load, material properties, and surface roughness. The friction coefficient including the roughness parameter as plasticity index (ψ) given by the Cohen et al. (CKE model) [83] is calculated as

$$\mu = \left(0.26 + \frac{0.43}{\psi}\right)(P^*)^{0.0095\psi - 0.09} \tag{2.65}$$

This plasticity index (ψ) is calculated as $(2E^*/\pi C_v(1-\nu^2)Y_0)(\sigma_s k_s)^{1/2}$. This expression provides a useful empirical prediction of the friction coefficient when the mechanical properties, surface roughness, nominal contact area, and normal load are known. At the maximum plasticity index $\psi = 8$, the model showed a realistic static friction coefficient value higher than that predicted by the KE friction model. The results the predicted by CKE model is well correlated with the experimental results by Ovcharenko et al. [82]. However this finding is limited to $\psi < 8$ and this investigation extends for rough surfaces with a high plasticity index by Li et al. [85]. This was accomplished by accounting more accurately for fully plastically deformed asperities using the finite element results of [70]. This model also correlates some deficiencies of the earlier model at very small plasticity index values below 0.5. Li et al. presented an empirical equation for static friction coefficient as a function of the normal load, material properties, and surface roughness. The static friction coefficient of nominally flat rough surfaces and rough spherical surfaces calculated as in equation (2.66) and (2.67), respectively,

$$\mu = (0.26 + 0.32\exp(-0.34\psi^{1.19}))(P^*)^{-\exp(-1.9\psi^{0.4})} \quad (2.66)$$

$$\mu = (0.26 + 0.61\exp(-0.74\psi^{1.4}))(P^*)^{-0.21\exp(-0.07\psi^{2.29})} \quad (2.67)$$

This plasticity index (ψ) is calculated as $(2E^*/\pi C_v(1-\nu^2)Y_0)(\sigma_s k_s)^{1/2}$. This expression provides a useful empirical prediction of the friction coefficient when the mechanical properties, surface roughness, nominal contact area and normal load are known. In literature several other static friction models for rough surfaces can be found [86-90]. A common feature in all above static friction model is that the static friction coefficient decreases with increasing normal load.

With the advent of Nanoindenter since two decades provides an unprecedented capability for probing the mechanical as well as tribological properties of materials over a wide range of length scales from nm to mm and force from nN to mN. This force-displacement sensing instruments also allows the studies of creep, dynamic loading, thin film behavior, fracture, and adhesion. A good summary is presented in ref [1, 91, 92]. Flores el al. [93] presented an outline a mechanistic framework for interpreting measurements from scratch tests on elastic-plastic materials with spherical indenters. According to Flores et al. [93], at sufficient low level of load, wherein the contact is elastic, sliding occurs subjected to Coulomb's law, with constant friction coefficient. At high level of applied load, wherein the contact and sliding involve plastic deformation, the friction coefficient increases with increasing normal load (figure 2.7). At intermediate range of applied normal load, where the deformation involves of elastic and plastic deformation, the friction coefficient changes accordingly as shown in figure 2.7.

Nanoindenter based scratching proceeds in two steps. Initially, a rigid spherical indenter of radius (R) is pushed into a flat surface of rigid, perfectly plastic material with normal force (P). The contact radius (a) of the resulting indentation is given by [94]

$$a = \sqrt{C_1 R u_0} = \sqrt{\frac{P}{C_2 \pi \sigma_y}} \quad (2.68)$$

where u_0 is the maximum penetration depth of indenter in to flat surface, σ_y is the material yield strength, $C_1 = 2.7$, and $C_2 = 3.0$. The indenter is then moved laterally while maintaining constant normal force. Three additional assumptions are invoked: (i) The sliding at the interface between the two bodies obeys Coulomb's law, (ii) The scratch depth u_s is equal to

the initial indentation depth u_0, and (iii) The forces at the indenter/material interface remain below those needed to produce sticking friction.

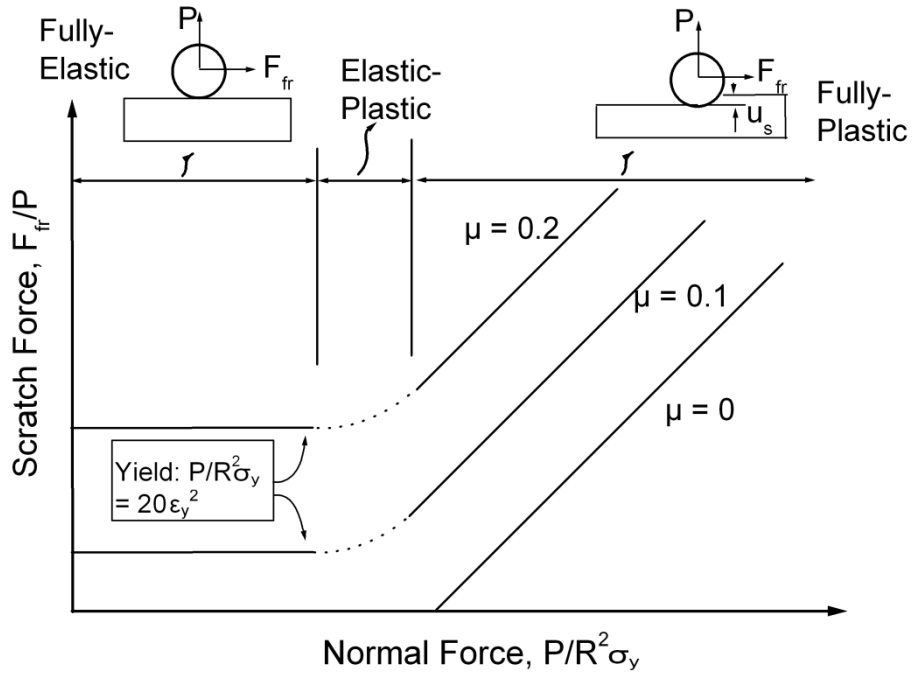

Figure 2.7: The trend in scratch force with normal force and friction coefficient.

In the steady-state domain, the rate of work done by scratching, $dW/dx = F_{fr}$, can be partitioned into two components: one, dW_p/dx, due to plastic deformation beneath the indenter tip, and another, dW_f/dx, from frictional sliding, where indenter moves in x-direction. Eventually the rate of work done is

$$\frac{dW}{dx} = F_{fr} = \int_0^{u_0} p(u)du + \mu P \tag{2.69}$$

where p(u) is the force per unit length of cylinder, given by

$$p(u) = 2a\sigma_y C_3 \tag{2.70}$$

where $C_3 \approx 2.5–3$ [33]. Combining equation (2.69) and (2.70) and integrating yields

$$\frac{F_{fr}}{P} = \mu + k_0\sqrt{\frac{P}{R^2\sigma_y}} \tag{2.71}$$

where $k_0 = 4C_3/3C_1(\pi C_2)^{3/2} \approx 0.05$. This relation identifies the two pertinent nondimensional parameters: the normalized scratch force (F_{fr}/P) or measured friction coefficient (μ) and the normalized normal force ($P/R^2\sigma_y$). Flores et al. provides critical loads for a predominantly

elastic (nondimensional normal load, $\sqrt{P/R^2\sigma_y} < 5\varepsilon_y$) and predominantly plastic contact (nondimensional normal load, $\sqrt{P/R^2\sigma_y} > 15\varepsilon_y$). However, this model underestimates the apparent friction coefficient, especially for the ultra low load regime, as the apparent friction coefficient decreases with increasing load as Hertzian behavior.

During Nanoindenter based scratch measurements, one can control the normal load value, the lateral tip position, the loading rate and the tip sliding speed (the tip's lateral speed). Labdi et al. [95] reported the effect of lateral tip displacement direction and normal force loading mode on lateral force measurements. The finding showed how the loading rate, rather than the sliding speed, is a very important parameter in the case of ramping load scratch tests. According to this finding during nanoscratch measurements, normal tip displacement is controlled by the normal force loading rate. The lower loading rate provides the higher value of normal displacement. Therefore the friction coefficient must increase on decreasing loading rate. This behavior seems to be universal and not related to material hardness and the Young's modulus.

Wong et al. [96] studied the wear behavior of an amorphous $Fe_{81}B_{13.5}Si_{3.5}C_2$ and reported that its wear rate increased with sliding speed, which was explained by the structural changes caused by in-situ adiabatic heating during sliding. It has been noted that the sliding speed used by Wong et al. is very much higher than that the one which have been used in in thesis work. Thus, in-situ adiabatic heating effect is expected to be much less significant. However, Imura et al. [97] reported that wear is independent of sliding speed. In fact, the ware rate of many crystalline metals is also independent of sliding speed [98]. Recently, Hodge et al. [99] evaluated the abrasive wear of several amorphous alloys and found the scratch velocity appeared to exert little effect on the wear behavior. The finding reported that the scratching speed is having little effect on the friction coefficient. More recently, Huang et al. [100] studied the mechanical performance of metallic glass during nanoscratch tests and according to finding the scratch velocity appears to have little effect on the scratch depth and faster scratch velocity leads to fined shear band.

Gossilloud et al. [101] studied the phase transformation of silicon during nanoscratching process and found that the applied load and the scratching velocity strongly influence the deformation mechanism. Gossilloud et al. found two deformation regimes, an elastic-plastic regime at low loads and a fully plastic regime at higher load during slow scratching. In their

studies, the silicon nanocrystals are embedded into amorphous matrix at low speed, whereas at high speeds the transformed zone is completely amorphous.

Briscoe at el. [102] proposed that the deformation velocity ($\dot{\varepsilon}_s$) in the scratching can be defined as the ratio of the scratching velocity (v) to the scratching width (b) and the decompression rate ($\dot{\sigma}_s$) may be defined as

$$\dot{\varepsilon}_s = \frac{v}{b} \tag{2.72}$$

$$\dot{\sigma}_s \approx \frac{2vP_m}{b} \tag{2.73}$$

where P_m is the mean contact pressure under the indenter and is defined as follows

$$P_m = \frac{P}{A} = q\left(\frac{4P}{\pi b^2}\right); \quad 1 < q < 1 \tag{2.74}$$

Gossilloud et al. [101] proposed the coefficient (q) value as 2 in equation (2.74) expresses the fact that the decompression takes place at rear half of the contact circle. Briscoe et al. [102] proposed that for rigid plastic material such as metal, q = 2 and for materials such as polymers with high elastic release, q = 1. In present study, the applied normal load is in elastic contact regime and then q = 1 is used. For constant scratching width, the decompression rate will be proportional to scratch speed ($\dot{\sigma}_s$ α v) and decompression will increase with scratch speed and thus scratching speed will influence on tribological contact.

The aforementioned findings have shown that at low level of applied load, a decreasing friction coefficient with load is observed, followed by a constant friction coefficient. In contrast at high level of applied load, an increase friction coefficient with load is found. In other words, an elastic contact behavior along with transition regime between elastic and plastic contact is observed, followed by a plastic deformation dominated normal load regime. The critical load range for transition from elastic to plastic contact regime is mainly dependent on the mechanical properties of contacting bodies and radius of probe for perfectly smooth surface as mentioned in ref [93]. By scratching on real rough surfaces, the yield of asperities deformation occurs at lower applied load and critical load range can change, which is not studied so far. Additionally the adhesion force provides an additional normal load when two bodied are in contact and leads to an existence of lateral force at nonzero applied load. The adhesion force is again dependent on the surface roughness, and other parameters. The

external parameters such as scratch speed and loading rate change the stress field and results in to different critical load range. The study to identify the individual as well as combined contribution of surface roughness, adhesion force, and mechanical properties in the tribological properties, particularly how the critical load range changes, is not done yet.

In order to study the effect of these parameters on tribological characterizations, AFM and Nanoindenter based tribological tests with various operating conditions are performed on various rough surfaces. The details of the experiments will be discussed in chapter 3. In chapter 3, first preparation techniques of analyzed samples and probes along with the radius calibration of probes are discussed. The instruments, which are mainly used in this thesis, are described in detailed. A basic aspect involved in AFM and Nanoindentation technique is presented. A description of normal load as well as lateral force calibration for AFM and Nanoindenter are also presented. Further in this chapter, data analysis for surface roughness, mechanical properties, adhesion force, and tribological test are presented. Chapter 4 presents the results and discussion and followed by the summary and outlook of the work in chapter 5.

Chapter 3 Experimental details

In this chapter, first preparation techniques of analyzed samples are discussed. Next the preparation techniques along with the radius calibration of probes are discussed. The instruments, which are mainly used in this thesis, are described in detailed. Finally data analysis for surface roughness, mechanical characterization, adhesion force, and tribological test are presented.

3.1 Analyzed samples

The homogeneous, amorphous, and isotropic samples are selected. The thickness of coating films are selected few hundreds of nanometers to few micrometers to prevent the substrate effect in the measurements. The amorphous and homogeneous fused silica sample is mainly used. Other amorphous coating systems such as diamond-like-carbon films (DLC) and Si-C-B-N-O coatings are used. The amorphous and homogeneous DLC samples featuring different surface roughness are selected for roughness effect on tribological characterization. The Si-C-B-N-O films are selected to study the effect of mechanical properties on tribological characterization. The amorphous silica particles and self-assembled monolayers (SAMs) are chosen for characterization of adhesion forces for particle-particle and particle-flat surfaces, and to study the effect of adhesion force on tribological characterization. Silica particles are also used to prepared colloidal probes, which will be discussed in later part of this chapter. Apart from amorphous samples, smooth and polished non-amorphous silicon and aluminum samples are used. Aluminum sample is selected to study the tribological characterization in predominantly elastic as well as plastic contact regime. In this sub-chapter, the synthesis techniques analyzed samples are discussed in detail.

3.1.1 Fused silica, Aluminum, and Silicon

The fused quartz or fused silica is used as a reference material in calibrating the tip area function for Nanoindenter tip. In literature, there is an argument on the difference between fused silica and fused quartz. Both are chemically identical, but differ in their manufacturing process. Fused quartz is manufactured by melting naturally occurring quartz crystals of high purity at approximately 2000 ˚C using either an

electrically heated furnace or a gas/oxygen-fuelled furnace. Fused silica is produced by melting high-purity silica sand using an electric furnace. A clean and transparent fused silica sample is provided by Hysitron Inc. The fused silica sample of about 10X10 mm^2 and 2 mm thick is glued on iron plate. The fused silica is used for pull-off force and scratch tests. The commercially available metallic aluminum (100) sample is optically polished single crystal. An aluminum sample of 10 mm diameter and 2 mm thick is glued on the iron plate. The aluminum sample is used for scratch tests. The clean and standard silicon wafer (100) is used as silicon sample. The silicon wafer is one side mirror polished single-crystalline (100). The silicon wafers are 1 mm in thickness. As obtained 2 inch silicon wafers are cut into smaller pieces and then glued on iron plate. The silicon sample is used for pull-off force tests. These sample surfaces are considered to be perfectly smooth and are featured without any bumps or grooves.

3.1.2 Diamond like Carbon (DLC)

For deposition of the thin DLC films the plasma enhanced chemical vapor deposition (CVD) is used. The preparation is carried out using a commercial sputtering plant (Balzers BAS 450). The DLC samples are deposited on silicon substrates by Ar+ operated in dc mode at a power of 1.5 kW. A gas mixture of Argon and Acetylene is fed into the deposition zone. A constant flow of the gas mixture is maintained at a working pressure of 0.47-0.50 Pa. The process is performed under negative bias voltage of 200-950 V. Substrate heating by the ion bombardment could be maintained around 200 ˚C at a bias of 100 V. The DLC samples are used for pull-off force and scratch tests.

3.1.3 Si-B-C-N-O Coatings

The Si-B-C-N-O films are deposited on range of substrates including silicon (100) wafers, WC-10%Co, Ni- and Ti-base alloys using electron cyclotron resonance (ECR) microwave plasma assisted chemical vapor deposition (MWCVD). Microwaves of 2.45 GHz are guided into the ECR excitation chamber via a quartz window. A divergent 87.5 mT magnetic field guides the plasma stream toward the substrate which is placed in a second chamber beneath the ECR zone. When required, the substrate is negatively DC- biased at low 30V to assist film growth. A gas mixture of BF_3–N_2–Ar–He is fed into the ECR excitation zone while H_2 and$Si(CH_3)_4$ are introduced into the elastomer-sealed reaction chamber underneath the ECR zone. Prior to the deposition, the reactor is pumped to a base pressure of

about 5×10^{-3} Pa and the substrates are resistively heated to about 800°C. The deposition conditions are listed in table 3.1[103]. These samples are used for scratch tests.

Table 3.1: A summary of coating composition and deposition parameters.

Gas composition	SiCN	SiBCN
$Si(CH_3)_4$ (1.15% in H_2)	10- 100 sccm	10- 100 sccm
CH_4	0- 5.8 sccm	0- 5.8 sccm
N_2	0- 11.5 sccm	0- 11.5 sccm
BF_3/ (10% in Ar)	0 sccm	2.8- 11.5 sccm
He	20 sccm	20 sccm
T_{sub}	800 °C	800 °C
V_{sub}	- 30 v	- 30 v
Pressure	2.1- 3.3 Pa	2.1- 3.3 Pa
Microwave power	300-1450 W	300- 1450 W

3.1.4 Silica microspheres and self-assembled monolayers

The borosilicate silica microsphers (silica particles) are provided by 9020, Duke Standard™. The radius of silica particles are 9.21 ± 0.73 μm and 2.63 ± 0.17 μm. Preparation of self-assembled monolayers (SAMs) using these silica particles are demonstrated in ref [104, 105]. In order to prepare SAMs, first, the suspensions of silica particles are prepared in acetone. SAMs of silica particles are then obtained by dipping glass substrates into a well dispersed silica particles suspension. The suspension is dispersed in an ultrasonic bath and with a magnetic stirrer before dipping. The substrate must be vertically dipped into the suspension for 1-3 minutes and withdrawn at a programmed speed during the coating process. Different homogeneity of SMAs on glass slide is obtained by varying the dipping time and withdrawn speed. Homogeneous SMAs are obtained by repeating the procedure and changing the dipping times. SAMs are used for pull-off force tests.

3.2 Probes

The tribological characterizations are carried out with spherical probes on analyzed flat surfaces. The diamond and silica spherical probes are selected and they are referred as diamond conical indenters and silica colloidal probes (adhering particles), respectively. Later the terminologies indenter and colloidal probe will be used in this thesis, respectively. The adhering particle term is used in adhesion force measurement. The diamond indenters are stiff

and rigid and used to apply load range from hundreds of nN to few mN loads with Nanoindenter. Silica colloidal probes are stiff and rigid and selected for apply load range from tens of nN to few µN loads with AFM. Nanoindenter and AFM will discuss in detail in next sub-chapter. Two different sizes of diamond indenter are used in tribological testing and their size calibration is discussed in this sub-chapter. Four different size of colloidal probe are used to measure the adhesion forces and among them two colloidal probes are used for tribological testing. In this sub-chapter, the preparations of colloidal probes as well as their actual radius calibration are presented.

3.2.1 Conical diamond indenters and their tip radii calibration

Two commercially available conical diamond indenters of nominal radii of 1 and 20 µm are used. The diamond conical indenter with 90° cone opening angle features a perfect spherical tip at the apex. The figure 3.1 shows an AFM image of a diamond indenter.

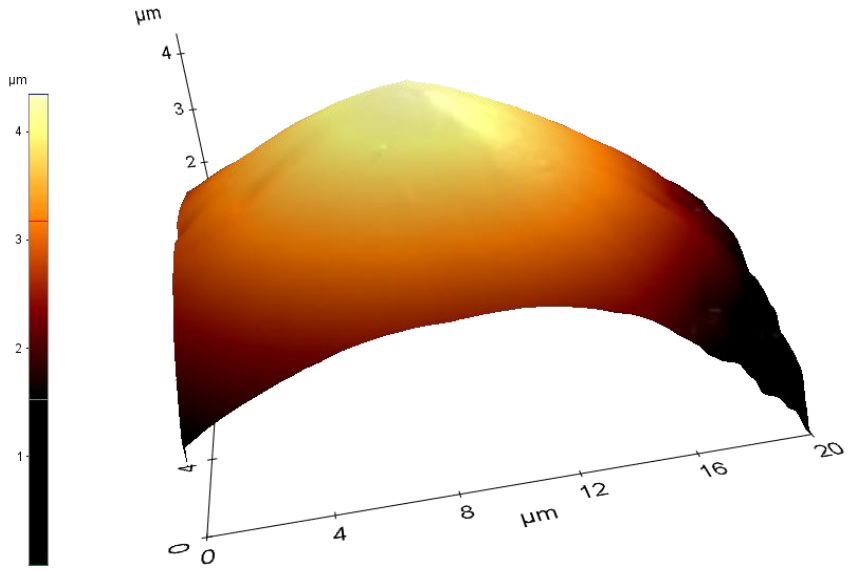

Figure 3.1: An AFM image of a conical diamond indenter.

Prior to use them, their actual radii must be measured. The actual radius of diamond indenter is calculated by fitting of Hertz equation in load vs. displacement data for known material (fused silica). Nanoindenter generates the measured load (P) values corresponding to indentation depth (d) for fused silica, as shown in figure 3.2. For ultra-smooth surfaces and in predominantly elastic contact regime, the Hertz theory can be apply here [2]. For a spherical probe the applied load (P) is having relation with displacement (d) as equation (3.1).

$$P = \sqrt{\frac{16\,R\,E^{*2}}{9}}(d + d_0)^{3/2} \tag{3.1}$$

where E^* is 69.6 GPa for fused quartz and diamond system, d is displacement of indenter corresponding to applying load (P), and R is radius of indenter, and d_0 is initial penetration depth.

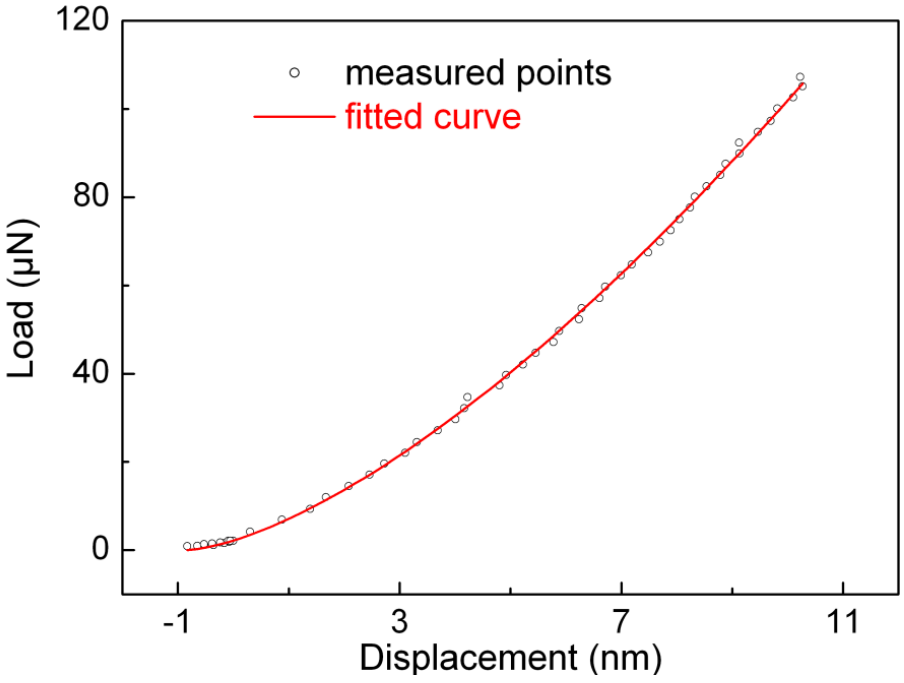

Figure 3.2: Load vs. displacement. Measured points were generated from Nanoindentation test using one of the conical indenter. The fitted curve was generated using Hertz equation (3.1).

The radius of indenters can be calculated by fitting equation (3.1) in measured curve of P vs. d, as shown in figure 3.2. The resulting radius at various load are calculated and are plotted in figure 3.3. The corresponding average actual are about 0.7 μm and 4.5 μm for 1 and 20 μm indenter, respectively as table 3.2. The above actual tip radius values are confirmed by AFM images. Later on these real radii will be used in context of all calculations.

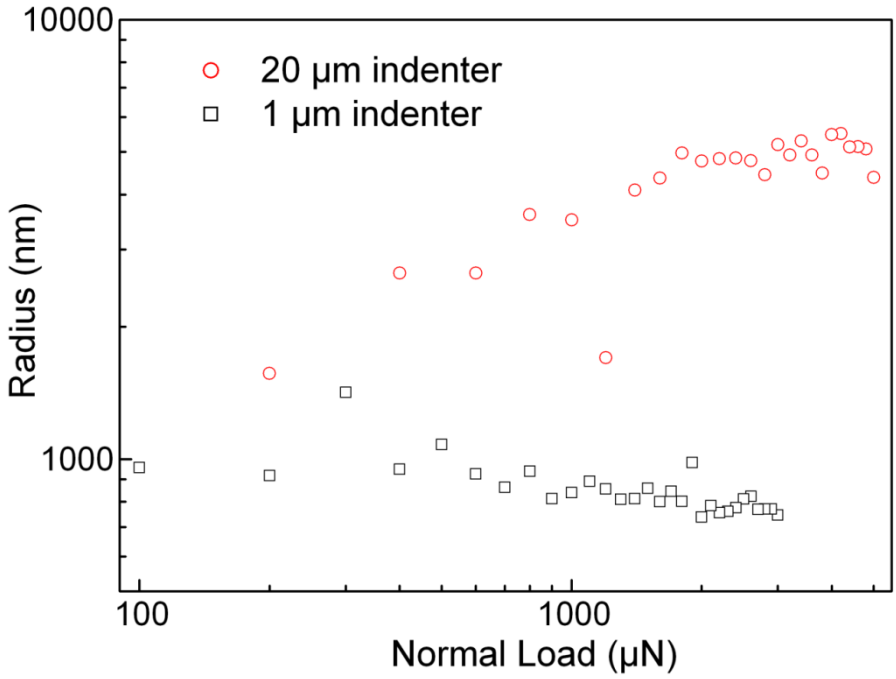

Figure 3.3: Radius corresponding to load for (a) 20 µm and (b) 1 µm conical indenter.

Table 3.2: Tip radius of diamond conical indenter

Indenter	Nominal Radius (µm)	Calculated Radius (µm)
20 µm indenter	20	4.5
1 µm indenter	1	0.7

3.2.2 Silica Colloidal probe

In the force measurement application a colloidal probe technique, a silica micro particles (glued to a tipless AFM cantilever), is used to probe an interface instead of the usual AFM cantilever tip. As standard tips are typically limited because the contact area between a tip and surface is very small, the alternative choice of a microscale colloidal probe can allow the user access to a much smaller stress regime and broader choice of probe materials. The colloidal probe application has found frequent use in the study of tribological phenomena. This thesis focuses on the AFM friction measurement technique called lateral force micrcscopy (LFM) using colloidal probes. Colloidal probes are prepared by gluing (Araldite 10-min, 2 components, Epoxy) silica particles (9020, Duke Standard^{TM} Borosilicate Glass Microspheres) of various radii onto tipless cantilevers (Mikromash, NSC12). Direct

attachment, gluing of spherical multi-micron size particles to the AFM cantilevers is demonstrated first in [66]. A typical colloidal probe is shown in figure 3.4.

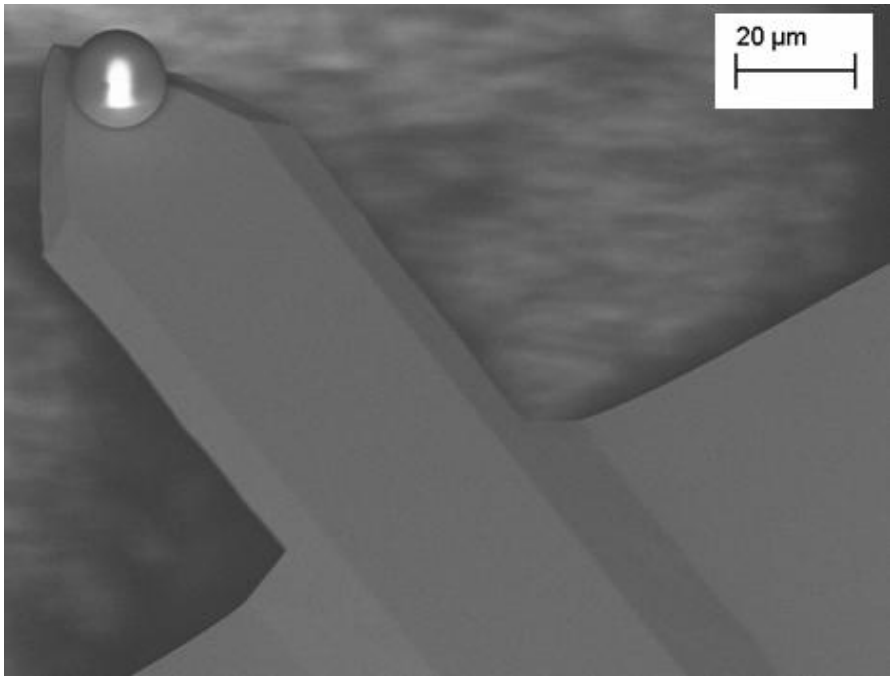

Figure 3.4: SEM image showing a top view of the silica micro particle glued onto the end of the cantilever.

The different size of colloidal probe ranged from 1 and 10 µm in radii are prepared. The radii of colloidal probes are measured with scanning electron microscopy (SEM) and their actual radii are 1.45, 2.78, 7.59, and 10.25 µm.

3.3 Instruments

As mentioned earlier, the analyzed samples are synthesized by dip coatings, CVD, and ECR-MWCVD techniques and their synthesis is not part of this thesis; therefore, these techniques as well as corresponding instruments are not presented. The analyzed samples are characterized by optical microscopy, scanning electron microscopy (SEM), X-ray diffraction (XRD), atomic force microscopy (AFM), Nanoindenter, and other techniques. Optical microscopy and SEM are used to topographical characterization of analyzed samples. XRD technique is used to confirm the crystal structure of analyzed samples. In this thesis, mainly two techniques are used: AFM and Nanoindenter. AFM is used to measure the surface roughness characterization, the adhesion forces for particle-particle and particle-flat surfaces, and the tribological characterization with applied load range from nN to µN. Nanoindenter is

used to mechanical characterization and tribological characterization with applied load range from µN to mN. So it is important to discuss in detail of both techniques. In this sub-chapter, the details of both instruments are briefly discussed.

3.3.1 AFM setup

AFM is a scanning probe technique which measure the interaction forces between the probe and the sample surface such as Van der Waals, friction, electrostatic, and magnetic forces [106]. It is a high-resolution imaging technique which allows researchers to observe and manipulate molecular and atomic level features. The schematic diagram of an (AFM XE-100, PSIA) is shown in figure 3.5.

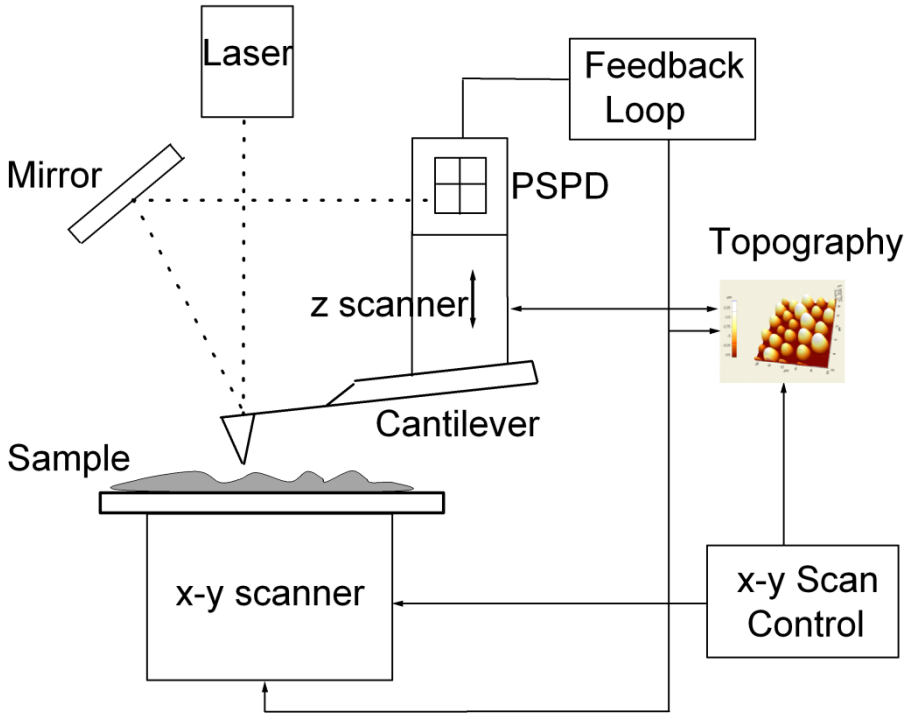

Figure 3.5: A schematic of an AFM setup.

The backside (reflective side) of cantilever is coated with metallic materials like aluminum. A sharp tip is scanned in a raster-pattern along a surface. A laser beam is first focused on the reflective side of a cantilever, then it is reflected to the mirror, and finally to Position Sensitive Photo Detector (PSPD), thus the change in the cantilever deflection during scanning of the sample surface by the tip is monitored with a quadrant photodiode detector. This photodiode detector measures the difference in light intensities between the upper and lower photo detectors, and finally converts in to voltage signal. The x-y scanner located under the

sample moves a sample in the horizontal direction (x-y) and z-scanner located at head of cantilever moves in the vertical direction (z). It is repetitively scans the sample line by line, while the PSPD signal is used to establish a feedback loop which controls the vertical movement of the scanner as the cantilever moves across the sample surface.

Based on tip and sample interaction, there are three primarily working modes: contact mode, tapping mode, and non-contact mode. In the tapping mode AFM, the cantilever is oscillated up and down at or near its resonance frequency with amplitude ranging typically from 20 to 100 nm. Due to the interaction of forces such as Van der Waals force, dipole-dipole interaction, electrostatic forces, etc. the amplitude of cantilever oscillation decreases as the tip gets closer to the sample. An electronic servo uses the piezoelectric actuator to control the height of the cantilever above the sample. The servo adjusts the height to maintain a set cantilever oscillation amplitude as the cantilever is scanned over the sample. This mode allows high resolution topographic imaging of sample surfaces that are easily damaged or loosely hold to their substrate. This mode also uses to define the two phase systems in which both phases shows different stiffness.

In the non-contact mode AFM, the cantilever is oscillated at a frequency that is slightly above the cantilever's resonance frequency with the amplitude of cantilever of < 10 nm. The cantilever must be oscillated above the surface of the sample at such a distance that the repulsive regime of the inter-molecular force curve cannot occur. Non-contact mode AFM does not suffer from tip or sample degradation effects which are usually observed for contact AFM mode. This makes non-contact AFM preferable to contact AFM for measuring soft samples. In the case of rigid samples, contact and non-contact images may look the same. Non-contact mode is a difficult mode in operating it into ambient conditions due to the thin layer of water contamination on the surface which invariably form a small capillary bridge between the tip and the sample and cause the tip to jump-to-contact. This problem exists even under liquids and in vacuum and imaging is most probably done using tapping mode in that situation.

In the contact mode, the tip and the surface remain in close contact during the scanning. In this mode, probe is sensitive to the forces acting perpendicular (normal forces) as well as parallel (lateral forces) to the sample surface. Basically it is static mode operation, where the static tip deflection is used as a feedback signal. This static signal is more pronounced of noise and drift, therefore low stiffness cantilever is usually used.

As mentioned earlier AFM is employed for number of purposes. Topography and surface roughness, adhesion force, and friction force of analyzed surfaces have been investigated using an AFM. Topography is mostly characterized in non-contact mode with commercial available silicon nitrate tip. Adhesion and friction force are measured in contact mode with silica colloidal probes. The detail of these measurements will be discussed in data analysis sub-chapter. In order to extract the absolute values for the adhesion force and lateral force from the experimental data, the cantilever deflection has to be multiplied with the actual spring constant of the cantilever and lateral force calibration factor, respectively. In following two sub-chapters, a brief discussion on spring constant and lateral force calibration factor are presented.

3.3.1.1 Spring Constant

The spring constant is defined as the quotient of the applied force at the cantilever to the displacement deflection of the cantilever at the tip position in the direction normal to the plane of the cantilever. This is the primary factor in determining the accuracy of the measured forces. The nominal values of the spring constant provided by the manufacturers are up to a factor of two or more in error compared to their true value [107]. It is, therefore, needed that quick and accurate methods to determine the spring constant must be available. In present work, the measured cantilever spring constants are significantly different from the nominal spring constant, as listed in table 3.3. The nominal spring constant of tipless cantilever for 1 to 8 μm colloidal probe is 14 N/m with a distribution range from 3.5 to 27.5 N/m. For 10 μm colloidal probe, the tip less cantilever cut by using focus ion beam (FIB) in manner such that it can provide high spring constant and generate high load range for application. After gluing the silica particles on cantilevers, it is necessarily to measure the actual spring constant of colloidal probe.

There are several methods to determine the spring constant with their some advantages and disadvantages. These are mainly categorized into 3 general groups: dimensional, static experimental and dynamic experimental [108]. In literature these are also categorized in four groups [109]. In dimensional methods, the spring constant is determined from the cantilever material and geometrical properties. Sadel et al. [110] have used finite element analysis (FEA) to calculate spring constant and Neumeister et al. [111] provided the equations for solving the spring constant. Clifford et al. [108] also extended the Neumeister et al. [111] solution. The geometrical and material properties are not easy to determine and FEA is time consuming.

The metallic coating at back side of cantilever also add the difficulties to determine the actual spring constant. In static experimental methods [112-120], a constant force is applied to the cantilever and then measuring the deflection of cantilever. These methods are required a pre-calibrated reference cantilever beam to push on the measuring cantilever or vice versa. In dynamic experimental methods [121-124], the spring constant can be calculated using the cantilever's resonant frequency combined with other measurements. These other measurements could involve attaching masses to the cantilever to measure the change in the resonant frequency or knowing some material properties.

As far it is well understood that all kind of spring constant measuring method are having some disadvantageous, however measuring the spring constant using a commercial Nanoindenter [117] is fast and simple, except that the instrumentation needed is expensive. This technique uses a Nanoindenter to calibrate a rectangular cantilever. The diamond tip for the Nanoindenter has been used to push down on a cantilever to obtain force-displacement curves. From the force-displacement curve of an indent, the spring constant can be calculated. Applied load should be small enough such that the actual indentation made in the surface of the tip is negligible. The compliance of the AFM/Nanoindenter combination should be negligible compared to the cantilever. These assumptions are reasonable in present study. The deflection of the cantilever on applying the normal load is not too large enough to change the angle. The indenter tip is ideally pressed against the cantilever at the point on the backside of the lever exactly above the tip. This is difficult due to lack of a clear optical path around the indenter tip as it contacts the backside of the lever. However Ying et al. [125] improved the technique by integrating an optical microscope at a calibrated distance away from the indenter probe allowing positioning of the probe with micrometer accuracy.

A popular thermal noise method [121] to determine the spring constant of the cantilever is also available. In this method, the spring constant (k) is determined by fitting the power spectrum of the colloidal probe thermal noise to a simple harmonic oscillator response with added white noise. This method allows the spring constant to be determined as

$$k = \frac{2k_B T}{\pi A_m^2 f Q} \tag{3.2}$$

where k_B is Boltzmann's constant, T is the temperature, f is resonant frequency, Q is quality factor of the resonant frequency peak of the cantilever, and A_m is amplitude. In this method, the cantilever end is kept far from the surface and it is free to oscillate at its natural resonant

frequency. This method is usually performed with cantilever in air with the default inverse optical lever sensitivity correction factor of 1.09 [107, 126-128]. This default correction factor is expected to depend upon the focused laser spot size and position on the cantilever [127]. This method allows for the determination of the spring constant by fitting the power spectrum of the cantilever thermal noise to a simple harmonic oscillator response with added white noise. It is a quick and simple process to determine the spring constant using the default thermal noise method via the user interface provided with the Asylum Research 3D MFP AFM.

In this thesis, spring constants of rectangular AFM cantilever are calculated by Nanoindentation method. In this method, AFM cantilever is placed in the sample position. The diamond conical indenter of 1 μm radius indenter is used. The Nanoindenter tip is landed at a certain point along the tested cantilever and then pushed downward with 5-10 μN loads. Applying load is low enough such that the force-displacement curve is linear. A series of indentation with indenter is done at various positions from one end of the cantilever to another end of the cantilever. The spring constant for each indent is calculated as slope of force-displacement curve as shown in figure 3.6 (b). End of it, the spring constants against the indentation distance from one end of the cantilever is obtained. The spring constant starts with very its highest value at fix end, and on increasing the distance from fix end it decreases (figure 3.6 (c)), which can be explained by equation (3.3) of spring constant (k) of rectangular cantilever as

$$k = \frac{Et_c^3 w}{4L_a^3} \tag{3.3}$$

where L_a is the length of the moment arm, t_c is thickness, w is the width, and E is elastic modulus. For cantilever spring constant, w, t_c, and E are fixed and L_a varies from one end to another end and hence spring constant varies. The exact position of probe on the cantilever can be seen by using SEM image as shown in figure 3.6 (a). At the end, the actual spring constant of AFM tip can be calculated by extra-plotting or intra-plotting of spring constant vs. distance curve as shown in figure 3.6 (c). The results are also confirmed with the spring constant from the thermal noise method [121]. The spring constant of used colloidal probes are presented in table 3.3.

Table 3.3: Details of colloidal probes.

Tip	Radii of glued glass spheres (µm)	Nominal spring constant (N/m)	Actual spring constant (N/m)
1	2.78 ± 0.1	14(6.5-27.5)	10.8
2	10.26 ± 0.1	--	100
3	7.59 ± 0.1	7.5 (3.5-12.5)	12.3
4	1.45 ± 0.1	4.5 (2.5-8.5)	3.5

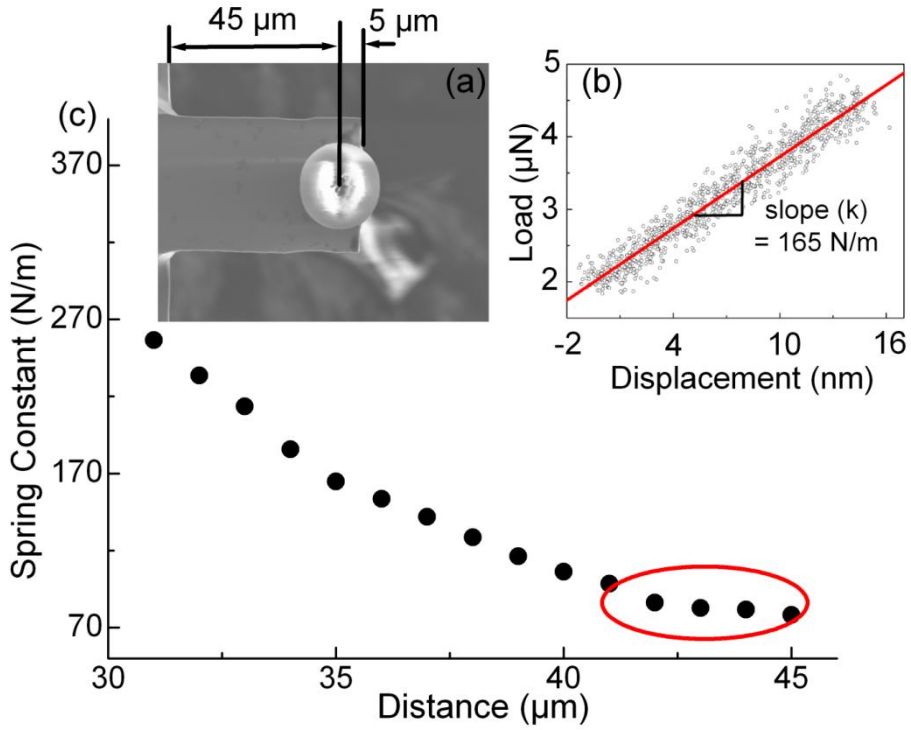

Figure 3.6: (a) SEM image showing a top view of the 10 µm radius sphere glued onto the end of the cantilever. (b) Load-displacement curve showing the spring constant. (c) Spring constant from one end to another end of the cantilever.

3.3.1.2 Later force calibration

The colloidal probe technique has been frequently used in the study of tribological phenomena [129-134]. The quantitative measurement of contact response with an AFM is not directly obtained; it requires complex calibration of normal and lateral forces. The normal force or spring constant is already described in previous sub-chapter.

The lateral force calibration can be performed by either a two-step or a direct procedure. The two-step procedure includes calibration of the cantilever torsion angle that is caused by lateral force acting on its tip end, and determination of the cantilever torsional stiffness. This allows converting the torsion angle into a lateral force. The torsion angle calibration factor is obtained from the slope of a friction loop [135, 136]; however, this is subjected to uncertainty because of the effect of lateral contact stiffness [137] and tip stiffness [138] or by analyzing the optical geometry of the laser beam path [139]. Cantilever torsion stiffness is either calculated [135, 136, 139] or obtained experimentally by measuring the torsion angle resulting from a known turning moment [140]. Another two-step procedure , which is based on measuring friction force in the direction parallel to the long axis of the cantilever, has also been proposed, but unfortunately it cannot be considered a quantitative method [136]. Direct calibration of the lateral force can be obtained by applying a turning moment to the cantilever [141] or analyzing the contact response measured on a substrate with two well-defined slopes [142]. The later is identified as the wedge calibration method and is probably the most commonly accepted one.

The wedge lateral force calibration method involves sliding the cantilever probe over a surface slope of well-characterized geometry, where the mechanical response of the cantilever probe on the surface incline is understood in term of force balance equilibrium, proposed by Ogletree et al. [142]. The wedge calibration method was so far limited to integrated probes with sharp tips only and is performed on a complex specially prepared calibration grating. This technique is modified for colloidal probes by Varenberg et al. [143].

In this thesis, the lateral force calibration is performed by an improved wedge calibration method by Varenberg et al. [143] utilizing two defined sloped silicon surface (one is flat and one is 25° inclined from the flat one). All measurements are performed with AFM. A silicon surface with 25° slope angle is used for the lateral force calibration. The calibration is performed for multiple applied loads at least 5 times for each load. The pull-off force has been measured between each probe and the silicon flat portion, the detail procedures will be discussed in data analysis sub-chapter. This pull-off force is then used as an adhesion (F_{ad}) for all loads to executing the lateral force calibration.

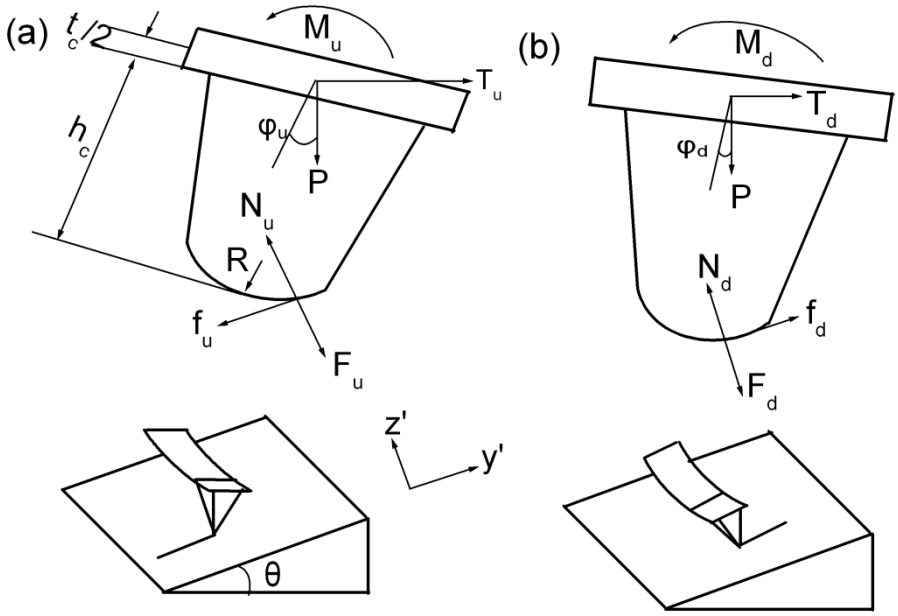

Figure 3.7: Schematic diagram of the cantilever tip while scanning (a) up and (b) down a sloped surface.

The free-body diagram in figure 3.7 depicts the forces and moments acting on the cantilever tip while scanning a sloped surface. The forces applied to the tip by the scanned surface, namely, the contact load N_c, the adhesion force F_{ad}, and the friction force F_{fr}, must be balanced by the applied load P, the force T, and the torsion moment M, which the cantilever exerts on the tip. When the tip slides across the surface, the acting forces are in equilibrium and depend on the direction of motion, thus for the uphill motion it is along the y' direction (see figure 3.7):

$$T_u \cos\theta - P \sin\theta - f_u = 0 \tag{3.4}$$

and along the z' direction

$$-T_u \sin\theta - P \cos\theta + N_u - F_u = 0. \tag{3.5}$$

Similarly, for the downhill motion

$$T_d \cos\theta - P \sin\theta + f_d = 0 \tag{3.6}$$

and

$$-T_d \sin\theta - P \cos\theta + N_d - F_d = 0. \tag{3.7}$$

Assuming $F_{fr} = \mu N_c$ where μ is a constant, and $F_u = F_d = F_{ad}$ in the range between N_u and N_d, equation (3.4) and (3.5) for the uphill motion will be

$$T_u = \frac{P\sin\theta + \mu(P\cos\theta + F_{ad})}{\cos\theta - \mu\sin\theta} \tag{3.8}$$

and from equation (3.6) and (3.7) for the downhill motion

$$T_d = \frac{P\sin\theta - \mu(P\cos\theta + F_{ad})}{\cos\theta + \mu\sin\theta} \tag{3.9}$$

The moment equilibrium equations about the point of the tip/surface contact, assuming small cantilever torsion angle φ ($\sin\varphi = \varphi$, $\cos\varphi = 1$), yield for the uphill motion

$$M_u + P\left[R\sin\theta - (h_c - R + \frac{t_c}{2})\varphi_u\right] - T_u\left(R\cos\theta + h_c - R + \frac{t_c}{2}\right) = 0 \tag{3.10}$$

and for the downhill motion

$$M_d + P\left[R\sin\theta - (h_c - R + \frac{t_c}{2})\varphi_d\right] - T_d\left(R\cos\theta + h_c - R + \frac{t_c}{2}\right) = 0 \tag{3.11}$$

In equation (3.10) and (3.11), R is the tip radius of curvature, h_c is the tip height, t_c is the cantilever thickness, and assuming that the force T acts through its mid section. The relation between the torsion moment, M, and the torsion angle, φ, is given by

$$\varphi = \frac{Ml}{GJ} \tag{3.12}$$

where l is the cantilever length, G is the shear modulus, and J is the torsion constant of the cross section (not to be confused with the polar moment of inertia). Combining equation (3.10) and (3.12) gives

$$M_u C + PR\sin\theta - T_u\left(R\cos\theta + h_c - R + \frac{t_c}{2}\right) = 0 \tag{3.13}$$

where $C = \frac{\frac{GJ}{l} - L\left(h - R + \frac{t}{2}\right)}{GJ/l}$. In general C is about 1 for silicon cantilever (G = 564 GPa, w = 30 μm, t_c = 1 μm, l = 100 μm, $J = 0.3wt^3$ for the rectangular cross section of $w/t_c > 10$ [144], h = 20 μm, R = 10 nm, and P = 5 μN) and equation (3.13) for the uphill motion becomes

$$M_u + PR\sin\theta - T_u\left(R\cos\theta + h_c - R + \frac{t_c}{2}\right) = 0 \tag{3.14}$$

Similarly, combining equation (3.11) and (3.12) gives for the downhill motion

$$M_d + PR\sin\theta - T_d\left(R\cos\theta + h_c - R + \frac{t_c}{2}\right) = 0. \tag{3.15}$$

The ultimate goal of this analysis is to define the relation between a lateral (friction) force on the probe tip while scanning a flat surface, f^{flat}, and the resulting moment M, which is actually measured by the AFM through the cantilever torsion angle, φ. The measured voltage output M_o (the ''o'' subscript indicates a moment measured in volts) is related to M by $\beta M_o = M$, where the calibration constant β (in newton-meters per volt) is a product of all the factors of the system. Hence, combining equation (3.4) and (3.14) for a flat surface, where θ = 0, will result into equation (3.16).

$$f^{flat} = T^{flat} = \frac{M^{flat}}{h_c + \frac{t_c}{2}} = \alpha M_0^{flat} \tag{3.16}$$

where the calibration constant α (in newtons per volt) is

$$\alpha = \frac{\beta}{h_c + t_c/2}. \tag{3.17}$$

The constant α converts a moment voltage output M_o to a friction force f^{flat}. Since for standard silicon AFM tip $h_c \gg R$ while in a spherical colloidal probe $h_c = 2R$, it is beneficial to treat the probes separately in order to find the calibration constant α. Substituting $h_c = 2R$ in equation (3.14) and (3.14) will result in to equation (3.18) and (3.19).

$$M_u = T_u\left[R(1+\cos\theta) + \frac{t_c}{2}\right] - PR\sin\theta \tag{3.18}$$

$$M_d = T_d\left[R(1+\cos\theta) + \frac{t_c}{2}\right] - PR\sin\theta \tag{3.19}$$

The equation (3.18) and (3.19) are for the uphill and downhill motion, respectively. The torsion loop, which is obtained on the sloped surface, is illustrated in figure 3.8.

$$W = \frac{M_u - M_d}{2} \tag{3.20}$$

$$\Delta = \frac{M_u + M_d}{2} \tag{3.21}$$

W is the half-width of the loop and Δ is the offset of the loop. The measured voltage output M_o where $\beta M_o = M$ defines $\beta W_o = W$ and $\beta \Delta_o = \Delta$. Experimentally, due to signal drift, crosstalk between deflection and torsion signals, and even small misalignment of the laser or cantilever with respect to the photodiode, it is impossible to identify the exact zero of the torsion signal (see figure 3.8) and, hence, the actual torsion loop offset, Δ_o. The torsion loop half-width, W_o, on the other hand, is insensitive to this problem since this is a relative value that involves a difference between torsion signals where, to first order, all absolute errors cancel out.

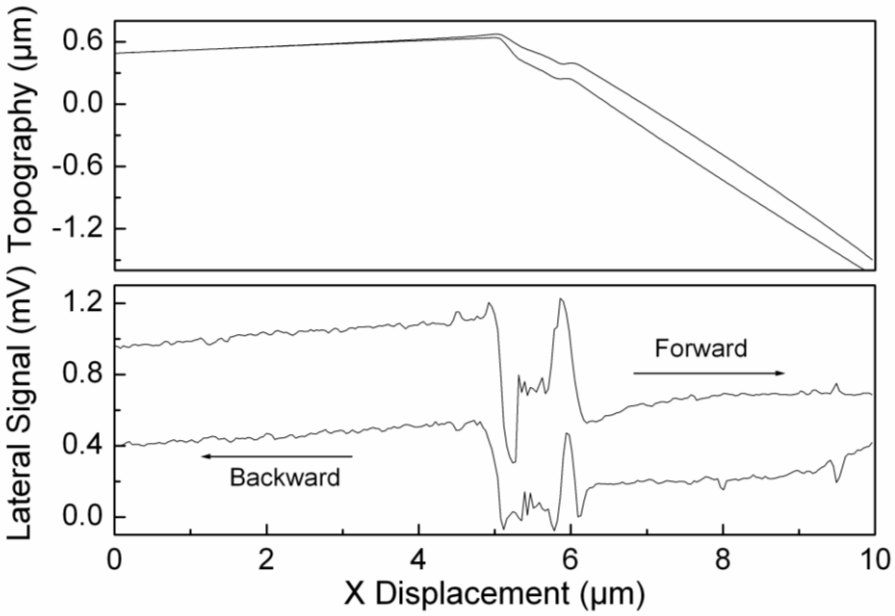

Figure 3.8: Topographical and torsion signal of sloped silicon surface for 2.5 μm colloidal probe at 500 nN load.

Now, substituting equation (3.8), (3.9), (3.18), and (3.19) in equation (3.20), recalling that W = βW_o,

$$\frac{\mu(P + F_{ad}\cos\theta)}{\cos^2\theta - \mu^2\sin^2\theta} = \frac{\beta W_o}{R(1+\cos\theta)+t_c/2} \tag{3.22}$$

Similarly, from equation (3.21), recalling that $\Delta = \beta(\Delta_0^* - \Delta_0^{flat})$

$$\frac{\mu^2\sin\theta(P\cos\theta+F_{ad})+P\sin\theta\cos\theta}{\cos^2\theta-\mu^2\sin^2\theta} - \frac{PR\sin\theta}{R(1+\cos\theta)+t_c/2} = \frac{\beta(\Delta_0^*-\Delta_0^{flat})}{R(1+\cos\theta)+t_c/2} \tag{3.23}$$

Dividing equation (3.23) by equation (3.22) results in a quadratic equation (3.24) for the unknown μ in the form

$$\mu^2\left[\sin\theta\,(P\cos\theta + F_{ad})\left\{R(1+\cos\theta)+\frac{t_c}{2}\right\}\right] - \mu\left[\left(\frac{\Delta_0^{*}-\Delta_0^{flat}}{W_o}\right)(P + F_{ad}\cos\theta)\{R(1+ \\ + PR\sin^3\theta \\ \cos\theta + tc/2 + P\sin\theta\cos\theta R1 + \cos\theta + tc2 - PR\sin\theta\cos2\theta = 0 \quad (3.24)$$

$$\mu^{flat} = \frac{\alpha W_o^{flat}}{(P+F_{ad})} \quad (3.25)$$

With known values of θ, P, and F_{ad} and measured values of torsion loop offset (Δ_o^{*} - Δ_o^{flat}) and the torsion loop half width (W_o), two possible solution of the friction coefficient (μ) can obtained. The real solution should be smaller than $1/t_c g\theta$. If both of the values of μ satisfy the condition $\mu < 1/t_c g\theta$, each of the two possible values of μ yields a corresponding α. Lateral force calibration factors (α) for 2.78 and 10.25 μm radii colloidal probes are calculated. The lateral force calibration factor is measured at different applied normal load and different values of calibration factor are obtained (table 3.4). When applied load is lower than the adhesion force between tip and silicon sample ($P < F_{ad}$), the lateral force calibration factor is found to be increased with applied load. It remains constant when applied load is higher than the adhesion force between tip and silicon sample ($P > F_{ad}$). In literature, no reason has been presented yet. There may be a possibility of that at applied load lower than adhesion force ($P < F_{ad}$), the torsion loop value may be overestimated and resulting into lower calibration factor. Therefore for obtaining lateral force signal in term of Newton, lateral force calibration factor has to multiply individually at each applied load.

Table 3.4: Lateral force calibration factor for colloidal probes.

Colloidal probe (2.78 μm)		**Colloidal probe (10.25 μm)**	
Load (nN)	**α (nN/V)**	**Load (nN)**	**α (nN/V)**
100	39 ± 9	500	185 ± 27
300	185 ± 8	1000	321 ± 6
500	234 ± 30	1500	311 ± 8
700	295 ± 17	2000	294 ± 7
900	261 ± 11	2500	292 ± 10

3.3.1.3 Normal and later force resolution

The applied load range is mainly dependent on the stiffness of AFM probe cantilever. 10.25 µm colloidal probe of 100 N/m spring constant AFM cantilever can provide the load limit up to 2.5 µN whereas 2.78 µm colloidal probe of 10.8 N/m spring constant AFM cantilever can provide the load limit up to 1 µN.

In order to find the normal resolution of AFM, the scratches with both probes are performed on smooth silica sample at given applied load ranges. For example the scratches with 10.25 µm colloidal probe on silica sample are performed at set applied loads of 100 nN to 2.5 µN. A deviation in set applied load is noticed and deviation (ΔP_{err}) between set applied load and actual load is referred as an error. ΔP_{err} is 69-86 nN at 2 Hz scan rate, while ΔP_{err} is 7-11 nN at 0.3 Hz scan rate. The % load error is calculated as

$$\text{load error (\%)} = \frac{\Delta P_{err}}{P} \times 100 \tag{3.26}$$

where ΔP_{err} is deviation between set applied load (P) and actual load. % load error is plotted against the applied load for different scan rate in figure 3.9.

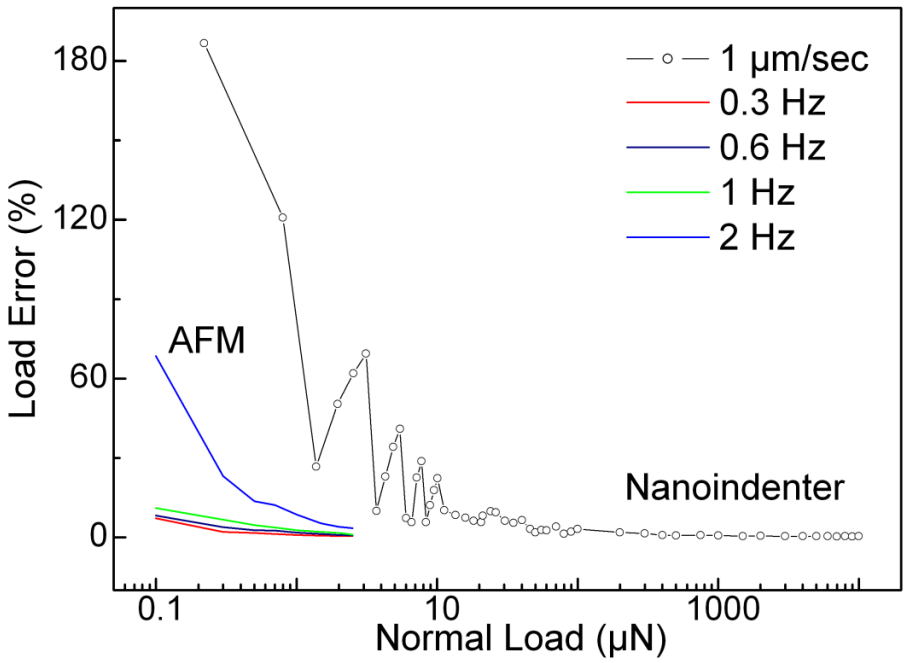

Figure 3.9: % load error vs. applied normal load for silica surface derived with 10.25 µm colloidal probe and 20 µm indenter.

ΔP_{err} is increased with applied load whereas % load error decreases with applied load. ΔP_{err} and % load error is increased with scan rate of tip. The slower the sample is scan and the better the feedback parameters are set, the smaller the error will be. ΔP_{err} or % load error is also expected to depend upon the focused laser spot size and position on the cantilever. The value of ΔP_{err} can be reduced by proper adjustment of laser spot on the cantilever. At a given applied load and scan rate, the size of the photodiode will be higher for soft cantilever and higher error will be. This is because of that the deflection of laser beam from soft cantilever will make larger laser beam diameter than the one from stiff cantilever. This kind of error can be minimized by proper selection of spring contact and corresponding set applied load range.

In order to find the normal resolution of AFM, the scratches with both probes are performed on smooth silica sample at given applied load ranges. For example five scratches with 10.25 μm colloidal probe at 0.3 Hz scan rate on silica sample are performed at set applied loads of 100 to 2500 nN. The resulting lateral force of 165 to 725 nN is obtained. The error in lateral force (ΔF_{fr}) is also observed. As mentioned earlier all scratch tests have done at 0.3 Hz scan rate with smooth silica surface, so the error in lateral force is lowest. ΔF_{fr} is found from 230 to 808 nN at applied load of 100 to 2500 nN. The % lateral force error is calculated as

$$\text{lateral force error (\%)} = \frac{\Delta F_{fr}}{P} \times 100\ \% \tag{3.27}$$

where ΔF_{fr} is deviation in lateral force at applied load (P). The % error is plotted against the applied load in figure 3.10. The % lateral force error decreases from 230 to 32 % at applied load from 100 to 2500 nN. ΔF_{fr} or % lateral force error depends on error in applied load, noise, surface roughness, and lateral force calibration factor. ΔF_{fr} is increased with applied load whereas % lateral force error decreases with applied load. ΔF_{fr} or % lateral force error is increased with scan rate of tip. The slower the sample is scan and the better the feedback parameters are set, the smaller the error will be. ΔF_{fr} or % lateral force error is also expected to depend upon the focused laser spot size and position on the cantilever. The value of ΔF_{fr} can be reduced by proper adjustment of laser spot on the cantilever. At a given applied load and scan rate, the size of the photodiode will be higher for soft cantilever and higher error will be. This is because of that the deflection of laser beam from soft cantilever will make larger laser beam diameter than the one from stiff cantilever. This kind of error can be minimized by proper selection of spring contact and corresponding set applied load range. In this thesis, the set applied loads of 100-900 nN and 500-2500 nN are used for 2.78 and 10.25 μm colloidal probe, respectively. The scan rate of 0.3 Hz is used in the scratch tests.

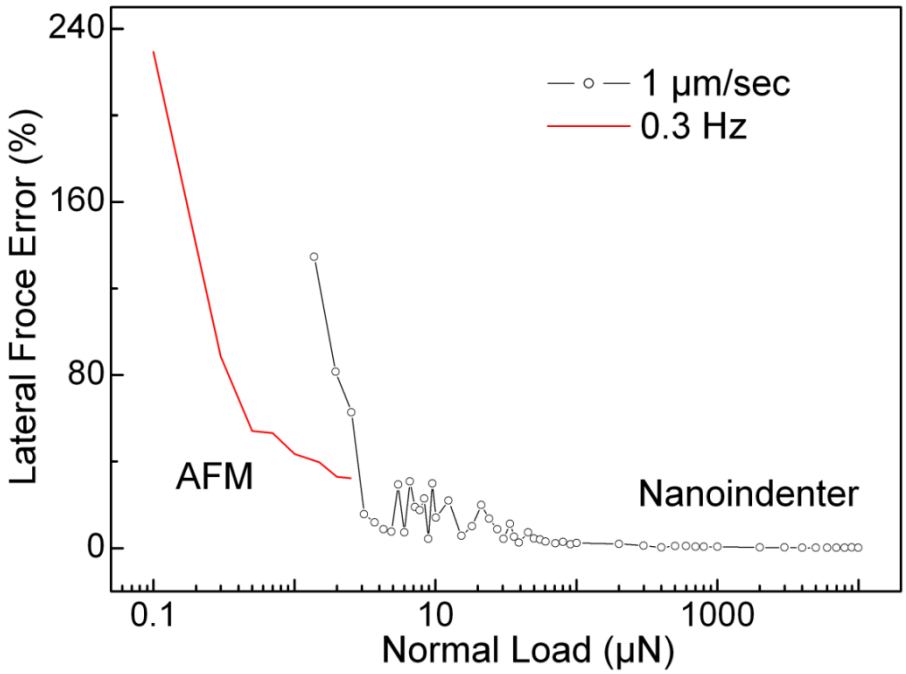

Figure 3.10: % lateral force error vs. applied normal load for silica surface derived with 10.25 μm colloidal probe and 20 μm indenter.

3.3.2 Nanoindenter

The mechanical and tribological characterizations are done by a combination of atomic force microscope and Nanoindentor. The atomic force microscopy provides a high lateral resolution, but the mechanical characterization using available cantilever system is extremely difficult. A regular and common Nanoindenter system provides the actual and indeed correct information for mechanical properties, but it is not possible to get the topographical information of at where the test was made. The Hysitron produced TriboIndenter (Nanoindenter) has the ability to produce the topographical information in addition to mechanical and tribological characterizations. By means of this system, it is now possible to locate the desired area of the surface for further mechanical characterization. By imaging before and after indentation or scratching, it could provide the important information about surface deformation mechanisms such as sink-in, pile-up, wear debris, fracture, and critical load for elastic to plastic deformation, etc.

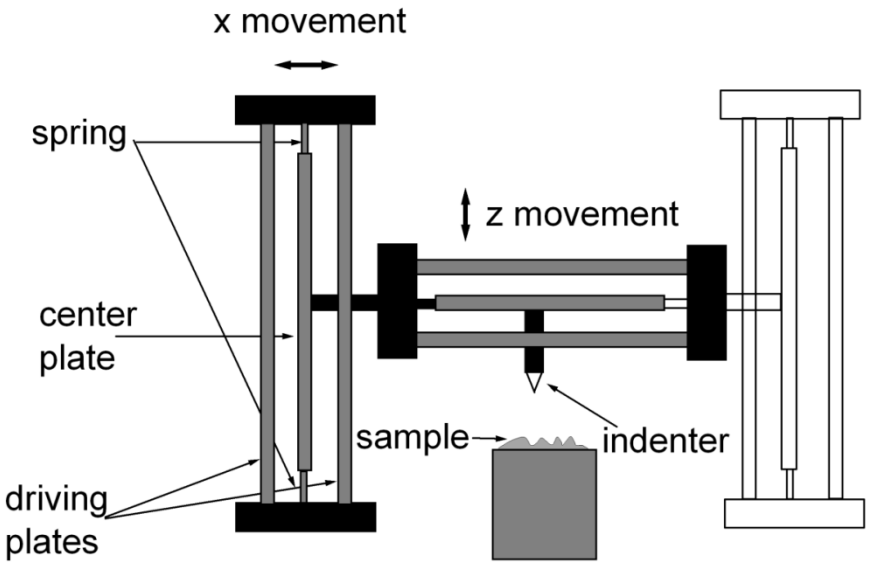

Figure 3.11: A schematic of a TriboIndenter setup.

TriboIndenter is a paired three-plate capacitive force-displacement transducer system, as shown in schematic figure 3.11. The indenter, generally made of diamond, is mechanically fixed in the middle of the z-plate. The force applied in the system can be calculated from the magnitude of the voltage applied. The system consists of two parallel and closely spaced fixed outer plates (driving plates), which are driven by AC signals. The maximum signal at the driving plates and minimum signal at central plate is applied. The input impedance of the synchronous demodulator is significantly larger than the output impendence of the transducer, so the pickup electrode will assume the same potential present at its position between the drive plates. This results in an output signal to the driving plate at maximum deflection, zero at the central position, and varying in a linear manner between maximum displacement and the center position. The system may also be used in either quasi-static or dynamic mode. Quasi-static mode calculates properties at the maximum penetration depth, delivering a single value for stiffness. In dynamic mode utilizes sinusoidal loading concurrent with the quasi-static measurement loading. In this thesis, the work has been done in quasi-static mode. When configured with two force transducers and a high load device, the system is capable of applying forces that range from hundreds of nN to 10 mN.

3.3.2.1 Calibration of Nanoindenter

In Nanoindenter, the centre plate is hold by a four-spring system and isolated by driver plates. The plate gap can change resulting into a change of electrostatic force constant. For

this reason, the electrostatic force constant must be calibrated using air indentation method after installing new indenter tip into the system. While using Nanoindentation test, the center plate of the transducer moves. This movement will cause a change in the electrostatic force constant. If the change in movement is less than 1 μm, the electrostatic force constant will not change much, and a single value of electrostatic force constant can be used for entire test. The TriboScan 8.2.0.14 software will automatically correct the electrostatic force constant at large displacements. For this correction, the software must know the plate spacing or the zero volt gap of the transducer plates, and this can be done by performing an indent in air. For calibrating electrostatic force constant (z-axis calibration), the indent in air with maximum applied load of 600 μN and for a total of 20 sec is performed. The TriboScan 8.2.0.14 software will automatically generate the correct electrostatic force constant and automatically update into the system.

Before scratching on a sample, the electrostatic force constant for lateral direction (x-axis calibration) must be calibrated in the air. Scratch in air will define the rest position of the tip and find the associated electrostatic force constant and plate spacing. The center plate of the transducer is moved by actuating one of the drive plates. Then the center plate will attract towards the drive plate. On moving the center plate towards the drive plate, the distance between the drive plate and center plate will reduce and causing an increase in the electrostatic force. The exact plate spacing can be found by calibration in air. For this, scratch in air with zero normal loads is performed. Once plate spacing is known, the TriboScan 8.2.0.14 software can make the required corrections to compensate for the changing force constant.

During the indentation process, total displacement of indenter is sum of the indentation depth in the specimen and the displacement associated with the measuring instrument, termed as the load-frame compliance. For elastically isotropic half-space contact, the compliance is inverse of the stiffness. To account for elastic displacement of the load-frame of the instrument, the machine compliance (C_m) must be added to the contact compliance (C_c), and then total compliance of the Nanoindenter system will be

$$C_{total} = C_m + C_c = C_m + \frac{\sqrt{\pi}}{2}\frac{\sqrt{H}}{E^*}\frac{1}{\sqrt{P_{max}}}. \quad (3.28)$$

For standard fused quartz sample, it is assumed that the hardness and reduced modulus is constant at large indentation depths with a standard Berkovich indenter. A graph of

1/measured stiffness vs. $1/\sqrt{P_{max}}$ for a series of indents performed in fused quartz will yield a straight line with a y-intercept of the machine compliance. The machine compliance is usually affected by many factors such as transducer, indenter tip, sample, and transducer mounting. Different transducers show different values of compliance. Stiffness of central plate, thickness of epoxy holding parts together can cause different amounts of compliance. The indenter tips can have different values of compliance depending on the amount of epoxy and length of the shank on the tip. There is also possibility of compliance by sample itself due to soft materials used in sample mounting. This issue is solved by gluing sample with stiff or epoxy materials. The machine compliance should check for each transducer-tip configuration. In this thesis work, the same transducer is used, so the machine compliance needs to be checked for each tip. This can be done in conjunction with calculating the tip area function.

3.3.2.2 Calibration of tip Area function

To determine the mechanical properties, the area function of indenter tip must be calibrated. The method is based on constant and independent of indentation depth Young's modulus. Fused quartz with 72 GPa Young's modulus is used as a standard sample for calibration purpose. An area function relating the projected contact area ($A(\delta_c)$) to contact depth (δ_c) is obtained. To determine the area function, a series of indent at various contact depths (normal loads) are performed on fused quartz. The unloading contact stiffness (S) is calculated as slope of initial portion of unloading curve (equation (3.29)).

$$S = \frac{dP}{d\delta} = \frac{2}{\sqrt{\pi}} E^* \sqrt{A(\delta_c)} \tag{3.29}$$

After rearranging above equation will result into

$$A(\delta_c) = \frac{\pi}{4}\left(\frac{S}{E^*}\right)^2. \tag{3.30}$$

The projected contact area ($A(\delta_c)$) is calculated using equation (3.30). A plot of the computed area as a function of contact depth is plotted and fitting procedure is employed to fit the ($A(\delta_c)$) versus (δ_c) to a sixth order polynomial of the form (equation (3.31)).

$$A(\delta_c) = C_0\delta_c^2 + C_1\delta_c + C_2\delta_c^{1/2} + C_3\delta_c^{1/4} + C_4\delta_c^{1/8} + C_5\delta_c^{1/16} \tag{3.31}$$

C_0 is 24.5 and 2.598 for a Berkovich and cube corner tip, respectively. At the end, the above constant can be entered into the area function section of the TriboScan software.

3.3.2.3 Normal and later force resolution

The set applied load range using Nanoindenter is 0.2 μN to 10 mN. In order to access the normal load resolution of Nanoindenter, several scratch tests on smooth surface with both diamond indenters are carried out. For an example, a scratch of increasing set load from 0.2 μN to 10 mN is performed on smooth silica sample with 20 μm indenter. This scratch is performed at 1 μm/sec scratching speed and in open loop mode. The actual load is found to be different than the applied one. The deviation (ΔP_{err}) between set applied load and actual load is referred as error. ΔP_{err} is obtained from 0.38 μN to 38 μN corresponding to set applied load of 0.2 μN to 10 mN. The % load error is also calculated from equation (3.26). The % error is plotted against the applied load in figure 3.9. The % error exponential decreases from 186 to 10 % at set applied load of 0.2 μN to 10 μN and it decreases on further increasing applied load. ΔP_{err} and % load error are expected to depend on control mode (load and displacement control) and surface roughness. The load control mode, where set applied load is kept constant by feedback system, may produce results of less error. The scratching speed also affects the value of ΔP_{err}. The slower the sample is scratch and the better the feedback parameters (control mode) are set, the smaller the error will be.

In order to access the lateral force resolution of of Nanoindenter, several scratch tests on smooth surface with both diamond indenters are carried out. For an example, five scratches of increasing set load from 0.2 μN to 10 mN are performed on silica sample in open loop mode at 1 μm/sec. The lateral force (F_{fr}) is obtained from about 6.5 μN at applied load of 0.2 μN to 30 μN and on further increasing applied load the lateral force increases from 6.5 μN to 1215 μN. The error in lateral force (ΔF_{fr}) from those scratches is obtained from 2 μN to 22 μN at set applied load of 0.2 μN to 10 mN. The % lateral force error is calculated from equation (3.27). The % error is plotted against the applied load in figure 3.10. The % error exponential decreases from 135 to 10 % at applied load from 0.2 μN to 10 μN and it decreases on further increasing applied load. The lateral force of 6.5 ± 2 μN at low level of applied load includes the nominal lateral force resolution of about 3 μN, adhesion force of 3 ± 2 μN, and artifacts. These artifacts are generated by noise level of instrument and surrounding as well as surface roughness. The error in set applied load and lateral force is found very high in applied load up to 10 μN. So open loop mode and set applied load from 10 μN to 10 mN are used in this thesis

3.4 Data analysis

Preceding the calibration of AFM and Nanoindenter, the experiments for surface roughness characterization, mechanical characterization, adhesion force measurements, and tribological characterization are carried out. In this sub-chapter, first experimental detail of measuring surface roughness of analyzed samples and probes is discussed, followed by experimental detail for mechanical characterization of analyzed samples and adhesion force between probes and analyzed samples. Finally the experimental details for AFM and Nanoindenter based tribological testing are discussed.

3.4.1 Roughness

The surface morphology is characterized by atomic force microscopy (AFM) (XE-100, PSIA). Non-contact AFM is mainly used to obtain detailed information about surface topography and surface roughness. The samples are imaged with commercial tips featuring a nominal tip radius of 10 nm in a feedback controlled mode on all three x-, y- and z-axes. Five 8X8 μm^2 with a pixel resolution of 512X512 are taken at different surface position of each sample in order to drive the corresponding RMS roughness. The appropriate topography of the conical diamond indenters and silica colloidal probes are also characterized.

3.4.2 Mechanical characterization

The mechanical characterizations are carried out by a transducer-based scanning Nanoindenter (TriboIndenter, Hysitron Inc.) in a laboratory environment (RT and 40%RH). The mechanical properties of the samples are evaluated with a Berkovich diamond tip of about 100 nm radius following the procedure proposed by Oliver and Pharr method [7, 91]. The samples are probed at three different spots. At each spot, 100 indents are placed in a grid pattern (10 times 10 indents with 20 μm spacing) varying in final load from 10 mN to 100 μN (100 μN/s loading and unloading rate, 5 seconds hold time at maximum load). At the end, the force-displacement curves are obtained with three segments named as loading, holding, and unloading. After analyzing the unloading segment for 5 to 60 % from the top of the segment using Oliver and Pharr method, the hardness and elastic modulus are directly obtained.

3.4.3 Surface adhesion

The pull-off force measurements are performed using an AFM under varying loads from 100 nN to 1 μN in a laboratory environment (RT and 40%RH). For adhesion force measurements, several pull-off force curves are captured on different parts of the analyzed sample surfaces. Velocity of tip-approach to the sample surface and maximum applied load are kept constant for each measurement. It is difficult to maintain the same maximum load (during capture of force calibration curves) for all size of tips due to the different spring constants and deflection sensitivities (due to different adjustment of cantilever in the cantilever holder).

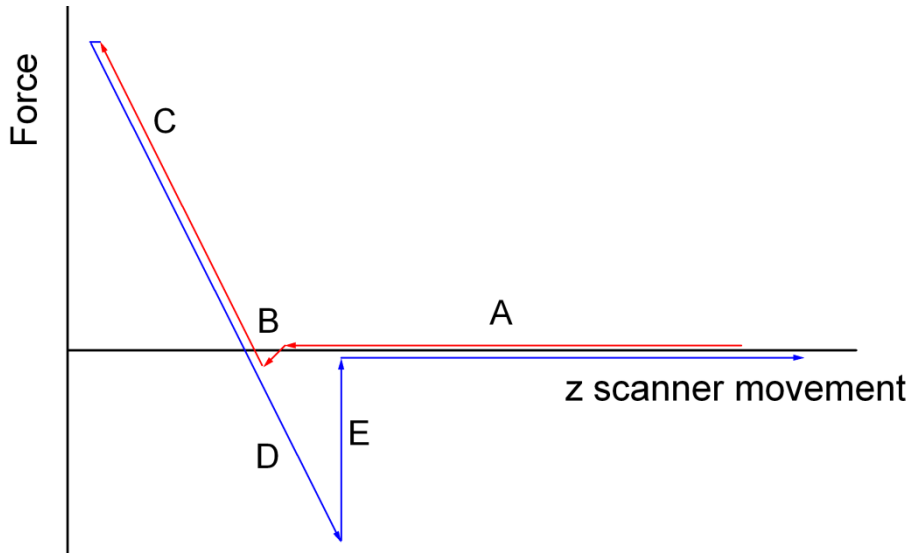

Figure 3.12: The graph shows the force measured by AFM-cantilever versus tip sample distance.

For adhesion force measurements, several pull-off force curves are captured on different parts of the analyzed sample surfaces. A typical force-distance curve for pull-off force measurement is as shown in figure 3.12. The adhesion force is measured through z scanner movement. The z scanner declines and inclines, so the tip will pull down on one point of the sample (red line) and pull off (blue line). Tip movement towards the sample is described in 5 steps. (A) Approach: tip is approaching to the sample. In this step, tip does not make any contact with sample. (B) Jump to contact (Snap-In): Tip is pulled down by attractive force near the surface. (C) Contact: Tip is pushing down the sample, so tip is bent. Lowering z scanner will bent tip even more. (D) Adhesion: When pulling up z scanner, due to interaction between tip and sample, adhesion force occurs. This force occurs until critical point. Due to

this, tip bent down. (E) Pull-Off: Distance between tip and sample is so far that it reaches critical point, so there are no contact between sample and tip. The adhesion force (pull-off force) is y-axis minimum value of retrace data and it can be is calculated using Hook's law i.e. by multiplying spring constant (k) of the cantilever by cantilever deflection at the jump out point. By using XEI 100 software, the adhesion force is directly obtained.

3.4.4 Tribological testing

3.4.4.1 AFM based scratch tests

Preceding the pull-off force measurements, the tribological tests are carried out with 10.25 and 2.78 µm colloidal probes. In order to access the friction signal, the samples are scanned in contact mode and lateral force images (forward and backward) are recorded and subtracted afterward. Three 20X20 and 10X10 μm^2 with a pixel resolution of 256X256 are taken at different surface position for 10.25 and 2.78 µm colloidal probes, respectively. The whole image is divided into multiple segments in the long axis where the normal load is progressively increased (see figure 3.13). From the subtraction of each pair of segments (backward and forward), yielding the lateral force in volt as shown in figure 3.14 which are converted into unit of Newton by using lateral calibration factor. The scratch tests with different constant normal load have been performed. For all scratch tests in this thesis the scan rate is set to 0.3 Hz in order to reduce the error in applied load. The applied loads are varied from 100 to 700 nN and 100 to 2500 nN using 2.78 and 10.25 µm colloidal probe for each sample, respectively.

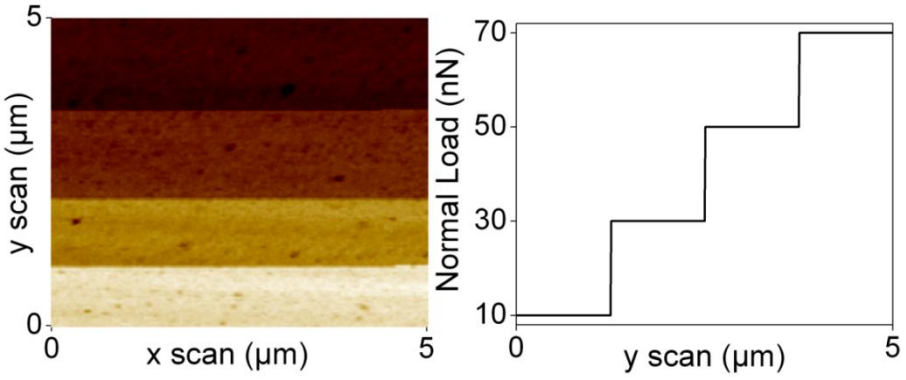

Figure 3.13: (a) Scheme of normal load change for average friction measurement. (b) Increase of the normal load during the measurement.

Friction force is measured under different loads ranged from 100 nN to 2.5 µN using a 90° scan depending on the size of probe. The figure 3.14 shows the simultaneous topography and torsion signal (trace), which are recorded with a silicon nitride standard AFM tip at applied load of 50 nN. The similar plots are obtained with the colloidal probes at the other applied loads as well as for retrace signal.

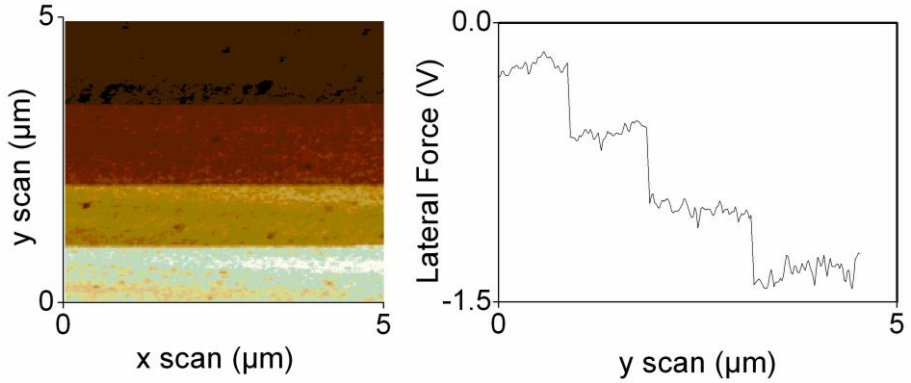

Figure 3.14: (a) Contrast of different lateral force output and (b) corresponding the lateral force signal in volt.

The friction voltage signal (half of the difference between trace and retrace scans) is converted to units of force using a lateral force calibration factor based on the improved wedge calibration method. This conversion factor (α) is used to convert the friction voltage signal to force units. Different values of conversion factor (α) are obtained for different type of cantilevers. The friction coefficients of analyzed samples are calculated as the ratio of friction force to the applied normal load.

3.4.4.2 Nanoindentation based scratch tests

One can design any scratch setup with Nanoindenter. Typically scratch setup consists of 5 segments: (1) Lateral movement of indenter tip from original position to negative direction with zero loads in 2.5 sec. (2) Indenter starts loading on the sample surface with defined loading rate such that end of it, the load is reached to the required values. In a separate experiment, the loading time is varied from 1 to 50 sec. It is found that the scratch results for silica sample are independent of loading time. The friction coefficient of aluminum sample initially decreases with increasing the loading time up to 10 sec, but the decay is very slow. On further increasing the loading rate, the friction coefficient merely changes. The decreasing friction coefficient for aluminum sample is due to increasing initial scratch depth.

(3) Now the scratching starts from negative to positive direction either with increasing/decreasing or with constant normal load. (4) Indenter then starts to unload with defined unloading rate such that end of it, the normal load will be zero, this step is also not very much important in characterization of tribological properties. (5) Finally, indenter returns to its initial position with zero applied load in 2.5 sec. In general first and last step are not affecting the tribological properties. Third step is actual step for tribological study.

Tribological testing has been done with constant load scratching and ramping load scratching. In constant load scratch tests, applied normal load is constant throughout scratching. In ramping load scratch tests, the applied load either increases or decreases linearly. In following sub-chapter, the experimental details of constant as well as ramping load scratch tests are presented.

3.4.4.2.1 Scratch test measurements for constant normal load

One load and lateral displacement scheme of a scratch segment for constant load scratch test is shown in figure 3.15.

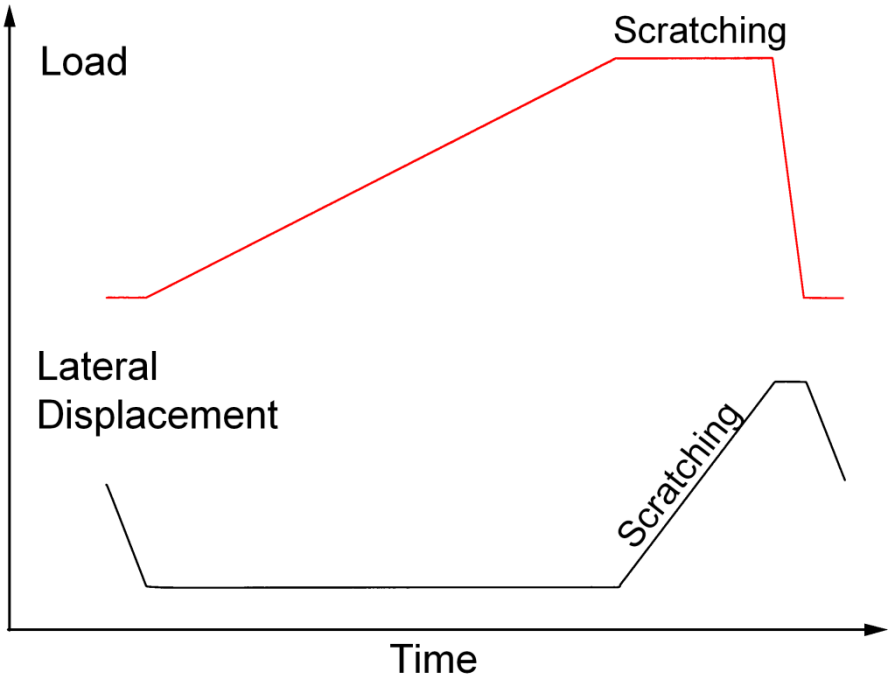

Figure 3.15: Example for a load and displacement scheme of one of the individual scratch segments used in this work.

As mentioned earlier the minimum applied load is 10 μN. The applied normal loads using 1 μm indenter are varied from 10 to 1800 μN, 10 to 1500 μN, 10 to 600 μN and 10 to 130 μN for silica, smooth DLC, rough DLC, and aluminum sample, respectively. The applied normal load using 20 μm indenter are varied from 10 to 4500 μN, 10 to 1600 μN, 10 to 800 μN, and 10 to 800 μN for silica, smooth DLC, rough DLC, and aluminum, respectively. In the case states here the interval or gap between two applied normal loads is ranged from 250 μN to 10 μN depending on sample roughness and indenter radius. Here the 250 μN corresponds to a scratch test of the smooth silica sample have been carried out with the 20 μm conical indenter and the 10 μN segment size to a test of the aluminum sample utilizing the 1 μm conical indenter. For all scratch tests, the minimum distance between two scratches and scratch distance are set to 20 μm and 10 μm, respectively. The scratching speed is varied from 0.33 to 3.33 μm/sec.

Table 3.5: Range for applied normal load for various rough surfaces and 1 and 20 μm diamond indenters.

Sample	Applied load for 1 μm diamond indenter (μN)	Applied load for 20 μm diamond indenter (μN)
Fused Silica	10 to 1800	10 to 4500
Smooth DLC	10 to 1500	10 to 1600
Rough DLC	10 to 600	10 to 800
Aluminum	10 to 130	10 to 800

Apart from the above mentioned scratch tests for fused silica, DLCs, and aluminum samples, the scratch tests are also performed on SiBCN composite coatings. For SiCBN coatings, the scratch tests are performed at constant applied normal load ranged from 10 to 500 μN derived with 20 μm indenters. The scratch speed, minimum distance between two scratches, and scratch distance are set to 1 μm/sec, 20 μm, and 10 μm respectively for all scratch tests for SiCBN coating.

The friction coefficient is measured as the ratio of the tangential force to the normal load. The typical curve of this measured friction coefficient is composed of three parts: the first part is correlated with the loading stage, the second part is the steady state scratching, and the last part is generated due to the detachment of the indenter during unloading. The measured friction coefficient of samples under different constant loads is as shown in figure 3.16. The effective values are obtained by calculating the average values of the second part.

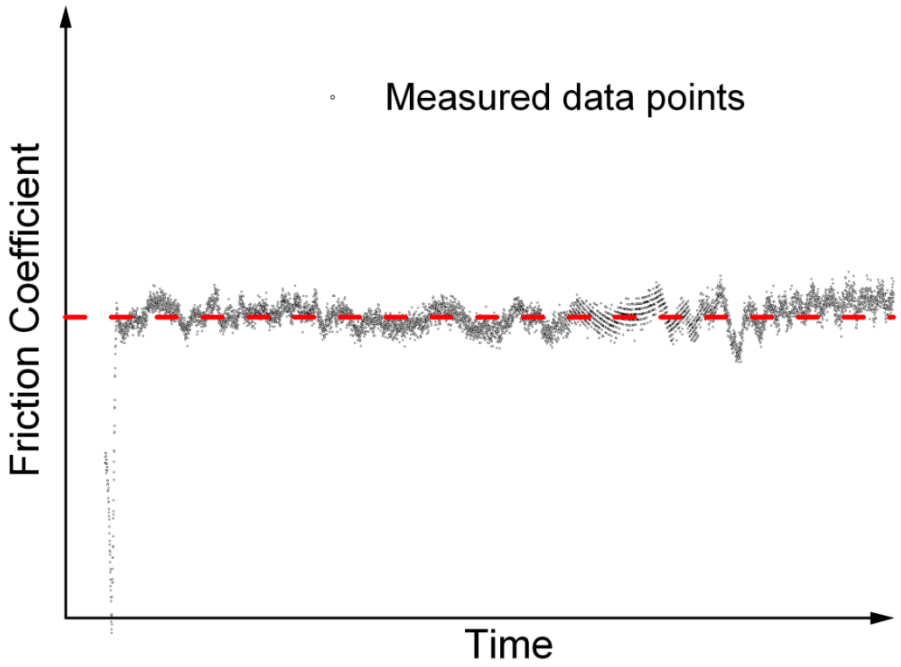

Figure 3.16: Variation of the measured friction coefficient during the scratch process.

3.4.4.2.2 Scratch test measurements for ramping normal load

As preliminary testing confirmed that the test results are not influenced by fashion of load ramping, i.e. increasing or decreasing load during scratching, and the scratch test with ramping load is done only with linear increasing load. One load and lateral displacement scheme of a scratch segment for ramping normal load are shown in figure 3.17. The scratch length, minimum distance between two scratches, and number of scratches for a particular load are set to 10 (-5 to 5) µm, 20 µm, and 10 µm, respectively for all scratch tests.

The total normal load range of each scratch is divided into segments in order to identify the suitable normal load range i.e. the range that do not feature any artifacts which might be dominated by instrumental boundary conditions. For practical reasons these segments has to be small but at the same time has to contain an adequate number of data points to be analyzed. In present case, the segment size is ranged from 300 µN to 20 µN depending on sample roughness and indenter radius. Here, 300µN segment size corresponds to a scratch test of the smooth fused quartz sample have been carried out with the 20 µm indenter and the 20 µN segment size corresponds to a test of the rough DLC sample utilizing the 1 µm indenter. The suitable load range is then defined as the range from the minimum normal load of 10 µN up to either the maximum normal load of the instrument, i.e. 10 mN, or the first segment that features a maximum lateral load difference larger than its segment size (table 3.6). The latter

case usually can be attributed to some stick-slip event that will contain a strong influence of the properties of the transducers spring setup. Therefore such segments are not considered in this thesis.

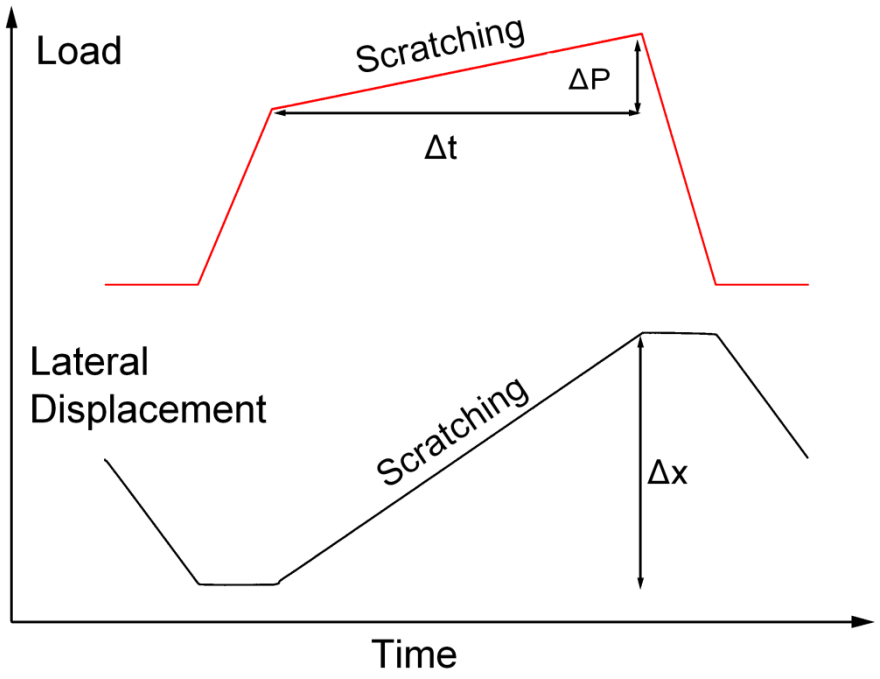

Figure 3.17: An illustrated figure for scratch test. Load and indenter position crosspond to the scratch time.

Table 3.6: Segment size of linear increasing load and range for applied normal load for various rough surfaces and 1 and 20 µm diamond indenters.

Sample	**1 µm diamond indenter**		**20 µm diamond indenter**	
	Segment size (ΔP)	**Range of applied normal load (µN)**	**Segment size (ΔP)**	**Range of applied normal load (µN)**
Fused Silica	100	10-1000	300	10-6000
Smooth DLC	20	10-210	50	10-750
Rough DLC	20	10-110	20	10-170

Beside the above mentioned scratch tests for fused silica and DLCs samples, ramping scratch tests are also performed for SiBCN composite coatings. For SiCBN coatings, the scratch tests are performed with ramping load of 10-100 and 10-300 µN using 20 µm indenters. The

scratch speed, minimum distance between two scratches, and scratch distance are set to 1 μm/sec, 20 μm, and 10 μm respectively for all scratch tests for SiCBN coating.

In order to understand the loading rate effect on friction, the tribological scratch tests have been performed with different ramping normal load on the silica sample using both indenters. In general, the loading rate (dP/dt or ΔP/Δt) is defined as ratio of the size of ramping load scratch segment (ΔP) to scratching time (Δt) and therefore, loading rate can be changed either by changing the segmental size of increasing normal load or time interval. In present case, the ΔP is changed while Δt is fixed. Although these scratch tests are performed using different ΔP, but the center of ΔP, scratch length, and scratch duration are fixed i.e. the experiments involves a constant tip lateral displacement speed (dx/dt) and different values of the loading rate (dP/dt). These scratch tests are done at applied load range from 50 μN to 5000 μN depending on the size of indenter.

In case of ramping load scratching, scratching speed or lateral displacement rate of tip (dx/dt or Δx/Δt) may be defined as ratio of lateral displacement (Δx) of tip during scratching and time duration of scratch (Δt), therefore the scratching speed can be changed either by changing the lateral displacement of tip (Δx) or time interval (Δt). It is only possible by changing the scratch length without changing the loading rate. A set of scratch tests are done on silica sample using different scratch lengths (Δx = 10, 8, 6, 4, and 2 μm) with constant dP/dt for load range from 50 to 5000 μN.

The slope of a linear trend line fit for each scratch is taken as the scratch friction coefficient at a normal load equal to the centre of the load for scratching with linear increasing normal load. This procedure ensures the elimination of any non-zero measured friction force that might be present at a normal load of zero, see figure 3.18. The later is usually explained by an additional load terms due to an intrinsic adhesive force and/or artifacts generated by the equipment. The adhesion force term itself consists of various attractive forces such as capillary, electrostatic, Van der Waals, and others.

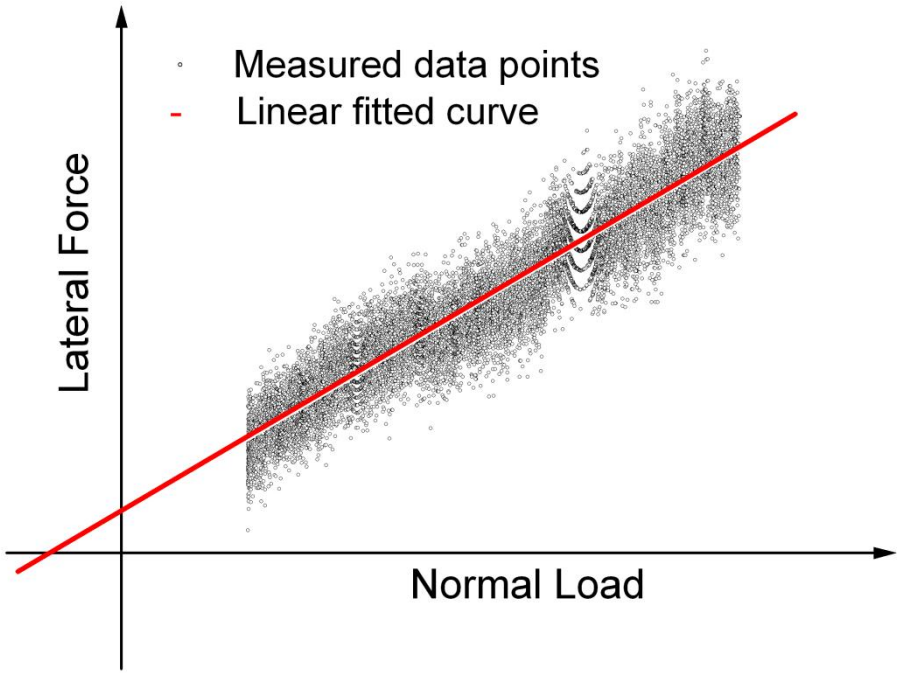

Figure 3.18: Lateral force vs. normal load plot for the silica sample in contact with the 1 µm conical indenter and the friction coefficient is estimated by a linear fitting routine.

Chapter 4 Results and Discussion

In this chapter, first surface roughness of analyzed samples and probes are presented. Next the mechanical properties of analyzed sample are presented. Followed by the adhesion force results are discussed. Finally tribological results and effect of surface roughness, mechanical characterization, adhesion force, and external parameters (applied load, loading rate, and scratching speed) on friction are discussed.

4.1 Surface topography and surface roughness

As mentioned in chapter 3, the homogeneous, amorphous, isotropic fused silica, diamond-like-carbon (DLC) and Si-C-B-N-O samples are selected. The thickness of DLC and Si-C-B-N-O coated films measured using SEM is found to be in order of few micrometers. All the coated specimens are chosen to understand adhesion and tribological phenomena. Amorphous silica micro-particles and self-assembled monolayers (SAMs) are chosen to measure the adhesion forces of particle to particle and of particle to flat surfaces and thus for study of effect of adhesion on tribological phenomena. Additionally, the smooth and polished non-amorphous silicon and aluminum samples are used for study the tribological phenomena. As mentioned earlier, the surface roughness is a key component in determining the nature of friction; therefore, the surface roughnesses of the analyzed samples as well as surface of probes are measured, and they are defined in term of root-mean-square (rms) in this thesis. AFM is employed to access rms value for each sample. The detail of experiments already described in chapter 3. In this sub-chapter, the surface roughness of analyzed samples and probes are presented along with their surface topography.

4.1.1 Silicon, Fused Silica, and Aluminum Samples

The rms values of silicon, fused silica, and aluminum samples are measured using AFM, and it is observed that the rms values of these samples are about 1 nm without any bumps and grooves. The rms values of silicon, fused silica, and aluminum samples are tabulated in table 4.1. After analyzing the topography, it is now known that the roughness of these surfaces is featured as closed-packed hemispherical asperity caps and troughs. The peak to peak distance (λ_2) of about 112 nm is found for silicon surface, which will be later used to compare experimental adhesion force and theoretical adhesion force.

Table 4.1: Roughness of fused silica, silicon, and aluminum.

Sample	Roughness, rms (nm)
Fused Silica	0.6 ± 0.1
Aluminum	1.5 ± 0.2
Silicon	0.2 ± 0.1

4.1.2 DLC Films

AFM and SEM images of DLC coatings are shown in figure 4.1. The DLC samples are prepared at a bias voltage of -950, -350, and -200 V. For different negative bias voltage, the DLC samples show different surface features (cauliflower like shape) and their roughness are increased with decreasing the voltage, and thus the different DLC rough surfaces are provided for further analysis. The surface features change with changing the bias voltage. The rms values of DLC samples are tabulated in table 4.2. The sample produced at -900 V is smoothest as shown in figure 4.1 (c, f) and rms roughness is about 4 nm. The roughness increases when the negative bias voltage decreases. The DLC samples, prepared at a bias voltage of -350 and -200 V, are having rms of about 12 and 24 nm, respectively. Later the terminology as smooth DLC (4 nm-DLC), rough DLC (12 nm-DLC), and very rough DLC (24 nm-DLC) will be used, respectively, see in table 4.2.

Table 4.2: Roughness of DLC samples at different bias voltages.

Negative Bias Voltage (V)	Sample	Roughness, rms (nm)
950	DLC-smooth	4.1 ± 0.1
350	DLC-rough	11.7 ± 0.7
200	DLC-very rough	23.9 ± 0.3

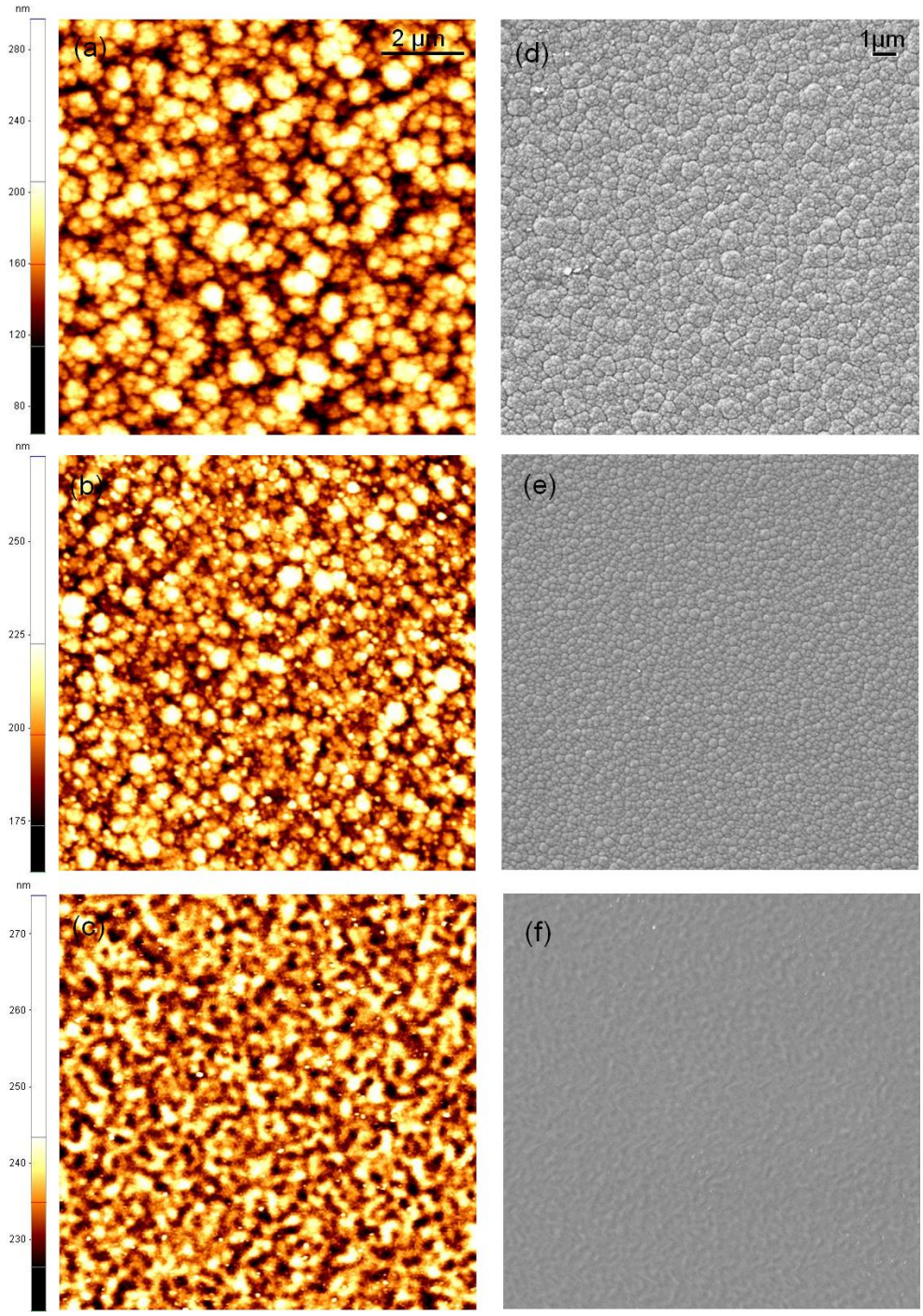

Figure 4.1: (a-c) AFM and (d-f) SEM images of DLC films.

After analyzing the topography, it is shown that the DLC surfaces feature closed-packed hemispherical asperity caps and troughs; see in figure 4.2. The 12 nm-DLC and 24 nm-DLC surfaces are exhibited two types of roughness profiles. The first roughness (rms_1) is associated with the larger peak-to-peak distance (λ_1). The both rough DLC samples (12 nm and 24 nm rms) reveal primary asperities of λ_1 = 600-2000 nm and their secondary asperities of about 225 nm λ_2 are superimposed on primary asperities. The radii of asperities are calculated by r =

$\lambda^2/58rms$ (table 4.3). The radius of primary asperities increases from 0.5 µm to 2 µm with increasing the roughness of DLC. The characteristic parameters (rms_1, rms_2, r_1, r_2, λ_1, and λ_2) are tabulated in table 4.3.

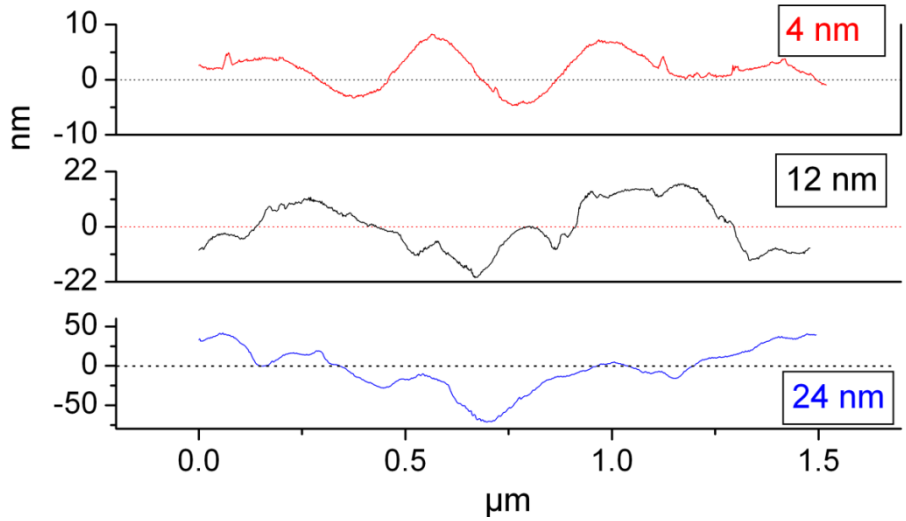

Figure 4.2: Surface roughness profiles of DLC samples as determined by AFM. Characteristic parameters are summarized in table 4.3.

Table 4.3: Measured roughness parameters, rms and λ, for the model surface and values of radii of peaks r_1 and r_2.

Sample	rms_1	rms_2	λ_1	λ_2	r_1	r_2
4 nm-DLC	0	4.1±0.1	0	388±66	∞	447-888
12 nm-DLC	10.9±0.7	4.1±0.1	833±248	229±25	536-1832	210-278
24 nm-DLC	23.6±0.3	4.1±0.1	1279±419	227±92	541-2111	78-433

4.1.3 Si-B-C-N-O coatings

X-ray diffraction (XRD) confirmed the amorphous structure of the Si-B-C-N-O coatings [145]. AFM measurements reveal that the Si-B-C-N-O coatings are very smooth. Films deposited on mirror-polished silicon single crystal substrates reveal rms values below 1 nm (table 4.4). SEM analysis reveals a glass-like fracture of the Si-B-C-N-O coatings exhibiting a dense and featureless structure.

Table 4.4: Roughness of Si-B-C-N-O coatings.

Samples	Roughness, rms (nm)
$Si_{19}B_{21}C_{23}N_{25}$	0.2 ± 0.1
$Si_{33}B_8C_{19}N_{27}$	0.9 ± 0.1
$Si_{36}C_{22}N_{25}$	0.5 ± 0.1
$Si_{40}C_{16}N_{27}$	0.8 ± 0.1

4.1.4 Self-assembled monolayers (SAMs)

The homogeneous SAMs of silica mirco particles of about 2.5 and 10 µm radii are characterized using SEM and AFM. The rms values of these particles are also measured using AFM. The rms values of 2.5 and 10 µm particles are about 2-3 nm. Figure 4.3 (a) and 4.3 (b) depict the SEM and AFM image of SAM of 2.5 µm particles, respectively. The AFM image shows the height variation of individual particle, which is based on the particle size distribution.

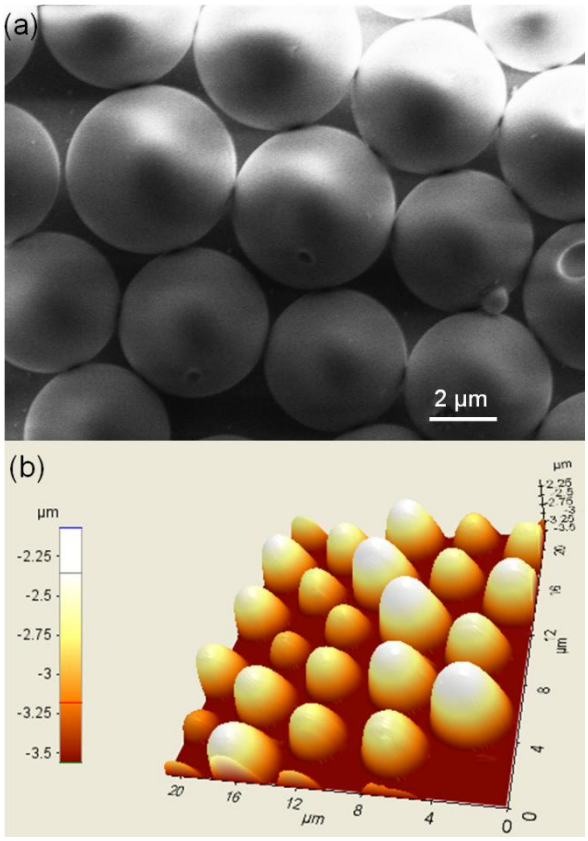

Figure 4.3: (a) A SEM image and (b) an AFM image of SAMs of 2.5 µm radius silica particles on a glass slide. AFM images are taken with commercial silicon nitride AFM tip.

4.1.5 Probes

The appropriate topography of the conical diamond indenters are characterized with an AFM. The resulting roughness of the 1 μm conical indenter is found to be negligible. The 20 μm conical indenter features topography aside from the overall macroscopic conical shape (with spherical end cap). However, its characteristic length scale is significantly larger than that of the samples studied here. For these reasons, the roughness of indenter is not considered. The colloidal AFM probes are prepared with spherical silica particles, and their average rms values are about 2-3 nm.

4.2 Mechanical Properties

The mechanical properties of materials is key component in determining the nature of friction as the mechanical properties influence the real contact area, the onset of plastic deformation, and shearing force. Therefore, mechanical properties of analyzed surface, mainly hardness (H) and elastic modulus (E), are measured. These quantities are determined by Nanoindentation technique. This technique generates load-displacement curve using standard diamond Berkovich indenter. The Oliver-Pharr method [146] is used to analyze the unloading segment of the load-displacement curves resulting in reduced elastic modulus and hardness values. In this sub-chapter, the hardness and the elastic modulus of fused silica, aluminum, DLCs, and Si-B-C-N-O films are presented.

4.2.1 Fused silica, Aluminum, and DLC film

A summary of the mechanical properties of these films are given in table 4.5. Several studies have shown that the DLC films, prepared at different bias voltage, have different hardness values [147, 148]. According to previous studies, it is shown that in the range of applying bias voltage, the hardness value decreases with increasing negative bias voltage, and same observation is experimentally found with DLC samples. The hardness and the reduced Young's modulus of smooth DLC sample are lower than those of the rough DLC sample. The fused silica sample depicts the typical hardness and reduced Young's modulus values as shown in table 4.5.The aluminum sample depicts the typical reduced young modulus values as shown in table 4.5. Although calculation of hardness of aluminum sample from indentation experiments by the method of Oliver and Pharr is resulted in unsatisfactory values and these values can be improved by the work Joslin and Oliver [149], and Saha and Nix [150] (based

on the numerical analysis by King [9]), but the measured value of hardness of 0.47 GPa is very close to existing literature value (0.45 GPa). Therefore, 0.47 GPa of hardness value is taken further for calculations.

Table 4.5: Mechanical properties of the fused silica, aluminum, and DLC samples.

Sample	Hardness (GPa)	Reduced Young's Modulus (GPa)
Smooth DLC	21±3	169±12
Rough DLC	23±6	187±26
Fused Silica	9±1	70±1
Aluminum	0.47 ± 0.1	75 ± 6

4.2.2 Si-B-C-N-O coatings

A summary of the mechanical properties of Si-B-C-N-O coatings is given in table 4.6. Upon analyzing the mechanical data, some distinct differences in the films are revealed. SiCN films have reduced Young's modulus values in the range of 160-169 GPa while hardness of around 24.2 ± 0.6 GPa which show no particular trend with changing the C-content. In contrast, SiBCN films exhibit lower reduced Young's moduli and hardness values. Both hardness and reduced Young's modulus of the lower boron containing $Si_{33}B_8C_{19}N_{27}$ are 23.6 ± 0.9 and 158 ± 4 GPa, respectively, which are close to those of SiCN films. However, increasing the coating's B-content is linked with a decrease in hardness and reduced Young's modulus reaching a minimum of 18.4 ± 0.6 and 127 ±2 GPa, respectively. This is correlated with the increase in softening B-N bonds.

Table 4.6: Mechanical properties of Si-B-C-N-O coatings.

Sample	Hardness (GPa)	Reduced Young's Modulus (E*) (GPa)
$Si_{19}B_{21}C_{23}N_{25}$	18 ± 1	127 ± 2
$Si_{33}B_8C_{19}N_{27}$	24 ± 1	158 ± 4
$Si_{36}C_{22}N_{25}$	24 ± 1	169 ± 3
$Si_{40}C_{16}N_{27}$	23 ± 1	160 ± 4

4.3 Adhesion Force

The adhesion forces is a key component in determining the nature of friction as it determines the actual contact area between two contacting bodies at given applied load and operating conditions. The adhesion studies are required to fully understand their origins and to enable control and optimization for successful tribological understanding. In this sub-chapter, the results from the interaction between adhering particles and interaction between different size of adhering particles (colloidal probes) and various rough surfaces such as silicon, fused silica, DLC, and aluminum are discussed. On analyzing the pull-off force test data, some distinct behaviour of adhesion force is revealed. Asides from adhesive force results, their interpretation and comparative studies with exiting models like JKR, DMT, modified Rumpf model, and Roninovich model are also presented.

4.3.1 Particle-particle interaction

The pull-off force tests are performed with 2.5 and 10 μm colloidal probes on SAM of 2.5 and 10 μm silica particles. A series of pull-off force tests is made in contact mode with AFM. Ideally, one would like to conduct the experiment to obtain the pull-off force of particle-particle interaction on an individual particle without interfering with other particles; therefore, prior to the test, an individual particle has been located by AFM scanning. Image resolution obtained by scanning with colloidal probe is not very high; however, it is enough to locate the particles unambiguously. The scanning areas are 10×10 and 30×30 μm^2 for 2.5 and 10 μm probes, respectively. After imaging, the probe is instructed to perform the pull-off force test on top of single particle and at the interface of 3 particles as shown in figure 4.4. The particles are loaded with different loads and then unloaded. The same scan area is again scanned to confirm that the test is done on the targeted position. The typical force-displacement curves for particle-particle interaction using the 2.5 μm probe are shown in figure 4.4. The average adhesion force of 2.5 μm interacting particles is about 294 and 98 nN for one particle to one particle and one particle to 3 particles, respectively. The average adhesion force of 10 μm interacting particles is 1029 and 335 nN for one particle to one particle and one particle to 3 particles, respectively (table 4.7).

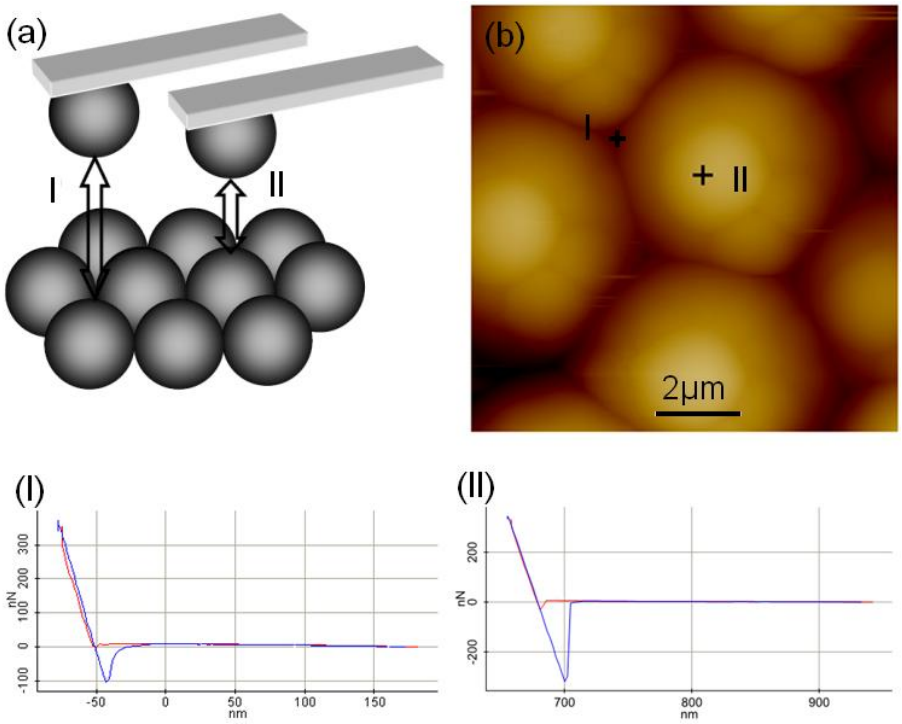

Figure 4.4: (a) Schematic diagram of interaction between adhering particle (colloidal probe) and SAM. (b) An AFM image of SAM of silica particles of 2.5 µm. (I) The graph depicts the force-displacement curve when the pull-off force test is performed at top of one particle (one particle to one particle). (II) The graph depicts the force-displacement curve when the pull-off force test is performed in between of three particles (one particle to 3 particles).

Table 4.7: Adhesion force for particle-particle interaction.

Adhesion Force	**one particle to one particle**	**one particle to 3 particles**
2.28 µm particle on 2.5 µm SAMs	294 ± 56	98 ± 18
10.25 µm particle on 10 µm SAMs	1029 ± 100	365 ± 22

The adhesion force for either one particle to one particle or one particle to 3 particles is increased with increasing the size of interacting particles. This can be explained by JKR and DMT model. According to JKR and DMT model, the adhesion force is given as

$$F_{ad(JKR)} = 3\pi\Delta\gamma R_{eq}, \tag{4.1}$$

$$F_{ad(DMT)} = 4\pi\Delta\gamma R_{eq}. \tag{4.2}$$

The particle-SAM interaction can be realized as schematic diagram (Figure 4.4(a, b)). Therefore, the equivalent radius (R_{eq}) can be calculated as

$$\frac{1}{R_{eq}} = \frac{1}{R_c} + \sum_{s=1}^{\infty} \frac{1}{R_s} \tag{4.3}$$

where R_c and R_s are the radius of adhering particle (colloidal probe) and interacting particles (particles on surface), respectively, and s is number of particles on the surface. It is found that the increment of adhesion force for one particle to one particle interaction, where the pull-of force tests are done on the top of a single particle, increases with radius of particle as same ratio of size of interacting particles. The adhesion force between one particle and three particles, where the pull-off force tests are done at the interface of 3 particles, increases as reduced radius increases. The reduced radius is calculated by using equation (4.3). The figure 4.5 shows the measured adhesion force with respect to reduced particle radii. The measured adhesion force increases linearly by increasing reduced radius. The little experimental error has been observed due to sufficient level of variation in size of particle in self-assembled monolayer; however, the size of particle on AFM cantilever is correctly measured using SEM.

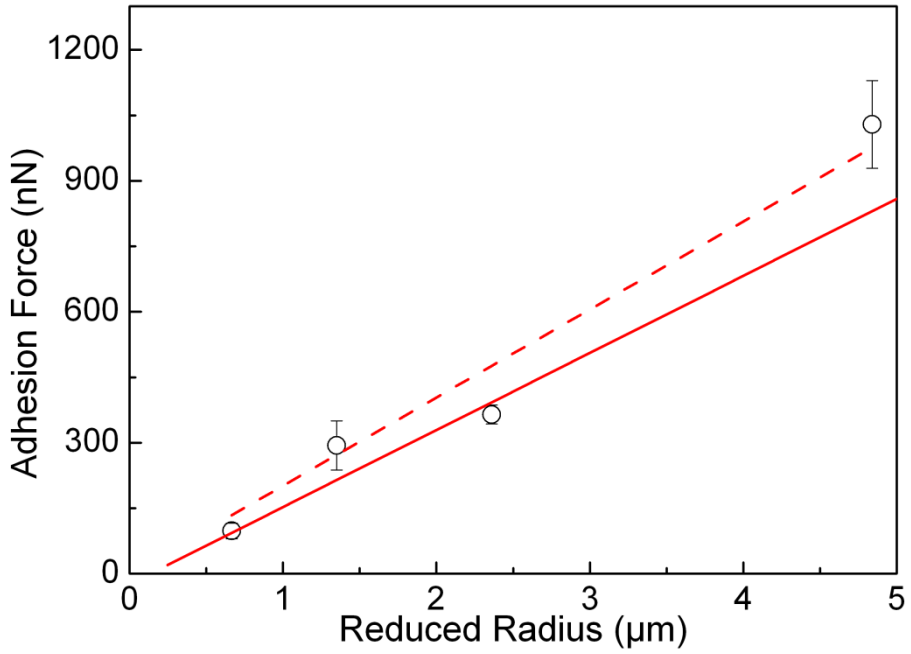

Figure 4.5: Adhesion force versus reduced particle radius. The straight line represents the best linear fit and gives a pull-off force of -23.97 nN at vanishing particle radius. The best linear fit to data points through the origin of the diagram has a slope of 0.202 N/m (dashed line).

4.3.2 Surface energy of silica particles

Figure 4.5 indicates that the measured adhesion force increases linearly by increasing reduced radius of interacting particles. By extrapolating to zero reduced radii, a linear fit gives a negligible force of -23.97 ± 24.08 nN with slope of 0.176 ± .014 N/m, as shown in figure 4.5 and the system can follow the JKR and DMT model as described in ref [44]. The best linear fit to the data points through the origin of the diagram has a slope of 0.202 ± 0.013 N/m, and this is taken as measured normalized adhesion force of F_{ad}/R. Hence, the calculated surface energies (γ) are found to be 22 ± 1 mJ/m^2 and 16 ± 1 mJ/m^2 using JKR and DMT models, respectively, as tabulated in table 4.8. The surface energies are slightly lower than 25 mJ/m^2 which has been determined from elastic behavior of silica power [151] or 40 mJ/m^2 which has been measured by modified surface force apparatus [152]. The relation between adhesion force and reduced radius is verified, but obtained surface energy is lower than the actual one. A significant difference may be due to error in adhesion force due to uncertainty of determining the spring constants of cantilevers, error due to uncertainty of slope of dashed line in figure 4.5, and error of reduced radius of adhering particles due to variation of size distribution of particle.

Table 4.8: Surface energies of silica particles.

Sample	Surface Energy, γ (mJ/m^2)
Silica particle/JKR	22 ± 1
Silica particle/DMT	16 ± 1

4.3.3 Particle on rough flat surfaces

The pull-off force tests on various rough surfaces are performed with various size of colloid probe or adhering particle using AFM. The radius of adhering particles is varied from 1.45 μm to 10.25 μm. The rms value is varied from 0.23 nm to 24 nm. A typical force-distance curve generated from AFM is shown in figure 4.6. The pull-off force or adhesion is defined as maximum negative force when the tip starts to withdraw from the surface (detail description is presented in chapter 3).

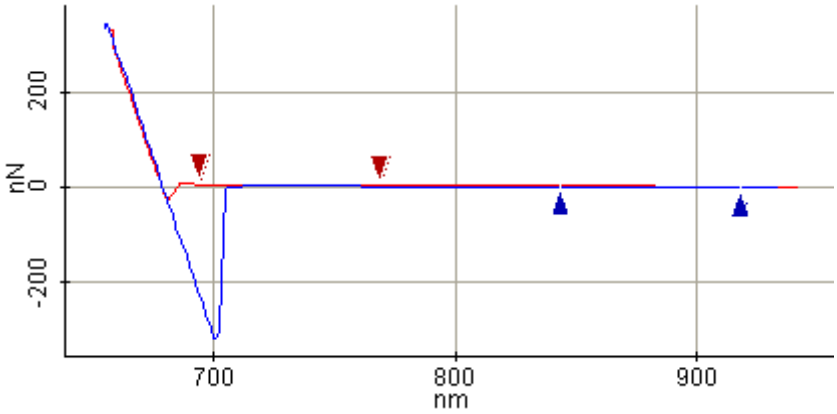

Figure 4.6: The graph shows the force measured by AFM-cantilever versus tip sample distance.

According to JKR and DMT models the adhesion force is independent of applying load or the contact time in predominantly elastic contact deformation load regime. If one of the contacting bodies shows the visco-elastic deformation, the contact area and adhesion force increase with contact time. When plastic deformation occurs, load depending adhesion force can be seen [38-43]. Heim et al. [44] and Ecke et al. [45] studied for silica particle to particle or silicon substrate and found that adhesion force is independent of loading force within a range, surrounding air pressure, and the relative humidity within a range. For adhesion measurements, load dependency on adhesion force has not seen; however, for avoiding any confusion, applied load have been kept constant. The fast approaching sped of 6 µm/sec of adhering particle to analyzed surfaces is used to prevent the hysteresis phenomena. The adhesion force between a spherical particle and smooth flat surface is given by JRK model as

$$F_{ad(JKR)} = \frac{3}{2}\pi R W_{12}, \tag{4.4}$$

where W_{12} is the work of adhesion per unit area between the AFM tip (subscript 2) and with material used (subscript 1). In agreement with the van Oss-Chaudhury-Good theory [153, 154], the work of adhesion W_{ij} is related to different components of the surface energy as

$$W_{ij} = 2\left(\sqrt{\gamma_i^{LW}\gamma_j^{LW}} + \sqrt{\gamma_i^{+}\gamma_j^{-}} + \sqrt{\gamma_i^{-}\gamma_j^{+}}\right) \tag{4.5}$$

where γ^{LW} is the apolar (Lifshitz-van der Waals) surface energy component, γ^{+} is the electron-acceptor surface energy parameter, and γ^{-} is the electron-donor surface energy parameter. Table 4.9 shows the surface energy components [155].

Table 4.9: Surface energy components of the materials.

Materials	γ^{LW} (mJ/m^2)	γ^{+} (mJ/m^2)	γ^{-} (mJ/m^2)
Silica Glass	32.9 ± 0.4	0.4 ± 0.3	37.4 ± 0.5
Silicon (100)	36.5 ± 0.4	0.6 ± 0.5	29.0 ± 0.5
DLC	37.4 ± 0.4	0.12 ± 0.1	19.7 ± 0.5

If the adhering particles, silicon surface, and DLC surface are assumed to be rigid and smooth, then JKR model can be applied. The adhesion force using JKR model is calculated for silicon and DLC surfaces using the surface energy components from table 4.9. The theoretical JKR adhesion force and experimental values are tabulated in table 4.10.

Table 4.10: Theoretical and experimental adhesion force between silica particle and silicon, DLC surfaces.

Sample	1.45 µm particle	2.78 µm particle	7.59 µm particle	10.25 µm particle
Silicon/JKR	585	1121	3060	4132
DLC/JKR	273	524	1430	1931
Silicon/Experimental	90 ± 9	217 ± 50	631 ± 61	1277± 192
DLC/ Experimental	48 ± 18	65 ± 9	313 ± 70	355 ± 44

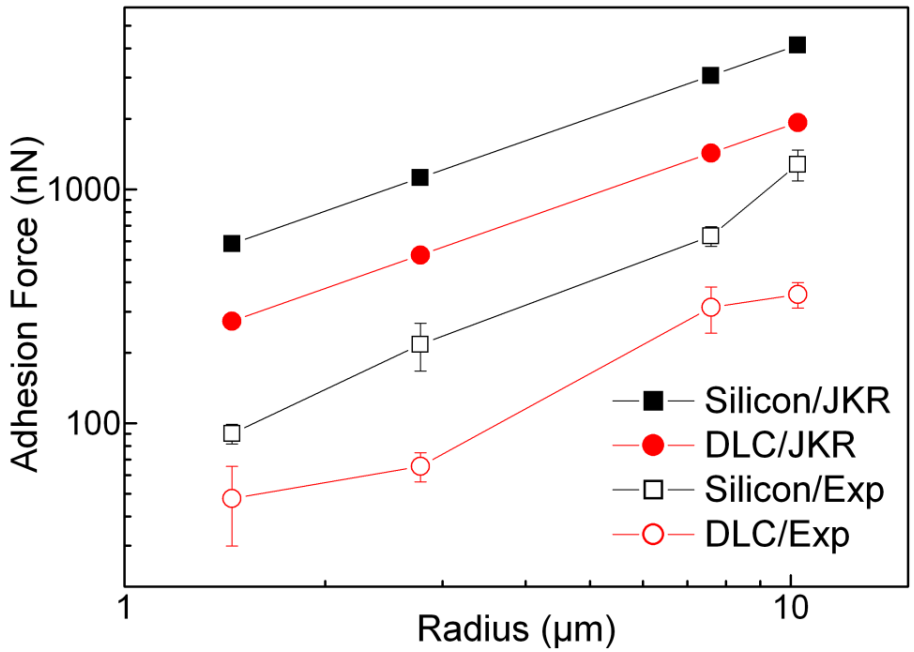

Figure 4.7: Theoretical and experimental adhesion force between silica particle and silicon, DLC surfaces. The adhesion force is plotted against the radius of adhering silica particle.

The adhesion force is found to be increased with increasing the size of adhering particle (colloidal probe) for smooth silicon and DLC sample as shown in figure 4.7. The theoretical JKR adhesion force of silicon and DLC surfaces is higher than the experimental results. It is earlier mentioned that silicon, DLC surfaces, and surface of adhering particles are not perfectly smooth and they posses finite surface roughness and JKR model is only valid for perfect smooth surface. Thus a difference between experimental and theoretical results is seen and this difference increases with further increasing the roughness

The adhesion force is turned out in unique trend with surface roughness (table 4.11). The highest values of adhesion force is obtained as from 90 to 1277 nN for smooth silicon surface using different size of adhering particles range from 1.45 to 10.25 μm. The adhesion force initially decreases with increasing the roughness and then it starts to increase with further increasing the roughness. This observation is shown for all size of particles except for the 10.25 μm adhering particle, which only shows decreasing trend for adhesion force on increasing the roughness. Several studies show that adhesion force is dependent on surface roughness, and dramatical reduction of adhesion is observed due to a decrease in the real area in contact and increase in the distance between bulk surfaces [36, 46-49].

Table 4.11: Adhesion force obtained from different size of adhering particles (colloidal probes).

rms (nm)	1.45 μm particle	2.78 μm particle	7.59 μm particle	10.25 μm particle
0.23±0.1	90 ± 9	217 ± 50	631 ± 60	1277± 192
4.1±0.1	47 ± 18	65 ± 9	312.7 ± 70	355 ± 44
11.7±0.6	80 ± 30	92 ± 24	242 ± 26	256 ± 36
23.9±0.3	111 ± 22	129 ± 40	282 ± 71	168 ± 49

4.3.4 Comparison with the modified Rumpf and Rabinovich model

The Rumpf's model [50] is proposed a theoretical prediction for adhesion force and the following equation (4.6) is obtained.

$$F_{ad} = \frac{H_0}{6z_0^2}\left[\frac{rR}{r+R} + \frac{R}{\left(1+\frac{r}{z_0}\right)^2}\right] \quad (4.6)$$

Hamaker constant (H_0) can be approximately 1.31×10^{-19} J for the silica/silicon contact [53, 54], and the value of z_0 is usually considered to be 0.3. By substituting r = 1.485rms into the equation (4.6) for silicon samples, the value from model prediction is lower than the experimental values as in table 4.12; this may be due to limitation of model. This comparison is only valid if the center of asperities is assumed to be lie at surface and radius of asperities increases with increasing roughness. For realistic study, the surface roughness decreases with increasing the roughness and center of asperities lies below the average surface plane.

Since the vertical scale is greatly exaggerated, the asperities should be as spherical with the origin below the surface instead of semispherical. Hence the asperity is scaled by using both the measured height and breadth. Silicon surface profile is investigated using AFM and the silicon surface profile depicts that the roughness (rms_2) and peak-to-peak distance (λ_2) are 0.23 nm and 112 nm, as reported in table 4.3. Applying the Rabinovich model [53], the following equation for adhesion force is obtained.

$$F_{ad} = \frac{A_H R}{6H_0^2}\left[\frac{1}{1+\left(\frac{32Rk_1 rms}{\lambda^2}\right)} + \frac{R}{\left(1+\frac{k_1 rms}{H_0}\right)^2}\right] \tag{4.7}$$

Using $k_1 = 1.817$ in above equation (4.7), the adhesion forces for silicon sample are calculated (table 4.12). The Rabinovich model produces higher adhesion force values than the modified Rumpf model and more close to the experimental results; see in figure 4.8. The experimental adhesion force within the standard deviation is similar with the one produced from the Rabinovich model for 2.78 and 7.59 μm adhering particles, whereas this is not seen for 1.45 and 10.25 μm adhering particles. The theoretical prediction by Rabinovich model for 1.45 μm adhering particle is higher than the experimental results. This can be explained by the roughness of adhering particle, which is about 2 nm, and the roughness on the adhering particle surface effectively reduces the contact area, and hence the adhesion force is reduced. The influence of roughness on the surface of adhering particle may reduce with size of particles. This is clearly shown in figure 4.8 that the difference between theoretical and experimental adhesion force decreases with increasing the size of adhering particle. It also shows that the roughness on adhering particle is not important for larger particle and predicting value is very close to the experimental result.

Table 4.12: Summary of adhesion forces between silica particle and silicon surface. The adhesion force for Rumpf and Rabinovich model is calculated using λ = 112 nm, rms = 0.23 nm, $A_H = 1.31X10^{-19}$ J, and H_0 = 0.3 nm.

Adhesion force (nN)	Rumpf model	Rabinovich model	Experimental
Silicon /1.45 µm silica probe	80 ± 22	202 ± 55	90 ± 9
Silicon /2.78 µm silica probe	154 ± 43	298 ± 89	217 ± 50
Silicon /7.59 µm silica probe	420 ± 117	553 ± 163	631 ± 61
Silicon /10.25 µm silica probe	546 ± 158	679 ± 196	1277± 192

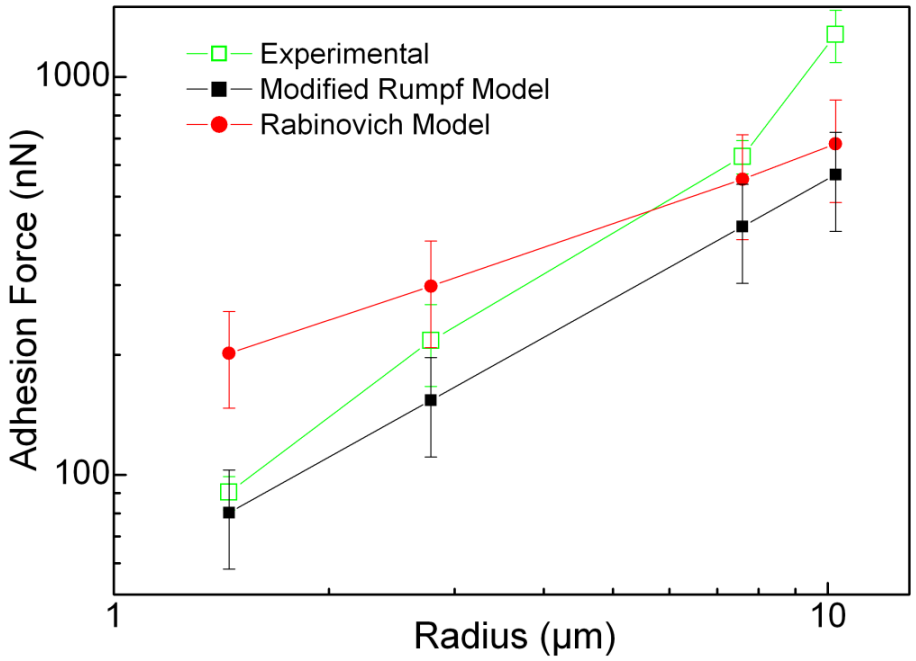

Figure 4.8: Adhesion forces of silicon surface vs. radius of adhering silica particle. The adhesion force for Rumpf and Rabinovich model is calculated using λ = 112 nm, rms = 0.23 nm, $A_H = 1.31X10^{-19}$ J, and H_0 = 0.3 nm.

Theoretical adhesion forces for DLC surfaces proposed by Rabinovich model are calculated using $A_H = 1.08x10^{-19}$ J and H_0 = 0.3. The equation (4.7) is utilized in calculating the theoretical adhesion force for 4 nm-DLC surface. Since the 12 nm-DLC and 24 nm-DLC surfaces exhibit two types of asperities: primary and secondary asperities; therefore, equation (4.8) is employed to calculate the theoretical adhesion forces for 12 nm-DLC and 24 nm-DLC. The theoretical as well as experimental normalized adhesion force (F_{ad}/R) vs. surface roughness (rms) for 10.25 and 7.59 µm adhering particles is plotted (figures 4.9).

$$F_{ad} = \frac{A_H R}{6H_0^2}\left[\frac{1}{1+\left(\frac{58R(rms_2)}{\lambda_2^2}\right)} + \frac{1}{\left(1+\frac{58Rrms_1}{\lambda_1^2}\right)\left(1+\frac{1.82rms_2}{H_0}\right)^2} + \frac{H_0^2}{(H_0+1.82(rms_1+rms_2))^2}\right] \quad (4.8)$$

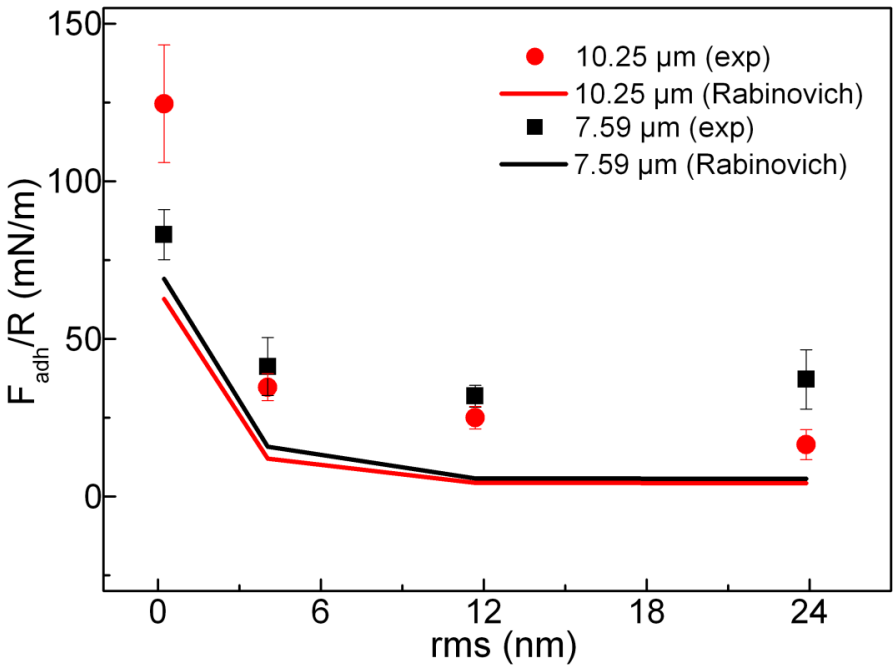

Figure 4.9: Theoretical and experimental normalized adhesion force vs. roughness of surface (rms) derived with 10.25 and 7.59 µm adhering particles.

According to Rabinovich model, the normalized adhesion force decreases with surface roughness. From figure 4.9, it is observed that the experimental normalized adhesion force shows highest values for 0.23 nm rough surface. It is observed for both 10.25 and 7.59 µm adhering particles. On increasing the surface roughness from 0.23 nm to 4 nm rms, the normalized adhesion force drastically decreases. On further increasing the roughness, the normalized adhesion force shows two types of trend. The normalized adhesion force for 10.25 µm adhering particle is slowly decreased with surface roughness. For 7.59 µm adhering particles, a constant normalized adhesion force is found for surface roughness from 4 nm to 24 nm rms. The prediction of Rabinovich model is lower than the experimental results. This may be due to inaccurate A_H and H_0 values. The theoretical as well as experimental normalized adhesion force (F_{ad}/R) vs. surface roughness (rms) for 2.78 and 1.45 µm adhering particles are plotted as shown in figures 4.10.

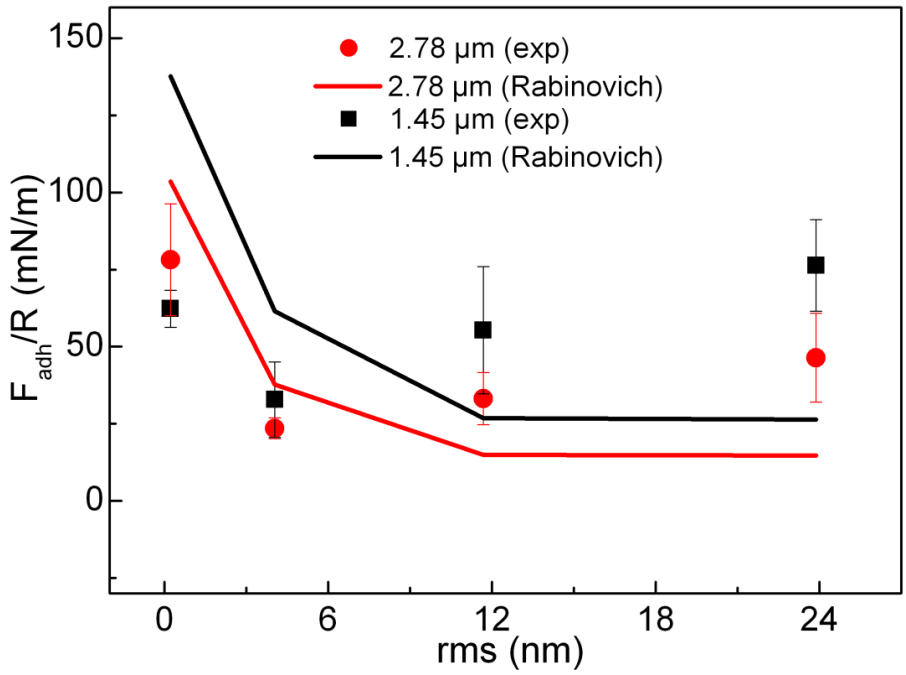

Figure 4.10: Theoretical and experimental normalized adhesion force vs. roughness of surface (rms) derived with 2.78 and 1.45 µm adhering particles.

According to Rabinovich model, the normalized adhesion force decreases with surface roughness for both 2.78 and 1.45 µm adhering particles as shown in figure 4.10. The experimental normalized adhesion force shows highest value for 0.23 nm rough surface. On increasing the surface roughness from 0.23 nm to 4 nm rms, the normalized adhesion force drastically decreases as predicted by Rabinovich model. The prediction by Rabinovich model is higher than the experimental results. This may be due to use of inaccurate A_H and H_0 values as well the influence of roughness on adhering particles. At higher level of surface roughness, the experimental normalized adhesion force increases with surface roughness but no increase in normalized adhesion force is observed by Rabinovich model. This may be due to the influence of several factors. The Rabinovich mdoel has a limitation in terms of size and geometry of asperities. It is earlier observed that size of both adhering particles (1.45 and 2.78 µm) is comparable to size of primary asperities of both rough DLC surfaces (12 and 24 nm). The interaction between these adhering particles and secondary asperities may be at several points, as see in figure 4.11 (c, d, e). This suggests that the Rabinovich model is not suitable to measure the adhesion force between adhering particle and rough surfaces where the size of adhering particle is comparable to size of asperities.

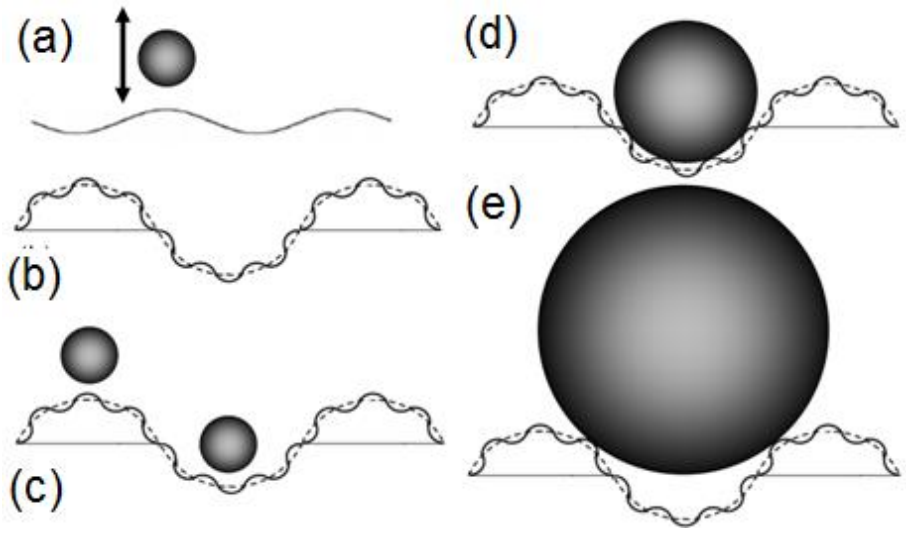

Figure 4.11: (a) Schematic diagram of particle-smooth surface interaction. (b) Surface showing secondary asperities superimposed on primary asperities. (c) Schematic diagram of particle-rough surface interaction ($r_1 > R$). Particle interaction between hilly and valley portion of primary asperity of surface. (d) Schematic diagram of particle and valley portion of primary asperity. Showing multiple interactions of adhering particle and secondary asperities. Here r is comparable to R. (e) Schematic diagram of particle-rough surface interaction ($r_1 < R$).

4.3.5 Comparison with the proposed model (Van der Waals approach)

Through AFM image profile of rough surfaces (figure 4.2), it is clearly seen that the geometries of asperities of treated surfaces in this study are not resembled as the Rumpf model described the asperity geometry at nanoscale. The asperity geometry is found to be similar as the Rabinovich model. Rabinovich model is based on approach where interaction between adhering particle and hemispherical caps (hills) on a smooth substrate is assumed. This approach underestimates the role of valley (cups) of asperities and completely neglects the contact interaction between adhering particle and valley portion of asperities as shown in figure 4.11 (a). This negligence is considerable because the size or radius of asperity can only increase at where surface roughness is relatively low i.e. smooth surface and for such surface interaction between adhering particle and average surface plane dominates.

In contrast, the radius of asperities increases with the increment of surface roughness at nanoscale with multi-scale asperities, such as secondary asperities are superimposed on primary asperities as shown in figure 4.11 (b). Consider the case where radius of adhering particle is lower than the radius of primary asperities ($r_1 > R$) as in figure 4.11 (c and d). The

adhering particle will interact only one secondary asperity if the adhering particle comes in contact exactly at the top of hilly portion of primary. This is ideal situation of the Rabinovich model and the equation (4.8) is valid. If the adhering particle comes into the contact of the valley portion of primary asperities, then the adhering particle interacts with multiple secondary asperities. The number of secondary asperities (n_{sa}) in contact at such situation is extremely difficult to calculate; however, the number of secondary asperities in contact lies in between 1 to $\pi R/\lambda_1$. Finally the equation (4.8) will replace with equation (4.9).

$$F_{ad} = \frac{A_H}{6H_0^2}\left[n_{sa} \cdot \frac{r_2 R}{r_2+R} + \frac{r_1 R}{(r_1 - R)(1+y_{max}/H_0)^2} + \frac{R}{(1+(y_{1max}+y_{2max})/H_0)^2}\right] \text{ or}$$

$$F_{ad} = \frac{A_H R}{6H_0^2}\left[n_{sa} \cdot \frac{1}{1+\left(\frac{58R(rms_2)}{\lambda_2^2}\right)} + \frac{1}{\left(1-\frac{58Rrms_1}{\lambda_1^2}\right)\left(1+\frac{1.82rms_2}{H_0}\right)^2} + \frac{H_0^2}{\left(H_0+1.82(rms_1+rms_2)\right)^2}\right] \quad (4.9)$$

In above equation, three terms are corresponding to the interaction between adhering particle and n_{sa}-number of secondary asperities, primary asperity, and the average plane surface, respectively. In denominator of second term, the negative sign is due to the interaction of the adhering particle and the valley portion of primary asperities. Therefore, when radius of primary asperities is higher than the radius of adhering particle, the adhesion force is completely dependent on number of secondary asperities in contact.

The equation (4.9) is valid only when the $\lambda_1 > \sqrt{58Rrms_1}$ and critical peak-to-peak distance of primary asperities ($\lambda_{critical} = \sqrt{58Rrms_1}$) is calculated for all adhering particle and rough DLC surfaces (table 4.13). The values of λ_1 for 12 and 24 nm-DLC are higher than the values of $\lambda_{critical}$ for 1.45 and 2.78 µm adhering particles; however, λ_1 of 12 and 24 nm-DLC is lower than the $\lambda_{critical}$ of 7.59 and 10.25 µm adhering particles. Therefore equation (4.9) is only valid with 1.45 and 2.78 µm adhering particles and for 12 and 24 nm-DLC surfaces. The perimeter of curvature of primary asperities of 12 and 24 nm-DLC surfaces and number of secondary asperities lies on the valley portion of primary asperities are calculated (table 4.14). 4 and 6 numbers corresponding to 12 and 24 nm-DLC surfaces are received, respectively; i. e. numbers of secondary asperities in contact (n_{sa}) are 4 and 6. Using these n_{sa} values theoretical adhesion forces are calculated by employing equation (4.9) for 1.45 and 2.78 µm adhering particles and corresponding results are plotted in figure 4.12. In this calculation, A_H is 1.08×10^{-19} J and 1.31×10^{-19} J for silica/DLC and silica/silicon, respectively and H_0 is taken to be 0.3. A very good correlation is found between experimental and theoretical normalized

adhesion force. A difference between their actual values is observed due to inaccurate A_H and H_0 values.

Table 4.13: Critical peak-to-peak distance for adhering particle and rough DLC surfaces.

Particle (µm)	$\lambda_{critical}$ for 12 nm-DLC	$\lambda_{critical}$ for 24 nm-DLC
1.45	962	1407
2.78	1332	1949
7.59	2200	3220
10.25	2563	3750

Table 4.14: Number of secondary asperities lies on the primary asperities for rough DLC surfaces.

Sample	Perimeter of curvature of primary asperities(nm)	No of secondary *asperities* lies on primary asperities (n_{sa})
12 nm-DLC	905	4
24 nm-DLC	1303	6

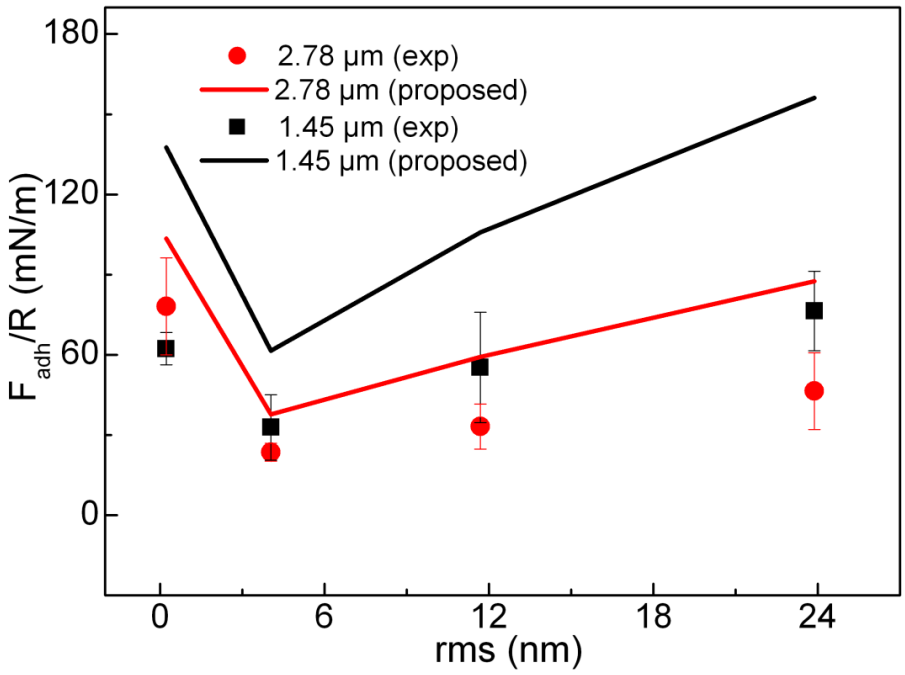

Figure 4.12: Theoretical and experimental normalized adhesion force vs. roughness of surface (rms) derived with 2.78 and 1.45 µm adhering particles.

If adhering particle size is lower than the primary asperities, then adhesion force increases due to multiple secondary asperities contact. On the other hand, if adhering particle size is higher than the primary asperities, then adhesion force decreases due to single point (secondary asperities) contact. The relative surface roughness (rms/R) is important in determining the adhesion force. The normalized adhesion force is plotted against the normalized or relative surface roughness (rms/R); see the figure 4.13. These values are measured between adhering particle and rough surface. The highest normalized adhesion force is observed at lowest rms/R value, which is measured between very smooth surface (silicon) and largest adhering particle (10.25 µm). The normalized adhesion force decreases with increasing rms/R. It is earlier mentioned that on increasing the roughness, the contact area decreases and adhesion force decreases. This observation is noticed up to 0.0025 value of rms/R. In this rms/R range, Rabinovich model is valid. Beyond 0.0025 of rms/R, the normalized adhesion force increases with rms/R. This is measured between the relatively small adhering particles (1.45 and 2.78 µm) and rough surfaces (12-nm and 24-nm DLC). Increasing normalized adhesion force is the result of interaction between small particles and rough surfaces, wherein the size of adhering particle is comparable to asperities and contact area increases with rms/R. This finding also helps to tailor the material surface. In literature, it is earlier mentioned that surface roughness at nanoscale leads to the reduction of contact area and the adhesion force will be decreased. From the present study, this phenomenon is observed if size of adhering body is 300-1000 times of rms of surface. Therefore, this finding could assist in designing of materials surface for several applications.

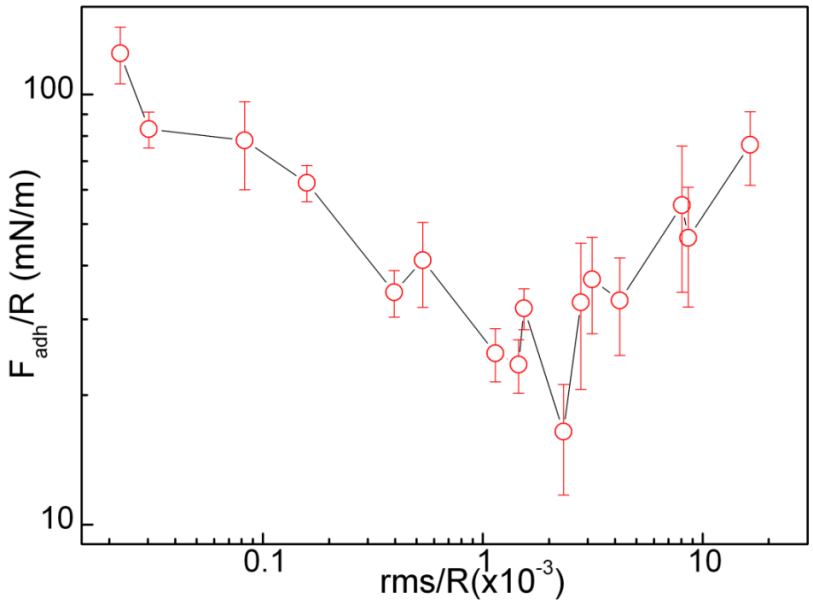

Figure 4.13: Normalized adhesion force (F_{adh}/R) vs. normalized surface roughness (rms/R).

4.4 Tribological results

The friction coefficient (μ) is defined as the ratio of the friction force or lateral force (F_{fr}), the resistance which opposed the motion, and the normal load (P). Several studies have shown that the friction force for a single asperity contact is proportional to true contact area [67]. For ultra-smooth contacts in predominantly elastic contact regime, the Hertz theory can be applied [2]. Hertz theory describes the contact area for smooth macroscopic contacts. For a spherical probe the friction coefficient (μ) has the relationship with applying load (P) as equation (4.10).

$$\mu = \pi\tau \left(\frac{3R}{4E^*}\right)^{2/3} (P)^{-1/3} \tag{4.10}$$

In elastic contact load regime, the friction coefficient decreases with applied load. Beyond the elastic contact load regime, the friction coefficient arrives at constant value. In this load range, the lateral force is subjected to equation (4.11).

$$F_{fr} = \mu_T P \tag{4.11}$$

where μ_T is frictional properties of the materials and friction coefficient is constant ($\mu = \text{constant}$). In contrast at higher load regime, wherein the contact is predominately plastic, the friction coefficient is increases as

$$\mu = k_0 \sqrt{\frac{P}{R^2 \sigma_y}} \tag{4.12}$$

where k_0 is constant. One can say that the friction coefficient decreases with increasing normal load at an early stage of applied normal load for perfectly smooth surface and rigid spherical indenter, and an increase of the normal load during scratching typically results in constant friction coefficient (Coulomb's law). In contrast at high level of applied normal load, the friction coefficient initially increases in a parabolic manner and subsequently linear manner (see figure 4.14).

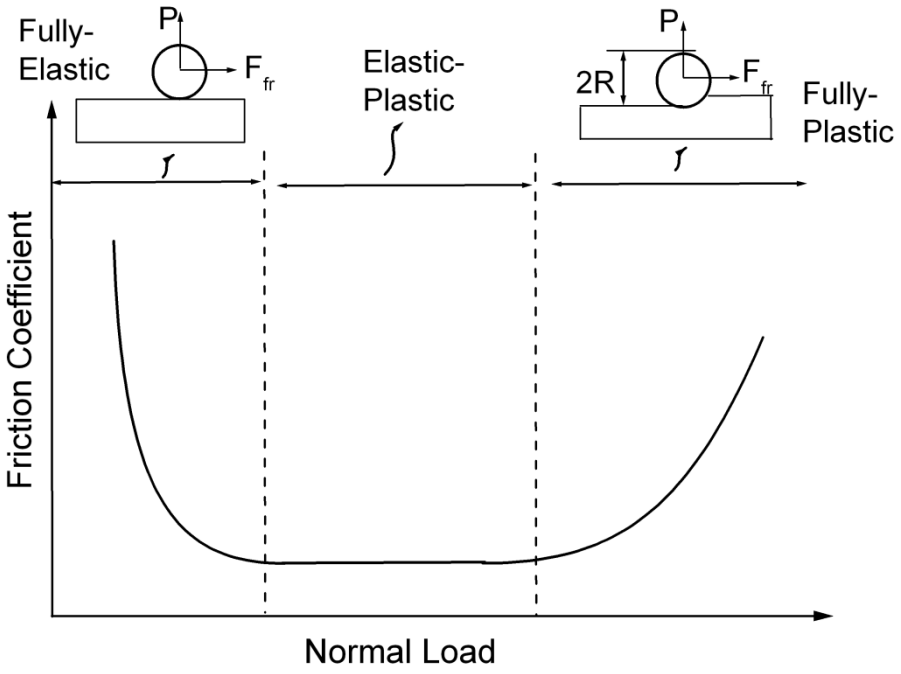

Figure 4.14: Schematic diagram of friction coefficient vs. normal load curve.

In fully elastic contact load regime, deformation of asperities is reversible or non-permanent, and a decreasing friction coefficient is noticed. The transition from decreasing friction coefficient to constant friction coefficient corresponds to a transition from a predominantly elastic contact to an elastic-plastic contact. In fully plastic contact load regime, asperities deform permanently and an increase friction coefficient is seen. In other words, at low loads a Hertzian contact behavior along with transition regime between elastic and plastic contact is observed, followed by a plastic deformation dominated normal load regime. The critical load range is then defined either as the transition from predominately elastic contact regime to elastic-plastic contact regime, from elastic-plastic contact regime to predominately plastic contact regime, or from predominately elastic contact regime to predominately plastic contact regime.

For perfectly smooth surface and rigid spherical indenter, the friction coefficient and critical load ranges are mainly dependent on mechanical properties of surface and radius of probe. In reality, a surface is featured with hills and valley often called surface asperities. By scratching on those surfaces, the yield of asperities will be at lower applied load and critical load range will be different. The adhesion force provides an additional normal load when two bodied are in contact and leads to an existence of lateral force at nonzero applied load. The external parameters such as scratch speed and loading rate change the stress field, and results into different critical load range. The parameters such as radius of probe, adhesion force, surface

roughness, mechanical properties of analyzed samples, scratching speed, and loading rate will be discussed in detail in this sub-chapter.

4.4.1 Probe size

Lateral force increases with radius of probe while other scratching parameters such as roughness, material, and applied normal load are kept constant. Figure 4.15 depicts the variation of the lateral force against the applied normal load with 2.78 and 10.25 µm colloidal probes used in AFM. This observation is seen for all samples.

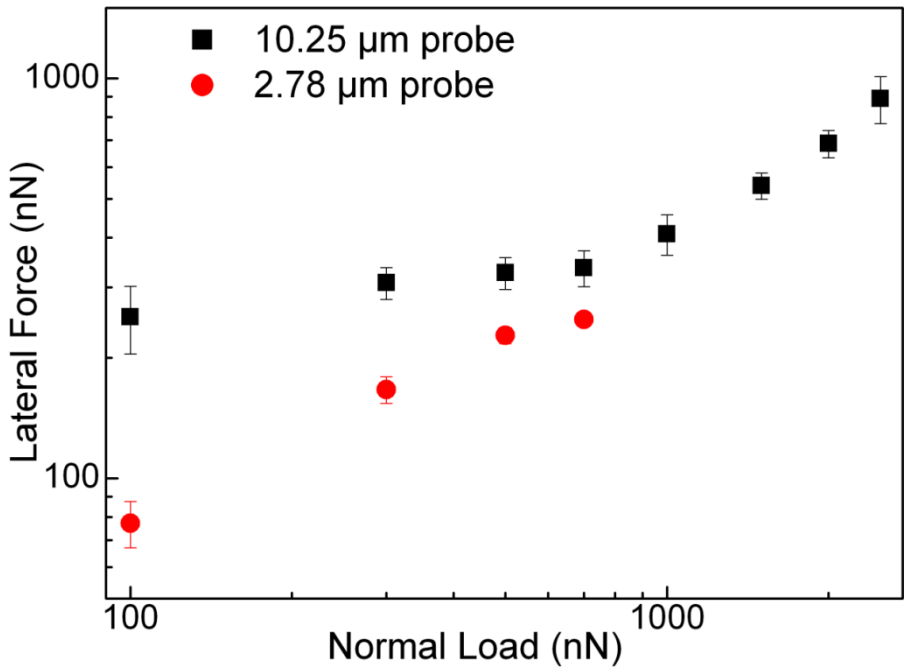

Figure 4.15: Logarithmic plot of lateral force vs. normal load for the silica sample derived with both colloidal probes using AFM.

Increasing lateral force with radius of probe could be explained by considering the fundamental law of friction given by Bowden and Tabor [156]. According to this law, the friction force is directly dependent on the real area of contact, for a single asperity contact (equation (4.13)).

$$F_{fr} = \tau \cdot A \tag{4.13}$$

The contact area in elastic contact load regime can be calculated using Hertz and JKR models. It is earlier noticed that adhesion force is dominated in case of silica particle and silica surface. JKR model is employed to estimate the contact area, if the silica surface is assumed

perfectly smooth. Assuming the contact at such scale is a pseudo-single asperity contact, the contact area can be calculated by given equation (4.14).

$$A = \pi\left(\frac{3R}{4E^*}(P + 3\Delta\gamma\pi R + \sqrt{6\Delta\gamma\pi RP + (3\Delta\gamma\pi R)^2}\right)^{2/3}. \quad (4.14)$$

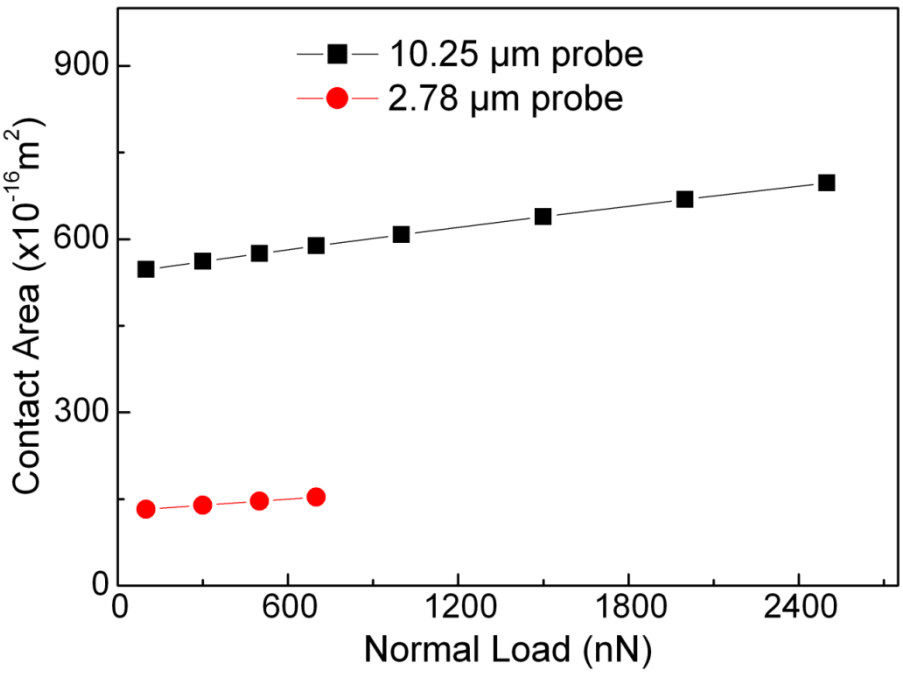

Figure 4.16: Contact area vs. normal load for the silica sample derived with both colloidal probes. Contact area are obtained using JKR model.

The figure 4.16 depicts the estimated contact area for silica sample with the applied normal load using 2.78 and 10.25 µm colloidal AFM probes. It can be observed that the contact area increases with the tip size. The lateral force increases with the tip size due to increasing the contact area. Figure 4.17 depicts the lateral force as a function of contact area between tip (10.25 and 2.78 µm) and silica sample. Yoon et al. [157] also calculated the contact area using JKR model for silicon and DLC, and observed that the contact area increases with the applied load and the tip size due to the increase in the real area of contact. Bhushan et al. [159] and Bhushan et al. [160] have also observed similar relationship between the friction force and the contact area for silicon and DLC.

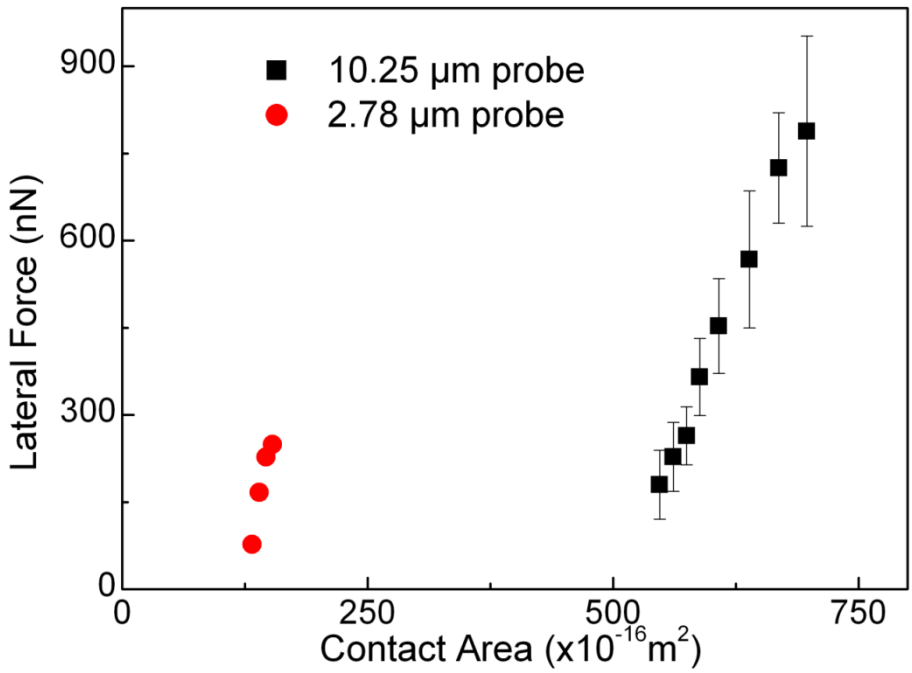

Figure 4.17: Lateral force vs. contact area for the silica sample derived with both colloidal probes. Contact area are obtained using JKR model.

The lateral force derived with 20 µm indenter is also observed higher than the one with 1 µm indenter, but this observation is only seen in a certain range of applied load, as shown in figure 4.18. The lateral force of aluminum sample for 20 µm indenter is higher than 1 µm indenter in load range of 0-50 µN. When applied load is higher than 70 µN load, the lateral force decreases with the size of the indenter. This phenomenon is also seen for silica and DLC surfaces. Decreasing the lateral force with radius of indenter at higher loads can be explained by contribution of plowing. Considering the size effect, the plowing component of lateral force (F_{fr}) has a direct [161], but inverse relationship with the radius of indenter (R) and the relationship is given as

$$F_{fr} = \frac{w_t^3 P}{12R} \tag{4.15}$$

where w_t is the track width. Furthermore, it can be considered that the surface makes multiple asperity contacts at very high applying load, and the plowing term reduces with increase in the number of points of contact for the same load. This also explains a decreasing lateral force with the radius of indenter at higher level of applying loads. Since friction coefficient is defined as ratio of lateral force to applied normal load, the friction coefficient is increased with radius of indenter in low level of applied load, and friction coefficient decreases with radius of indenter at high level of applying load.

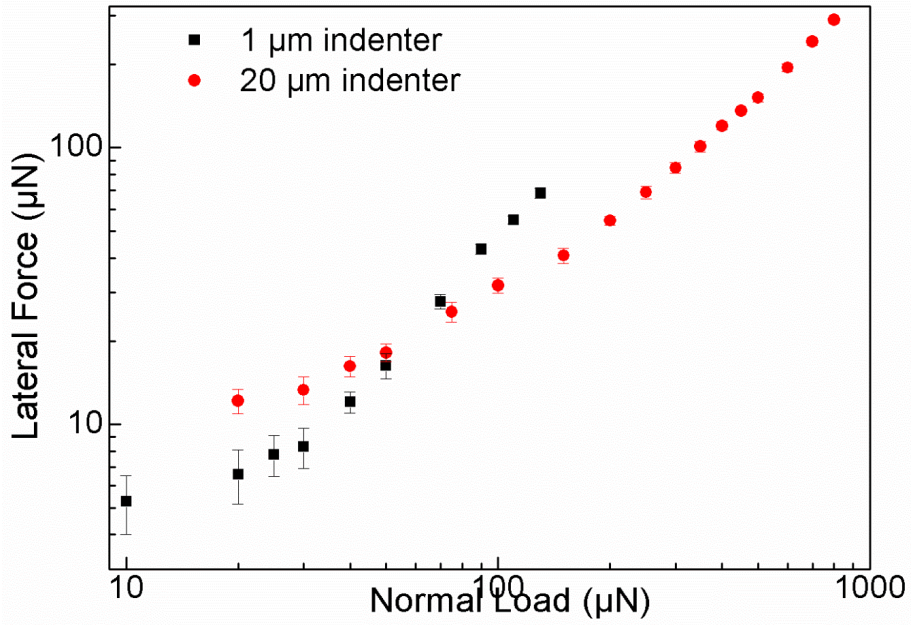

Figure 4.18: Logarithmic plot of lateral force vs. normal load for the aluminum sample derived with both diamond indenters. These results are obtained using Nanoindenter.

It is observed that the critical load ranges increase with the radius of indenter. The figure 4.19 shows the critical load values for all samples. For silica sample, the critical load range for transition from predominately elastic contact regime to elastic-plastic contact regime is around at 200 and 400 µN with 1 and 20 µm indenter, respectively, and critical load range for transition from elastic-plastic contact regime to predominately plastic contact regime is observed at around 1000 and 3000 µN with 1 and 20 µm indenter, respectively. For smooth DLC sample, critical load range for transition from elastic to elastic-plastic contact regime is observed at around 200 and 400 µN with 1 and 20 µm indenter, respectively. For rough DLC sample, no critical load range is identified. For aluminum sample, the critical load range for transition from predominately elastic to predominately plastic contact regime is at around 30 and 110 µN with 1 and 20 µm indenter, respectively. It is previously explained that the contact area increases with indenter size. The higher contact area provides the lower yield of asperities deformation, and load has to be increased to get permanent plastic deformation of asperities. Thus elastic deformation load regime enhances and critical load range increases.

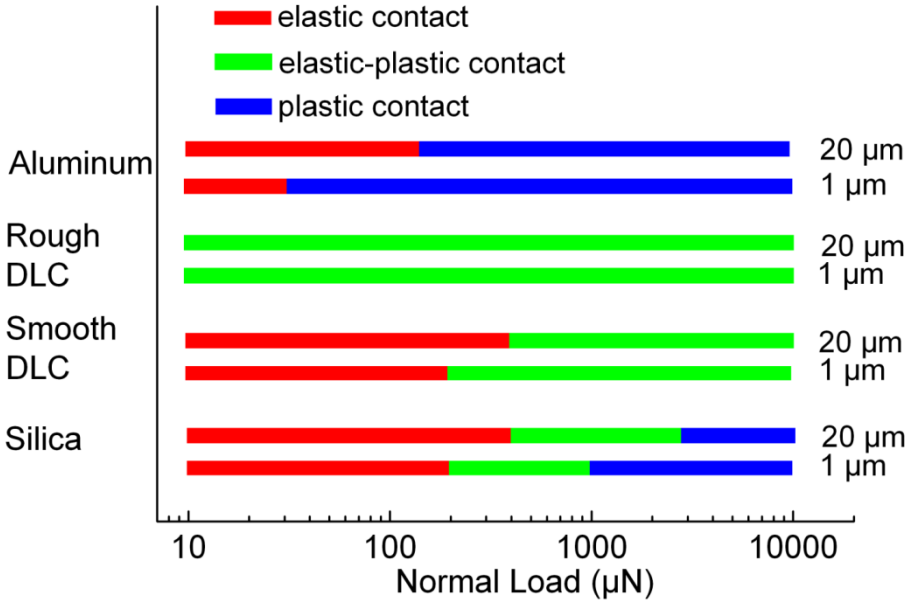

Figure 4.19: Critical load values for silica, DLCs, and aluminum sample derived with 1 and 20 µm indenters. A red strip show the elastic contact, green is for elastic-plastic contact and blue is for plastic contact regime.

4.4.2 Surface roughness

Since the analyzed surfaces are not smooth, contact occurs only at discrete contact points which sustain the total compressive force. During scratching, interfacial forces, that are responsible for friction, are generated at these contact points and eventually the friction results will be different. At a given load and radius of tips, friction coefficients show finite errors and these are shown as error bars in friction coefficient curves. The error bar increases with applied load as well as surface roughness. The error in friction coefficient becomes predominant at high level of applying loads and for rough surfaces due to stick-slip phenomena (figure 4.20). Stick-slip increases with surface roughness and applying load. It is observed that the silica and aluminum surfaces do not show any stick-slip even though applied load is in predominantly plastic contact regime. On the other hand, both DLC samples show the stick-slip phenomena.

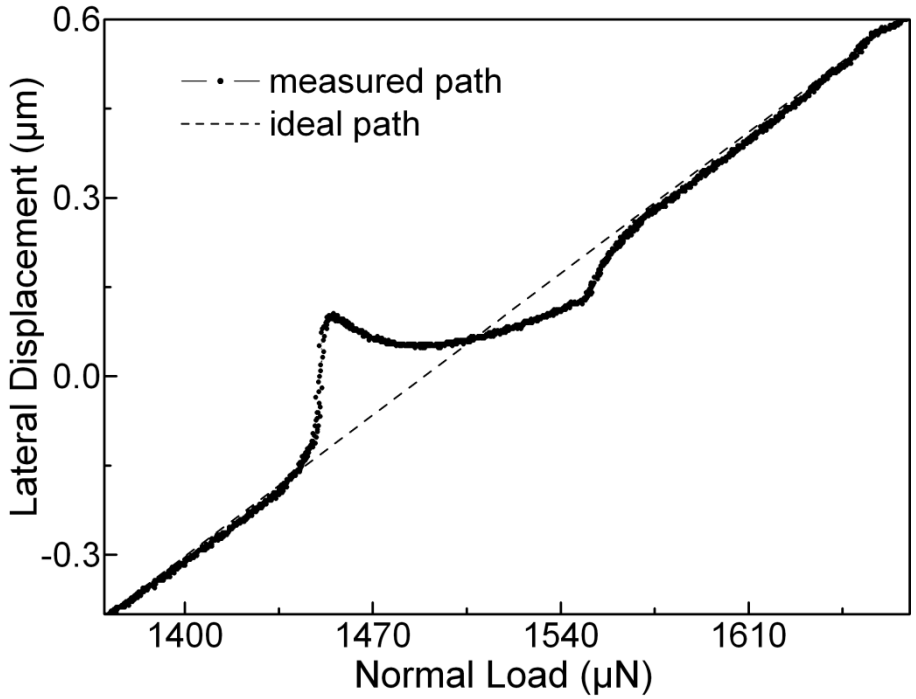

Figure 4.20: Topography induced artifact during a scratch test. The tip leaves its predefined displacement-load-path due to a stick-slip effect caused by a surface asperity or a constellation of several asperities. Measured data as well as the ideal path (dashed line) are shown.

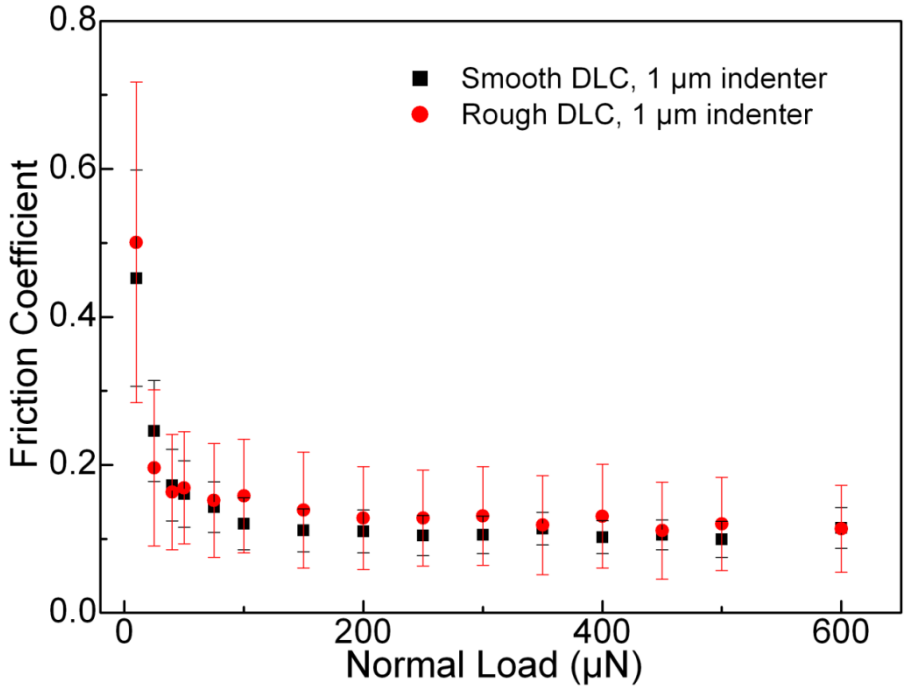

Figure 4.21: Lateral force vs. normal load for DLC samples derived with 1 µm indenter.

The figure 4.21 depicts the friction coefficient vs. normal load for DLC samples. Both rough and smooth DLC samples show similar average friction coefficient but standard deviation of friction coefficient for rough DLC surface is higher than the one for smooth DLC surface. The deformation of asperities increases on increasing the roughness of surface and error bars in friction coefficient increases. This is also seen in the results produced form AFM using colloidal probes.

The friction coefficient of smooth surfaces (silica, and aluminum) exponentially decreases with applied load in the low load range and follows the 1/3rd rule of Hertz ($\mu \propto P^{-1/3}$). The friction coefficient of DLC samples exponentially decreases with applied load in the low load range; however, it does not follow the 1/3rd rule of Hertz. This is basically due to the surface roughness. Surface roughness of DLC sample leads to the smaller contact area compared with the nominal contact area. To determine the real contact area and separation between contacting surfaces, several studies has been done. Greenwood and Williamson model (GW model) [23] showed that for arbitrarily shaped surfaces, the actual contact area will be proportional to the load. In the Hertzian case, it is known that the contact area is proportional to $P^{2/3}$. This dependency will be $P^{1/2}$ for pyramidal-shaped or conical tips. Therefore it might be possible, for low level of applied normal load regime, to approximate the contact area-load dependence by following equation with $0 < m < 1$

$$A \propto P^{m}. \tag{4.16}$$

This equation leads to load dependent friction coefficient as

$$\mu \propto P^{-m} \tag{4.17}$$

The prediction made by GW model is mainly suitable for pure elastic contacts. Besides elastic contact models, several studies have been done for plastic contact, showed by Abbott et al. [68]. Chang et al. [25, 26] (CEB model) made first attempt to account for elastic-plastic asperities contacts. This model is based on GW model and law of volume conservation for asperities. The CEB friction model underestimates the static friction coefficient, especially for higher plasticity contact, because it neglects the ability of plastically deformed asperities to resist additional tangential loading. This problem was resolved by Kogut at al. (KE friction model) [80, 162], where model improved the CEB static friction model by accounting for the resistance to sliding of plastically deformed asperities. The general trend between friction coefficient and applied load predicted by KE model is similar as experimental values;

however, their actual values are different from each other as shown in figure 4.22. The difference between experimental and theoretical friction coefficient by KE model for DLC sample is higher than the one for silica and this difference increases with surface roughness. This observation is seen for all samples and with all probes.

From the figure 4.22, the KE friction exponentially decreases similar as experimental in certain range of load and the KE friction is higher than the experimental values of silica sample, but the KE friction is lower than the experimental after certain range of load, and eventually KE friction becomes negative. The negative KE friction coefficients are also seen for aluminums sample. According to the model, the friction force is maximum at about P^* = 10 and then decreases to zero when P^* reaches 14 and hence friction coefficient will be zero after P^* = 14 and beyond that the KE friction becomes negative. This model is assumed that the contact area, the interference, and the contact pressure distribution due to the normal preload (under slip condition) remain constant during the additional tangential loading. A limiting normal preload, of about 14 times the critical load for yielding inception has been found, above which the contact cannot bear any additional tangential load.

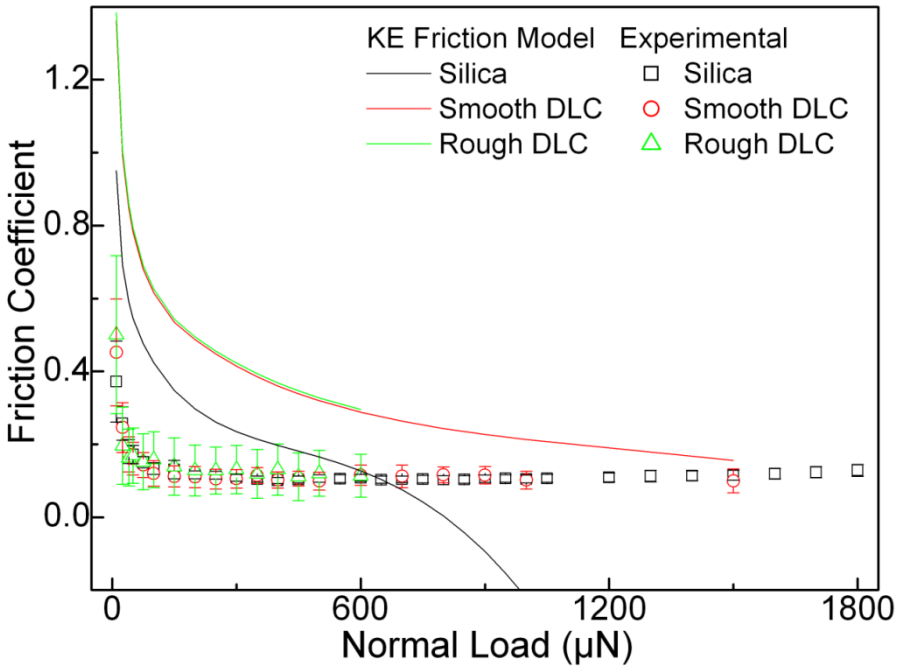

Figure 4.22: Comparision of the friction coefficient between theoritical (KE model) and experimenatal results for fused silica, and DLCs samples derived with 1 μm indenter. These results are obtained using Nanoindenter.

An another friction model for elastic-plastic spherical contact under combined normal and tangential loading in full stick given by Brizmer et al. (BKE friction model) [81] is used to calculate theoretical friction coefficient. In this model the sliding inception is associated with a loss of the tangential stiffness of the loaded asperity. The general trend between the applied normal load and friction using the BKE model is found very much similar as experimentally produced ones in low as well as medium level of micro Newton load range as shown in figure 4.23. The experimental friction coefficient decreases sharply with increasing normal load in low level of applied load. Friction coefficient attains plateau (validating the Coulomb's friction law at such high dimensionless loads) in medium level of applied load and remains constant (much smaller than by BKE model) with further increasing load. At high normal load, it starts increasing on increasing the load, which is not the case of the BKE model. This observation is seen for all samples and with all probes.

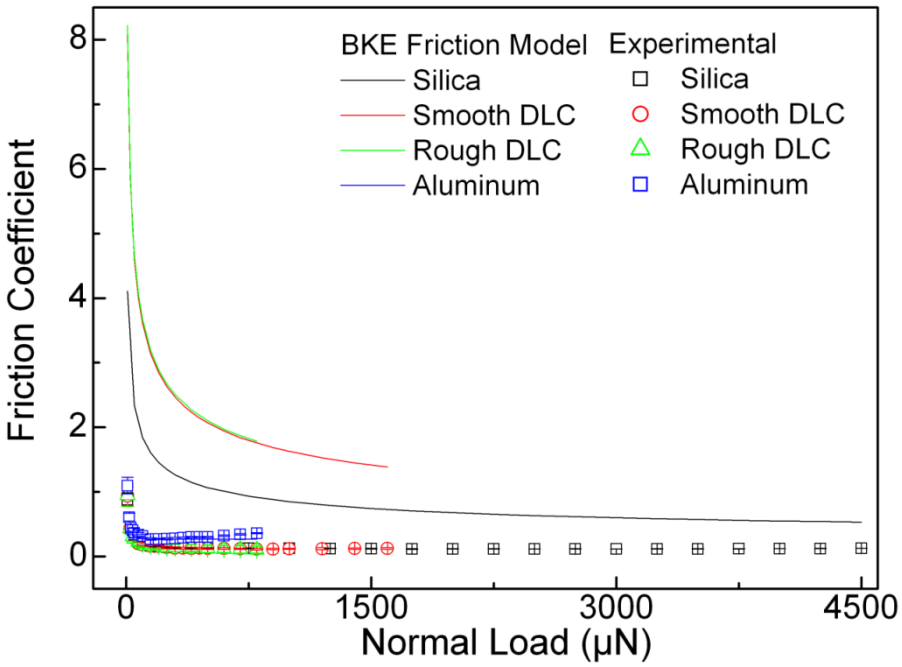

Figure 4.23: Comparision of the friction coefficient between theoritical (BKE model) and experimenatal results for fused silica, aluminum, and DLCs samples derived with 20 μm indenter. These results are obtained using Nanoindenter.

The experimentally measured friction coefficient decreases sharply with increasing normal load $P^* < 10$ and $P^* < 1$ using 1 and 20 μm indenter, respectively. The decreasing friction coefficient load regime ($P^* < 20$) predicted by BKE model differs from the one which experimentally produced. This difference increases with roughness; however, the model prediction holds true ($P^* < 20$). The experimentally produced friction coefficient attains a

plateau at earlier than the one ($P^* = 50$) predicted by BKE model. According to BKE model, at higher normal loads ($P^* > 50$), where the friction force nearly proportional to, the rate of decrease of the friction coefficient diminishes, and at $P^* = 200$ the friction coefficient approaches a constant value. Experimentally these events are observed at different normal load. The critical load, at which friction coefficient stops to decrease with normal load, decreases with increasing the roughness. These experimentally produced critical load ranges are not only different from the BKE model; it is also observed that the experimental observation for aluminum sample is substantially different at medium and high load from the one described in the model of BKE using diamond indenters; however, the asymptotes of experimental results are about 0.27 as per theoretical prediction (see figure 4.23). For other samples (silica, and DLCs) the theoretical values are always higher than the experimental results at entire range of the load. The difference between theoretical BKE and experimental results is much high at nN load range than the one at μN load range. This difference decreases with normal load and increases with surface roughness. In other words, asymptotes defined by the BKE model and experimentally produced are entirely different. These contradictory results are due to low ratio of E/Y_0 of silica and DLC sample of order of 23. The BKE model is comparable for aluminum sample because of its high ratio of E/Y_0 of about 500. This model is formed in account for contacting bodies, those have high ratio of E/Y_0 of about 1000 such as copper ball in contact with a hard sapphire flat. Another reason may be due to practically treated rough surface, whereas this model assumes very atomically smooth surface. Therefore this model has its own limitations. The actual level of the static friction coefficient in this elastic regime of deformation seems to depend on the sphere material, its diameter, and surface roughness or plasticity index. Cohen et al. [83, 84], therefore, developed a theoretical model for elastic-plastic spherical contact with real rough surfaces. The theoretical CKE friction coefficient is calculated for silica, aluminum, and DLCs samples. The CKE model shows improved results than BKE model for both DLCs samples but it fails to produce improved results for silica sample, which shows the $\psi < 0.6$. Therefore, it needs further improvement as well as this finding is limited to $\psi > 0.6$ and $\psi < 8$ and this investigation extends for rough surfaces with a high plasticity index by Li et al. [85].

The theoretical friction coefficient proposed by Li et al. is calculated for silica, aluminum, and DLCs samples and corresponding results have been plotted in figure 4.24. In low and medium level of μN load range, the general trend between the applied normal load and friction by Li et al. is found very much similar with the present experimental results. In this load range

experimental observation for aluminum sample is mostly different from the one described in Li et al. but the asymptotes of experimental results are very close to the Li et al. findings. For other samples (silica, and DLCs) the theoretical values are always higher than the experimental results at entire range of the load. The difference between experimental and theoretical values decreases with surface roughness. This observation is found with both 1 µm and 20 µm indenters. The Li at el. finding shows improved results over BKE model for both DLCs samples, and the prediction Li et al. shows improvement as compare to BKE and CKE models.

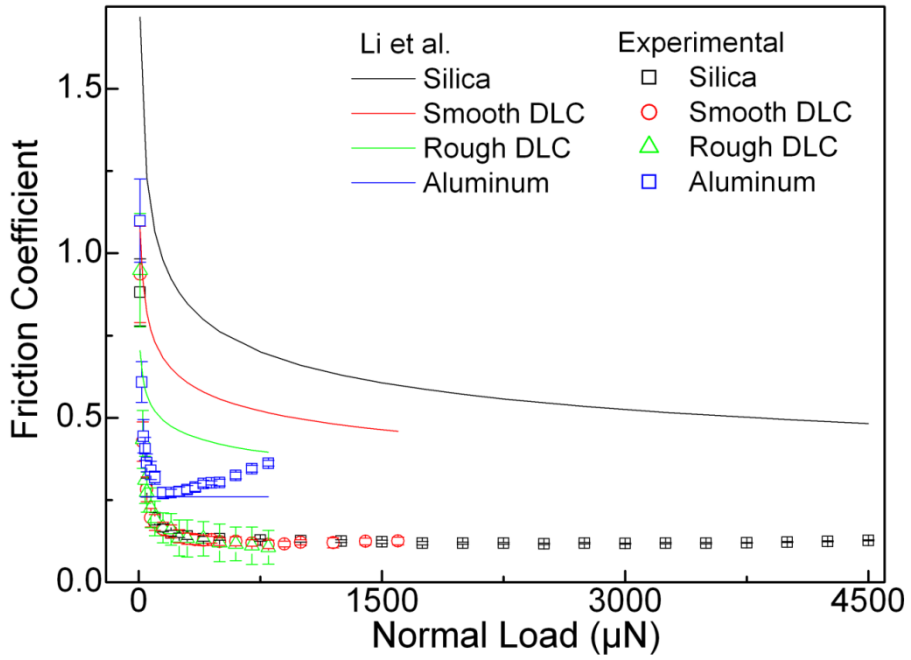

Figure 4.24: Comparision of the friction coefficient between theoritical (Li et al.) and experimenatal results for fused silica, aluminum, and DLCs samples derived with 20 µm indenter. These results are obtained using Nanoindenter.

The critical load ranges decreases with surface roughness. For silica sample, the critical load ranges for transition from purely elastic to elastic-plastic contact regime at around 200 and 400 µN with 1 and 20 µm indenter, respectively and critical boundaries for transition from elastic-plastic to predominately plastic contact regime are at around 1000 and 3000 µN with 1 and 20 µm indenter, respectively. For smooth DLC sample, the critical load ranges from purely elastic to elastic-plastic contact regime at around 200 and 400 µN with 1 and 20 µm indenter, respectively. Immediately after these transitions, the friction coefficient arrives at plateau and remains constant on further increasing normal load. It is observed that at very high level of applied load and for such rough surface lateral force or friction coefficient is

mainly due to stick slip phenomena and hence it could contain high error-bar. The predominately plastic contact regime will be somewhere after 200 and 400 µN with 1 and 20 µm indenter, respectively. For the rough DLC sample there is no reasonable identified load regime featuring a predominantly elastic contact, no transition is observed, and a predominantly plastic contact is established already at lower load than 200 and 400 µN with 1 and 20 µm indenter, respectively.

The experimental critical load values are compared with the prediction made by Flores et al. [93]. The FEM based work presented by Flores et al. [93] provides critical loads for a predominantly elastic (nondimensional normal load, $\sqrt{P/R^2\sigma_y} < 5\varepsilon_y$) and predominantly plastic contact (nondimensional normal load, $\sqrt{P/R^2\sigma_y} > 15\varepsilon_y$). These critical values for all four samples are calculated. The results are tabulated in table 4.15. Although, it is experimentally verified the general trend of the friction coefficient with increasing normal load, i.e. initial decreasing friction coefficient, followed by a constant and subsequently linear increasing friction coefficient after exceeding a critical normal load range. The most striking point in this context is a significant nondimensional load ($\sqrt{P/R^2\sigma_y}$) boundaries difference between the absolute values of the calculated and the one which experimentally found. For aluminum sample, the theoretical predominately elastic contact regime ends at 0.01 of $\sqrt{P/R^2\sigma_y}$ and predominately plastic contact regime starts from 0.03 of $\sqrt{P/R^2\sigma_y}$. However experimentally these limits are indenter size dependent and predominately elastic contact regime are observed till 0.64 and 0.19 of $\sqrt{P/R^2\sigma_y}$ for 1 and 20 µm indenter, respectively. In case of silica sample for 1 µm indenter, the experimental and theoretical have good agreement; however, predominately plastic contact regime starts at 0.22 of $\sqrt{P/R^2\sigma_y}$ for 20 µm indenter. The calculations lead to very similar boundaries for both DLC samples, whereas the experimental tests show huge differences between the two. Here the both DLC samples show predominately elastic contact regime much earlier than the one predicted by this model for 20 µm indenter. The friction coefficient remains constant at and after $15\varepsilon_y$ for 1 µm indenter and it does not follow the increasing trend after $15\varepsilon_y$. Basically, critical boundary values as $5\varepsilon_y$ and $15\varepsilon_y$ are independent of contact area and mainly depend of material properties and the finding does not consider the roughness parameter. In summary the results presented here show that till date, the existing contact models are not able to simulate the behavior of the friction coefficient. Especially the influence of sample roughness is not well understood.

Table 4.15: Critical boundaries for the fused silica, aluminum, and DLCs samples.

Sample	Theoretical		Experimental			
			1 µm indenter		20 µm indenter	
	$5\varepsilon_y$	$15\varepsilon_y$	$5\varepsilon_y$	$15\varepsilon_y$	$5\varepsilon_y$	$15\varepsilon_y$
Silica	0.34	0.71	0.37	0.82	0.08	0.22
Smooth DLC	0.21	0.65	0.24	>0.24	0.05	>0.05
Rough DLC	0.2	0.6	<0.24	--	<0.05	--
Aluminum	0.01	0.03	0.64	>0.64	0.19	>0.19

4.4.3 Mechanical properties

The mechanical properties of contacting bodies are key components in determining the friction and critical load range. The mechanical properties (hardness and elastic modulus) determine the actual contact area, surface interactions, and yield strength of plastic deformation. The friction coefficient of silica, aluminum, and smooth DLC samples is plotted against the applied normal load, while other parameters are kept constant as shown in figure 4.25. The difference in friction coefficient of silica and DLC samples is not very much clearly seen. This can be explained as per following. As mentioned earlier that at given radius of probe and other scratching conditions, the silica sample exhibits the higher contact area than DLC because of its higher interfacial energy, and friction coefficient of silica sample should be higher than DLC sample. This is applicable only when the deformation of asperities is predominantly elastic. In plastic contact load regime, the mechanical properties become key player in determining the friction values. The ratio of E/Y_0 of silica and smooth DLC sample are 22.6 and 23.7, respectively. High value of E/Y_0 means high plastic deformation and high energy dissipation loss, and friction coefficient of DLC sample should be little higher than the silica sample. Since the DLC sample is much rougher than the silica sample, friction coefficient of DLC sample should be higher than silica sample. Therefore difference in friction coefficient of silica and DLC samples is not noticed. This difference is much clear for smooth silica and aluminum sample, see in figure 4.25. This is basically due to different nature of material. Aluminum is purely metal and silica is ceramic material. The hardness of aluminum sample is about 0.47 GPa and hardness of silica is about 9.21 GPa. The pair of diamond indenter and aluminum sample provides high ratio of E/Y_0 of about 500 while ratio of E/Y_0 of silica sample is about 22.6. High of E/Y_0 means high plastic deformation and high energy dissipation loss. Therefore, the friction coefficient is higher for aluminum than the silica sample.

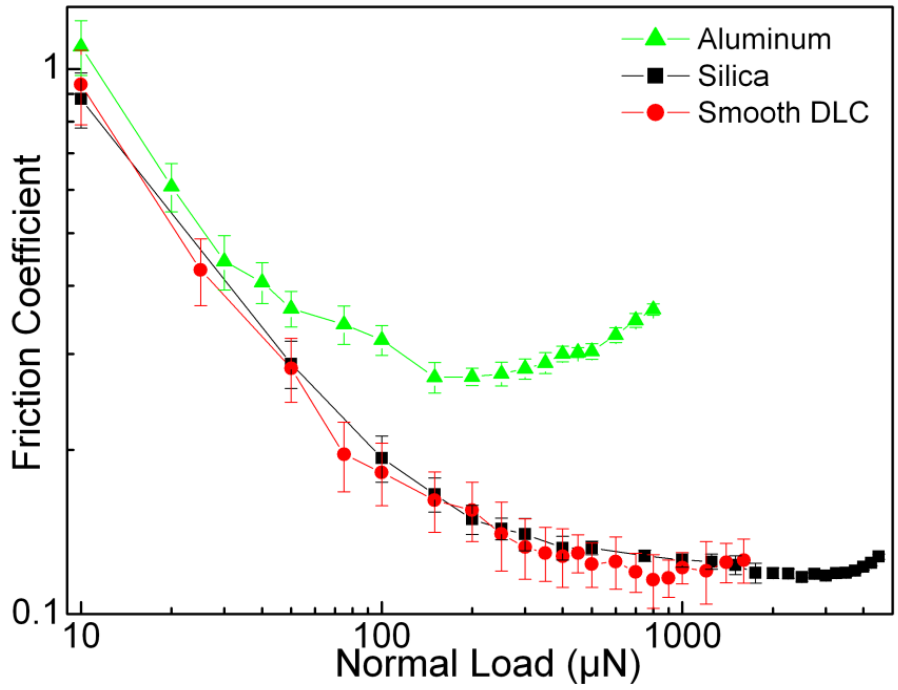

Figure 4.25: Friction coefficient vs. normal load for aluminum, silica, and DLC sample derived with 20 μm indenter.

The different critical load ranges have been observed for silica, aluminum, and DLC samples. A difference in the critical load range for DLC and silica samples can be explained by their surface roughness and material properties. A difference in the critical load range for very smooth surfaces of aluminum and silica could be explained only by their material properties. Figure 4.25 shows the critical load ranges of silica and aluminum samples for 20 μm indenter.

In order to take a closer look at the influence of material properties on the contact characteristics a non dimensional number plasticity index using material properties (E and H) is to be calculated for silica, DLCs, and aluminum samples. The simple form of plasticity index can be considered as E/Y_0. This ratio for aluminum sample is about 500 while for silica and DLC samples sample is about 23. High value of E/Y_0 implies high plastic deformation. Therefore the plastic deformation occurs at lower load for aluminum sample compared to silica and DLC samples. This comparison works for atomic level smooth surfaces but present surfaces are not perfectly smooth and possess finite roughness. Therefore a non-dimensional plastic index should be considered to include the roughness parameters. In this aspect, the first systematic attempt was made by Greenwood and Williamson (GW model) [23]. The plasticity index given by GW model is

$$\psi = \left(\frac{E^*}{H}\right)\sqrt{\sigma_s \kappa_s}. \quad (4.18)$$

According to the GW model, the predominately elastic contact is expected if $\psi < 0.6$ and for $\psi > 1$, which is the case for most rough surfaces, plastic flow will occur even at trivial nominal contact pressures. In case of the fused silica it is found to be less than unity. Whereas both DLC samples feature plasticity indices greater than unity (table 4.16). The plasticity index of aluminum sample is about 6.6. Another modified plasticity index given by the KE model [80, 162], is calculated using hardness coefficient ($K= 0.454 + 0.41\nu$).

$$\psi = \frac{2E^*}{\pi K H}\sqrt{\sigma_s \kappa_s} \quad (4.19)$$

A plasticity index of 0.4 for silica ($\nu = 0.17$), plasticity index of 7 for aluminum sample ($\nu = 0.35$), and plasticity indices of 1.4 and 1.9 for smooth and rough DLC ($\nu = 0.30$), respectively have been detected (table 4.16). According to KE model, the plasticity index is a main dimensionless parameter that defines the contact of rough surfaces. Up to $\psi = 0.6$ the contact is predominately elastic, $\psi = 1.4$ is the critical value for the transition from entirely elastic to elastic-plastic, and $\psi = 8$ is considered for the transition of the contact problem from an elastic-plastic to predominately plastic.

Table 4.16: Plasticity indices for the fused silica, DLC samples, and alumiunm sample.

Sample	Plasticity Index (GW Model)	Plasticity Index (KE Model)
Silica	0.3 ± 0.1	0.4 ± 0.1
Smooth-DLC	1.3 ± 0.1	1.4 ± 0.1
Rough-DLC	1.8 ±0.1	1.9 ± 0.2
Aluminum	6.6 ± 0.5	7.1 ± 0.6

GW and KE model estimate a predominantly elastic contact for the tests on fused silica and predominantly plastic contact for aluminum sample. GW model predicts the plastic contact deformation for both DLC samples. On the other hand KE model predicts elastic-plastic deformation and plastic contact deformation for smooth DLC and rough DLC sample, respectively. The transition load, at which plastic deformation starts, increases with plasticity index. The silica sample shows a highest elastic contact load regime and this is decreased for DLC samples. The plastic deformation starts at lowest load for aluminum sample. This observation is valid for both indenters. According to GW and KE model, deformation

between silica and indenter should be only elastic, and between indenter and aluminum sample should be plastic; however, both samples show elastic and plastic contact deformation zones at different level of applied loads. The difference between experimental results and the models could be due to simplicity of GW model and KE model. The GW model is mainly suitable for elastic contact and KE model is mainly suitable for elastic-plastic. Both models did not consider the permanent asperities deformation or plastic deformation and only valid in certain range of applied load. From the results, it can be said that the stress between indenter and sample during scratching process determines whether the contact is elastic or plastic. This local stress is a function of applying load, mechanical properties, and surface topography.

The results of scratch tests, those are carried out on SiCBN ($Si_{19}B_{21}C_{23}N_{25}$, $Si_{33}B_8C_{19}N_{27}$, and $Si_{14}B_{24}C_{29}N_{22}$) and SiCN ($Si_{36}C_{22}N_{25}$ and $Si_{40}C_{16}N_{27}$) composite films, indicate that the measured friction coefficient shows distinct behavior against the boron/silicon ratio in to the composite films (figure 4.26).

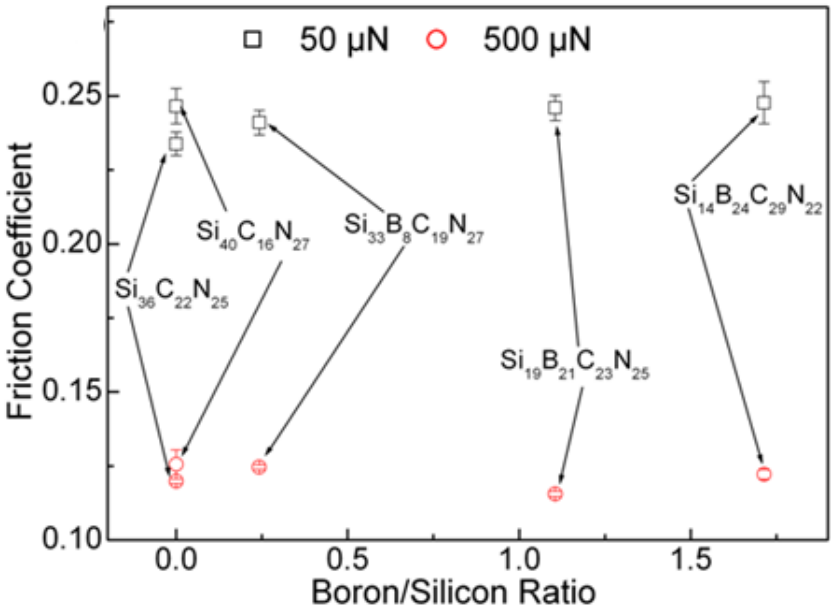

Figure 4.26: Friction coefficient of SiCN and SiCBN films.

The friction coefficient measured at 50 µN and 500 µN are about 0.25 and 0.12 for all five samples. Low coefficient of friction is correlated with low roughness of film composition and consequent tribochemical behaviour is responsible for the decreasing coefficients of friction. In SiCN films, decreasing the C-content leads to considerable decrease in coefficients of friction. However, the addition of boron to these films results in further decrease in the coefficients of friction. In order to take a look into detail, the histograms of scratch data are

plotted in figure 4.27. The histograms for SiCN films are single peaked and they are almost Gaussian fitted. The mean of histogram for $Si_{40}C_{16}N_{27}$ coating is slightly different than the one for $Si_{36}C_{22}N_{25}$ coating. This is due to presence of different amount of carbon in both coatings. The histograms of SiCBN films show two peaks. These peaks are very much clear for higher boron content film i.e. $Si_{19}B_{21}C_{23}N_{25}$ and $Si_{14}B_{24}C_{29}N_{22}$. In histogram of SiCBN films, the right hand side peak may represent component of friction due to boron content because two peak behaviors is only seen in boron contenting films, and average friction coefficient increases with increasing boron percentage in coatings. With these results, it can be said that at a given set of applied scratch conditions, the materials response to the friction can be identified and such knowledge would allow for the design of tailor made surfaces featuring defined tribological properties.

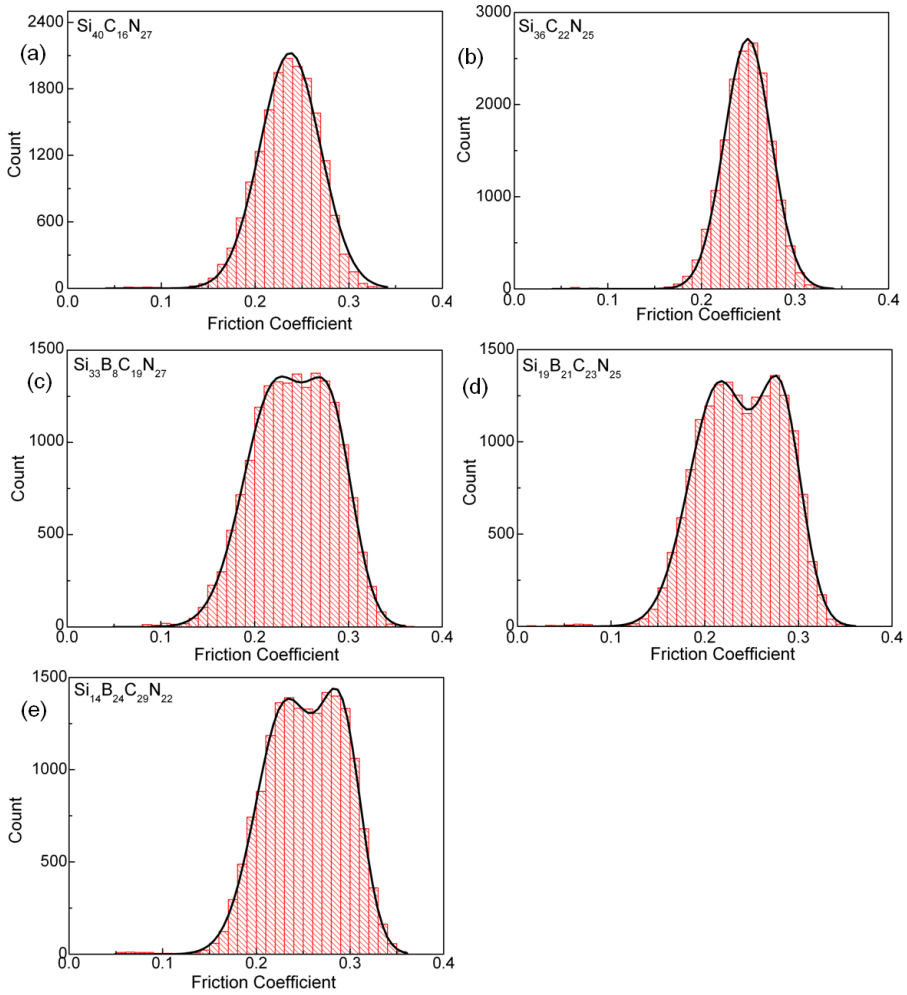

Figure 4.27: Histogram of friction coefficient data of SiCN and SiCBN films. The data are obtained from scratch test at 50 µN load derived with 20 µm indenter.

4.4.4 Adhesion force

As mentioned earlier the lateral force increases with applied load (figure 4.28) and the lateral force exists even at the zero normal load, which is additional term for the intrinsic adhesive force and/or artifact generated because of certain degree of limitation of equipment. Adhesion force consists of various attractive forces like capillary, electrostatic, van der Waals and other forces under different operating conditions. For adhering surfaces, Derjaguin proposed the following modified version of Amonton's equation

$$F_{fr} = \mu(P_0 + P) = F_0 + \mu P \qquad (4.20)$$

where a constant internal load P_0 is added with the external load to account for the intermolecular adhesive forces. The Derjaguin equation accounted for the experimental observation that there is already existence of a finite friction force F_0 at zero load or adhering surfaces.

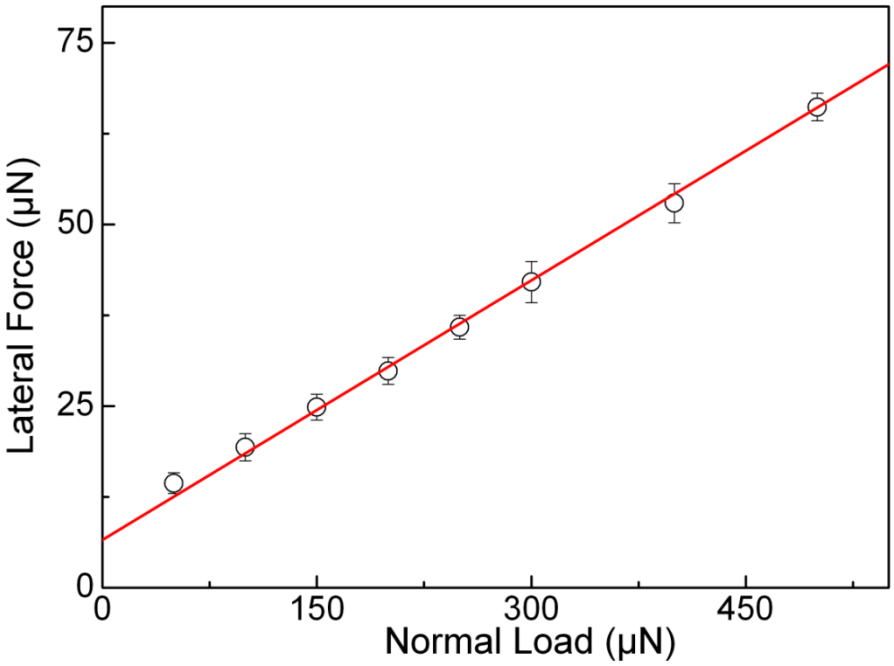

Figure 4.28: Lateral force vs. normal load for silica using 20 μm diamond indenters. These results are obtained using Nanoindenter.

The y-axis intercepts of lateral force vs. normal load for all samples and with all probes are calculated (table 4.17). The y-axis intercepts for colloidal probes are here substantially different than the one obtained from pull-off force experiment. The lateral force is complex phenomena and despite being based on physical and chemical principles as well as the huge

amount of experimental work that has been carried out, until now no complete understanding between friction and adhesion force is achieved. It can be argued that the front part of probe is only exposed to the surface while scratching, and adhesion force is only due to front part of probe. In other words, due to lateral movement of probe, the contact area is reduced and hence adhesion force is decreased. Furthermore the normal load and lateral force resolution of AFM setup also add some level of error into the lateral force data, and the y-axis intercepts may be different from the adhesion force. From AFM based results, the y-axis interacts appears lower than their actual adhesion force. The adhesion force with diamond indenters cannot be measured due to poor normal load and lateral force resolution of Nanoindenter below 10 μN load. The adhesion force between 20 μm diamond indenter and silica sample is measured using Nanoindenter with high load and lateral force resolution, and it is found to be 3 ± 2 μN, but y-axis intercept is about 7.4 μN. The y-axis intercept includes the nominal Nanoindenter lateral force resolution of about 3 μN, adhesion force of 3 ± 2 μN, and influence from artifacts. These artifacts are generated by noise level of instrument as well as surrounding and surface roughness. The same observation is seen for other samples.

Table 4.17: Y-axis intercepts of lateral force vs. normal load.

	20 μm indenter (μN)	**1 μm indenter (μN)**	**10.25 μm colloidal probe (nN)**	**2.78 μm colloidal probe (nN)**
Silica	7.4 ± 1	3.6 ± 0.6	216 ± 23	65 ± 11
Smooth DLC	7.7 ± 0.8	3.2 ± 1	77 ± 7	46 ± 19
Rough DLC	8.4 ± 1.3	3 ± 1.6	100 ± 19	67 ± 21
Aluminum	7 ± 1	3.7 ± 2	333 ± 35	21 ± 16

The true friction coefficient can be estimated by taking the slope from the plots of measured friction force vs. the applied normal load and that would eliminate the contribution of the adhesive force [163] and Nanoindenter instrumental artifacts (figure 3.18). Therefore, ramping load scratching or linear increasing scratching approach for various normal load segments has been applied. A continuous analysis of a scratch with a single scratch of increasing normal load can also be applied instead of segmental approach for various range of linear increasing normal load. In principle, there would not be a difference in both approaches. If segment size of linear increasing load is same in both approaches, it is very obvious that both would generate the same lateral force, and hence friction coefficient will be the same. However, their scratch test parameters are not same, and hence will generate different friction values. For example, for a continuous analysis of single scratch with

increasing normal load, initial segment size (ΔP) is 1000 µN for 10 sec and 10 µm (ΔP = 1000 µN, dP/dt = 100 and dx/dt = 1), and in segmental approach, the segment size (ΔP) is100 µN for 10 sec and 10 µm (dP/dt = 10 and dx/dt = 1). In order to compare both cases continuous scratching has to be divided in to 10 segments. Eventually, the segment size will be same at the end in both cases, however loading conditions (dP/dt = 100) remain high in first case, which provides the difference in values. While fixing loading conditions (dP/dt) same in both cases, one has to adjust the indenter lateral movement (dx/dt), which is, however, difficult in first case to scratch at large length with existing Nanoindenter setup. Therefore the segment-approach is more convenient for studying the effect of influencing parameter. Once the normal load range and scratch segment size are established (detail in chapter 3), the slope of a linear trend line fit to each segment is taken as the segments friction coefficient at a normal load equal to the segments centre. The corresponding results for the silica sample are plotted in figure 4.29.

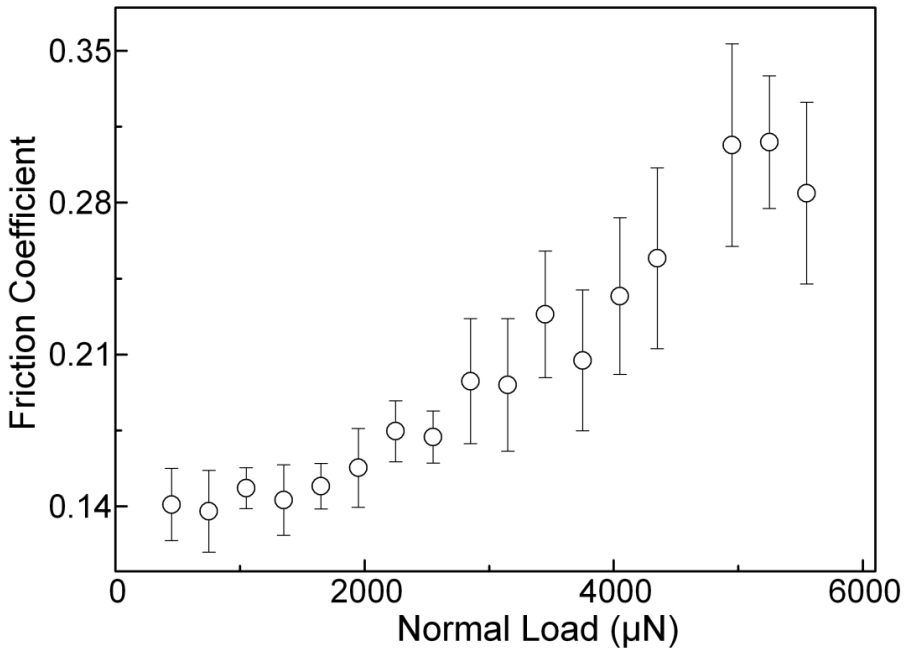

Figure 4.29: Friction coefficient vs. normal load for the silica sample derived with 20 µm indenter.

Here friction coefficient does not follow the decreasing trend due to adhesion component of friction because by defining the friction coefficient, the adhesion component is eliminated. The friction coefficient follows only constant to increasing trend in the provided Nanoindenter load regime. A decreasing friction coefficient from slope approach can also be seen, if applied load range is lower than provided load range of Nanoindenter. Constant

friction coefficient at low level of applied load and increasing friction coefficient at high level of applied load can be explained by following equation

$$\mu = \mu_0 + k_2 P^{1/2}. \quad (4.21)$$

The general trend of a transition from a predominantly elastic contact regime featuring a low constant friction coefficient to a predominantly plastic contact characterized by an increasing friction coefficient with increasing load can be considered, and this transition is considered as a critical load range for a transition from elastic contact to plastic contact regime. It is observed that the critical load range increases with the radius of indenter due to increasing the contact area, see figure 4.30.

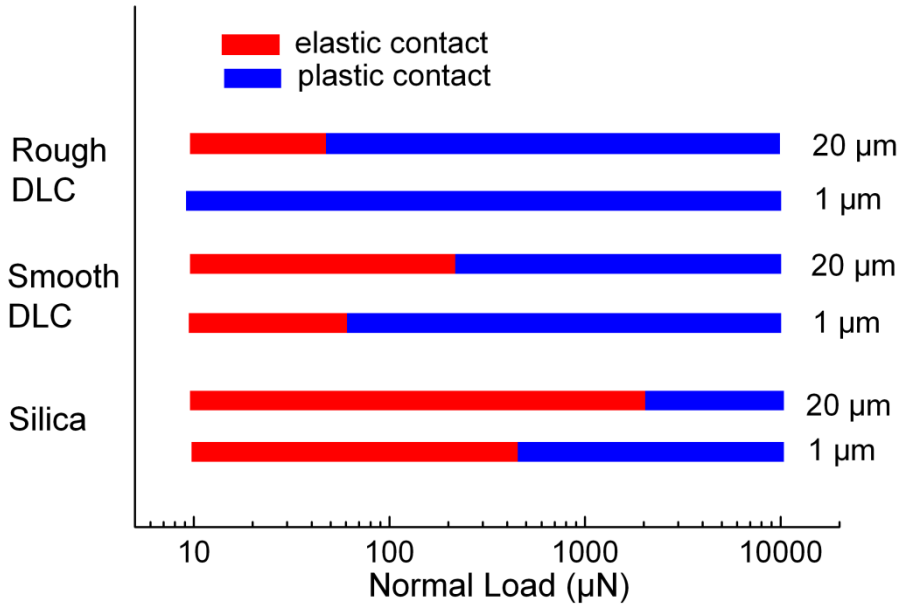

Figure 4.30: Critical load values for silica and DLCs samples derived with 1 and 20 µm indenters.

The critical load range for silica sample using 1 µm indenter is found to be 400-500 µN whereas it is 1800-2100 µN for 20 µm indenter. For smooth DLC samples, the critical load range increases from 50-70 to 200-250 µN with using 1 to 20 µm indenter. For rough DLC, only plastic deformation contact regime is observed for 1 µm indenter, but a transition at 50 µN load is seen for 20 µm indenter.

The friction coefficients also show the distinct difference on surface roughness. At a given load and probe, the friction coefficient increases with surface roughness. On increasing roughness the yield of plastic deformation of asperities occurs at earlier load, and friction

coefficient increases. With 20 µm indenter, the critical load range of silica, smooth DLC, and rough DLC samples is found at 1800-2100, 200-250, and 50 µN, respectively, as shown in figure 4.31. The same observation is noticed for 1 µm indenter.

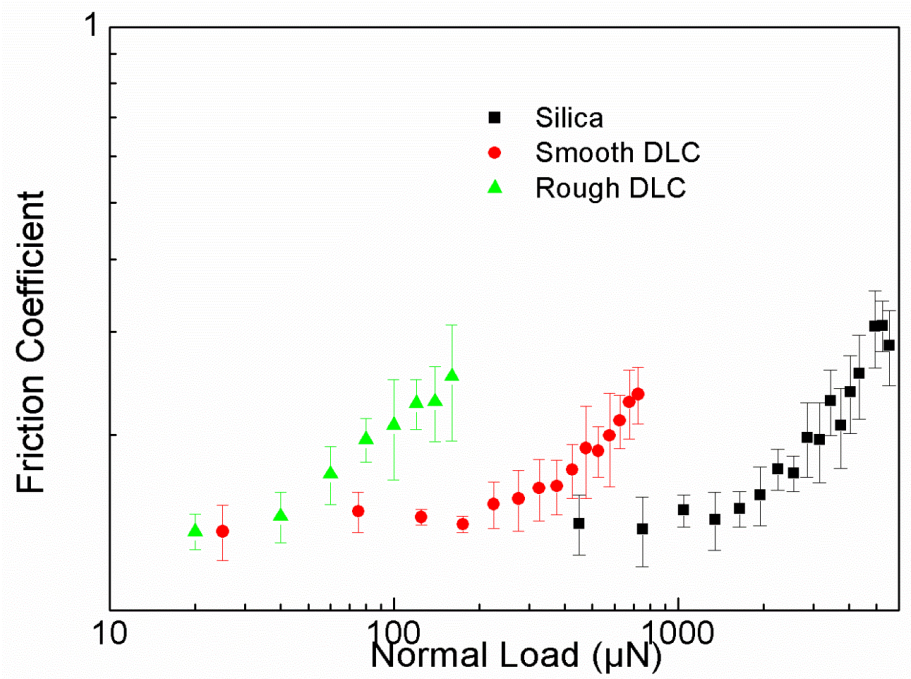

Figure 4.31: Friction coefficient vs. normal load at logarithmic scale for silica and DLCs samples using 20 µm indenter.

Silica sample is very smooth and constant friction coefficient load range is also found to be largest. Constant friction coefficient load range decreases with surface roughness. The increasing friction coefficient load range is found at lower load for rough DLC sample than the one for smooth silica sample. The deformation of asperities is higher for rough surfaces at particular scratch condition and the permanent deformation of asperities is observed at lower load for rough surface. Since the increasing friction coefficient load regime represents the plastic contact deformation regime, this load regime is observed earlier for rough DLC surfaces.

The experimental critical load values are compared with the prediction made by Flores et al. [13]. The critical values for all three samples and both indenters are tabulated in table 4.18. Although, the general trend of the friction coefficient with increasing normal load is experimentally verified, i.e. initial constant low value followed by a linear increasing friction coefficient after exceeding a critical normal load range, the absolute values of the calculated and experimentally found load boundaries differ significantly (table 4.18). In case of silica

sample, the theoretical predominately elastic contact regime ends at 0.24 of $\sqrt{P/R^2\sigma_y}$ and predominately plastic contact regime starts from 0.71 of $\sqrt{P/R^2\sigma_y}$. The experimental critical values for transition from elastic to plastic contact regime for silica sample using 1 µm indenter is 0.516-0.58 of $\sqrt{P/R^2\sigma_y}$. Thus experimental critical values satisfy the model for 1 µm indenter; however, plastic deformation with 20 µm indenter starts at 0.17-0.18 of $\sqrt{P/R^2\sigma_y}$, little earlier than the theoretical elastic limit. The most striking differences in this context are the load boundaries in case of the smooth and rough DLC samples. The calculations lead to very similar boundaries for both DLC samples, whereas the experimental tests show huge differences between the two. Here, the plastic deformation for smooth DLC sample with 1 µm indenter starts little earlier than the theoretical values, while it arrives much earlier than the theoretical value with 20 µm indenter. The rough DLC sample on the other hand features no such regime in the normal load range (only small normal load range with 20 µm indenter).

Table 4.18: Critical values for silica and both DLCs samples.

Sample	**Theoretical**		**Experimental**	
			1 µm indenter	**20 µm indenter**
	$5\varepsilon_y$	**$15\varepsilon_y$**	**Critical value**	**Critical value**
Silica	0.24	0.71	0.5-0.6	0.17-0.18
Smooth DLC	0.21	0.62	0.12-0.14	0.03-0.04
Rough DLC	0.20	0.60	--	0.02

4.4.5 Loading rate

The loading rate (dP/dt) for ramping load scratch test is defined as ratio of the magnitude of ramping load (ΔP) to time interval (Δt). In order to understand the loading rate effect on the friction, the lateral force vs. normal load curves for different loading rates are plotted (figure 4.32). In figure 4.32, the loading rate varies from 6 to 18 µN/sec. This plot is obtaining with 20 µm indenter, 100 µN as the center of all applying loads, and 1 µm/sec scratching speed. The slope of lateral force vs. normal load curve is increased with decreasing the loading rate as shown in figure 4.32. The friction coefficient is calculated as slope of above lateral force vs. normal load curve and these friction coefficients are plotted against the loading rate in figure 4.33 (b). The friction coefficient of silica decreases with increasing the loading rate. This observation is also seen for all indenters, scratching speeds, and normal loads, as shown in figure 4.33.

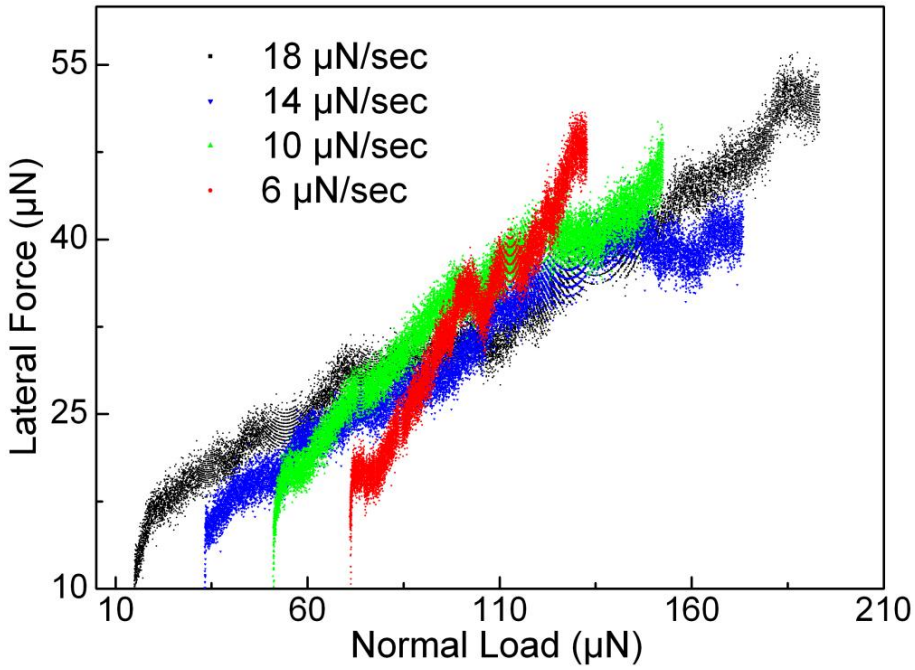

Figure 4.32: Lateral force vs. normal load for the silica sample derived with 20 μm indenter. The scratching length and time are 10 μm and 10 sec at 100 μN load.

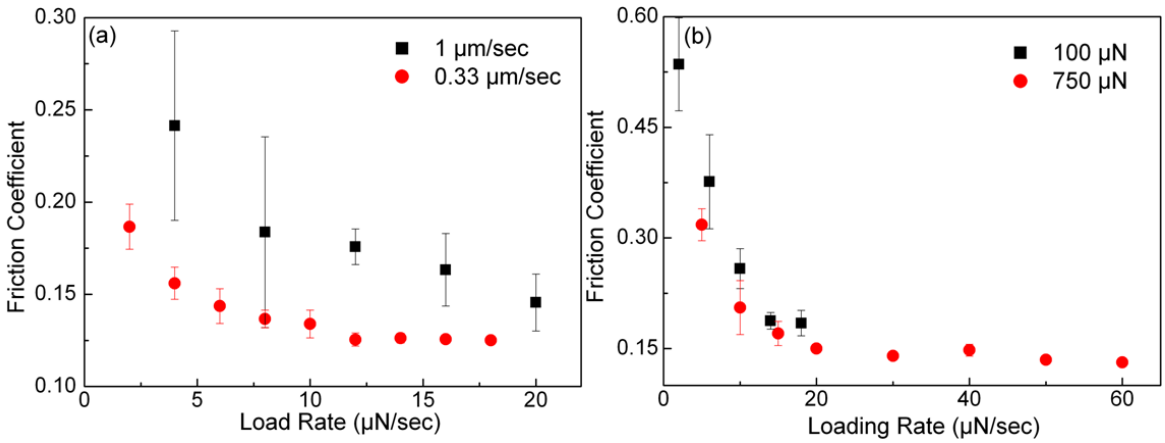

Figure 4.33: Friction coefficient vs. loading rate. (a) R = 1μm, dx/dt = 0.33 and 1 μm/sec, and P = 100 μN. (b) R = 20 μm, dx/dt = 1 μm/sec, and P = 100 and 750 μN.

In order to understand the detailed behavior, the normal displacement as a function of normal load is plotted (figure 4.34). The parameters are a constant tip lateral displacement speed (dx/dt = 1 μm/sec) and different values of the loading rate (dP/dt = 30, 40 μN/sec). These scratches are performed with 1 μm indenter on silica sample within fully elastic contact load regime (10-400 μN). From figure 4.34, two different curves corresponding to two different

ramping normal loads are obtained. The normal displacement of indenter decreases with increasing loading rate. The same observation is also found by Labdi et al. [95]. The higher normal displacement of the indenter means higher lateral force, thereby, increasing the friction coefficient. This observation is independent of applied load regime, size of the indenter, roughness of surface, and other parameters.

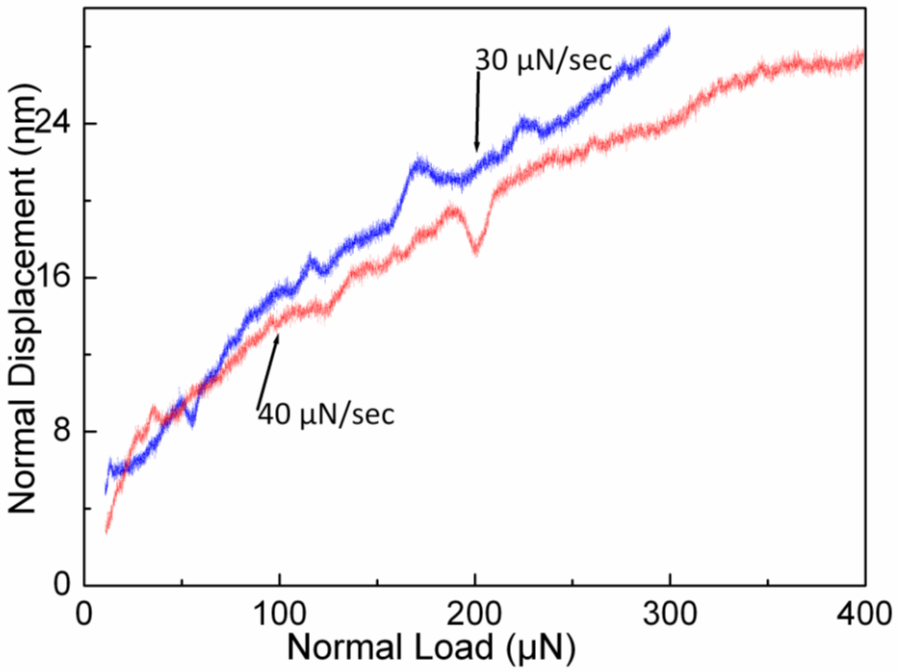

Figure 4.34: Normal displacement vs. normal load for 30 and 40 µN/sec loading rate (R = 1µm, dx/dt = 1 µm/sec).

It is also observed that the critical load for a transition from constant friction coefficient to increasing friction coefficient changes with changing the loading rate by fixing above parameter constant (R = 1µm, dx/dt = 0.33 µm/sec) as shown in the figure 4.35. The friction coefficient is found to be higher at 1 µN/sec loading rate than the one at 3.33 µN/sec loading rate. The difference of friction coefficients at both loading rates is almost constant in elastic contact load regime and this difference is increased with load in plastic contact load regime. The difference in normal displacement of 3.33 and 1 µN/sec scratching is also constant in elastic contact load regime and this difference increases with load in plastic contact load regime. The transition from elastic to plastic contact regime is slightly higher at lower loading rate but with clear transition. On the other hand the transition at higher loading rate the transition is slightly lower with unclear transition, as shown in figure 4.35. The stress between indenter and sample during scratching process can be a function of applying loading rate as

loading rate determines normal displacement of indenter. This stress field determines the contact regime between indenter and sample.

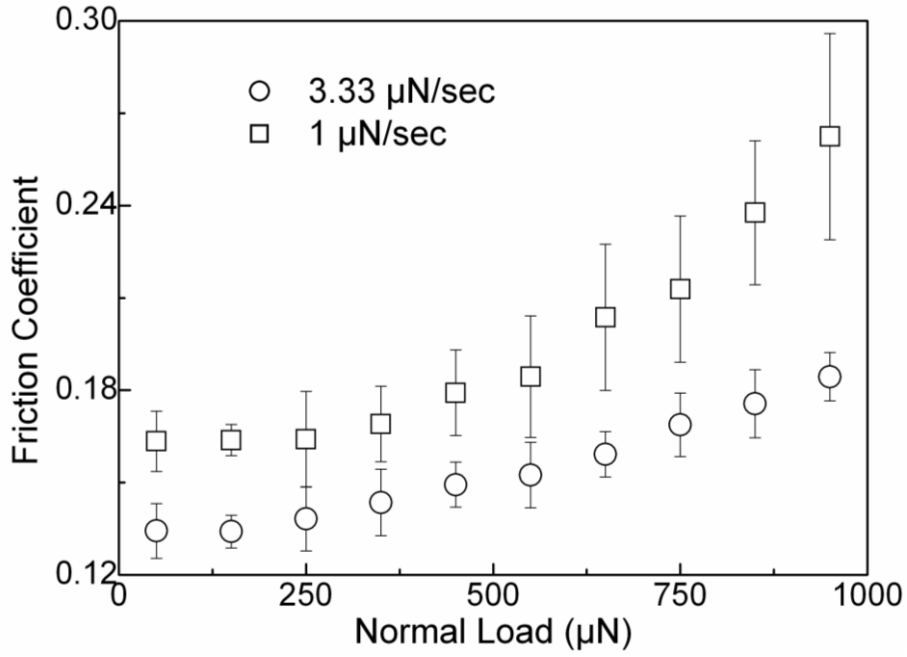

Figure 4.35: Friction coefficient vs. normal load curve for silica at 1 and 3.33 μN/sec loading rate (R = 1μm, dx/dt = 0.33 μm/sec).

4.4.6 Scratching speed

The scratching speed (dx/dt) is defined as the ratio of lateral displacement (Δx) of tip during scratching to time duration of scratch (Δt), and it can vary with either changing the lateral displacement of tip or time interval of scratch. The scratching speed for constant load scratching varies with scratching time and it varies with lateral displacements for ramping load scratch tests. The tests of constant load scratching on silica and aluminum sample with 0.33 and 1 μm/sec and ramping load scratching on silica sample with 0.066 to 0.33 μm/sec scratching speed are performed. The scratch tests with varying scratching speed are mainly carried out on the smooth samples (silica and aluminum). Other rough DLC samples are not used to avoid any confusion because rough sample can have additional error due their surface roughness. Figure 4.36 depicts the friction coefficient vs. normal load with 0.33 and 1 μm/sec scratching speed. The normal load is constant for these scratch tests and scratch length is 10 μm. The friction coefficient is found higher at higher scratching speed. This behavior is also found for both silica and aluminum samples as well as for both indenters.

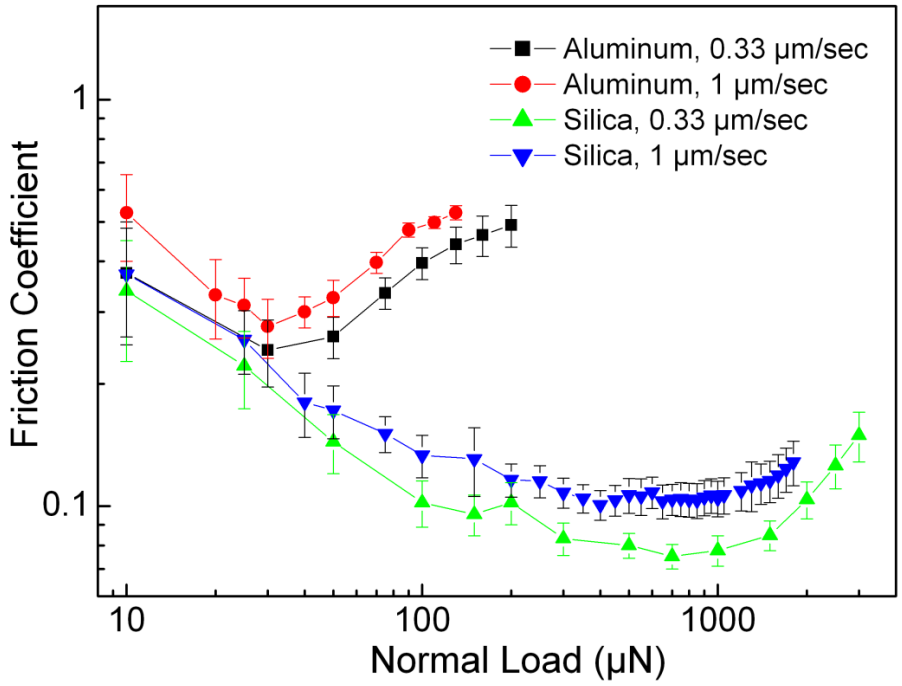

Figure 4.36: Friction coefficient vs. normal load. Scratch tests were performed at constant normal load with 1 µm indenter.

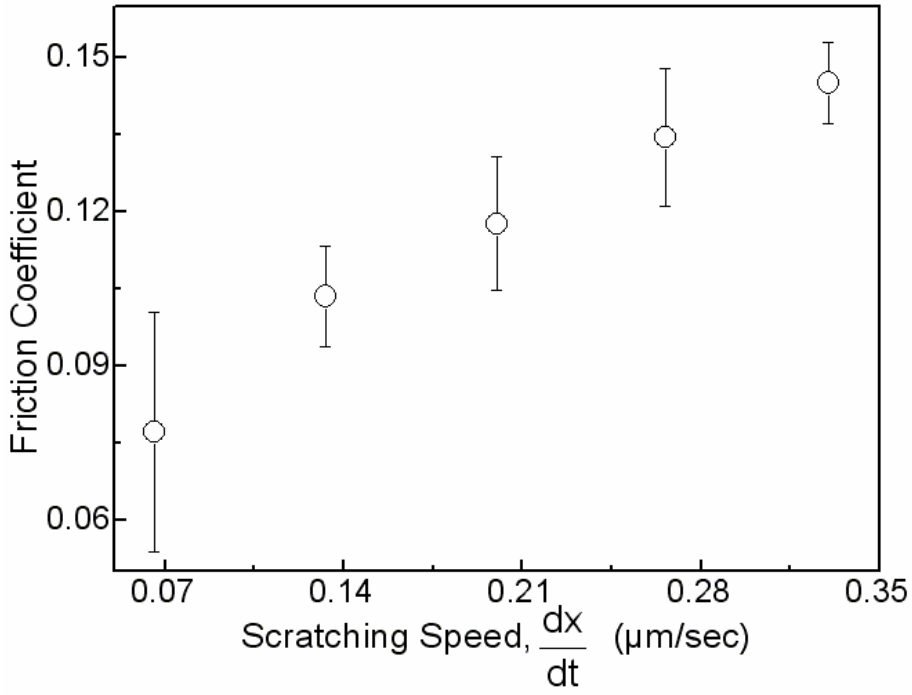

Figure 4.37: Friction coefficient vs. scratching speed. Scratching is at ramping load (R = 1µm, dP/dt = 3.33 µN/sec, and P =100 µN).

The figure 4.37 shows the friction coefficient of silica against the scratching speed for ramping load scratching. The scratching speed (0.066 to 0.33 µm/sec) is varied by changing

the scratching length from 2 μm to 10 μm and fixing other parameters at constant values (R = 1μm, dP/dt = 3.33 μN/sec, and P =100 μN). The friction coefficient is calculated by measuring the slope from the plots of measured friction force versus the applied normal load. Te friction coefficient increases with increasing scratching speed.

In literature several studies have been done in order to know the scratching speed effect on friction. Several findings such as Labdi et al. [95] stated that friction is independent of scratching speed. Several other findings stated that scratching speed affects the wear rate and friction. For example, Wong et al. [96] reported that wear rate increases with sliding speed due to the structural changes caused by in-situ adiabatic heating during sliding. Hodge at el. [99] found that the scratch velocity exerts little effect on the wear behavior and the scratching speed is having little effect on the friction coefficient. Huang et al. [100] found that scratch velocity has little effect on the scratch depth, and Gossilloud et al. [101] found that the applied load and the scratching velocity strongly influence the deformation mechanism. Briscoe et al. [102] proposed a relation between decompression rate and scratch velocity as

$$\dot{\sigma}_s \approx \frac{2vP_m}{b} \tag{4.22}$$

where P_m is the mean contact pressure under the indenter and b is scratch width. It is experimentally noticed that the normal displacement of the indenter does not change with variation of scratching speed; therefore, width of scratching (b) will not change. For constant scratching width, the decompression rate will be proportional to scratch speed ($\dot{\sigma}_s$ α v) and decompression will increase with scratch speed, and hence scratching speed will influence on tribological contact. At high scratching speed due to the high decompression rate, the silica and aluminum sample will plastically deform earlier, and they will show higher friction coefficient, which is in fact observed experimentally (figure 4.36 and 4.37). It is also observed that the critical load range for transition from elastic to plastic contact regime is lower for scratching at higher speed. It means that the plastic deformation at higher scratching speed starts comparatively at lower load (figure 4.36). The stress between indenter and sample during scratching process can be a function of scratching speed as it determines decompression rate. This stress value determines the contact regime between indenter and sample.

Chapter 5 Conclusions and Future aspect

5.1 Conclusions

The tribological contact phenomenon on the nanoscale by means of scanning probe techniques is studied. The AFM and Nanoindentation based tribological tests on the surfaces featuring different roughness values (fused silica, silicon, DLC, aluminum, Si-C-B-N-O coatings) are carried out. The constant load as well as ramping load scratch tests in the load range of nN-mN are performed. The radius of probes (diamond and silica) and experimental operating parameters (loading rate and scratching speed) are varied in these experiments. Aside from the tribological tests, results of adhesion force (pull-off force) between adhering particles (colloidal probes) and rough surfaces (silicon and DLC) are discussed. In this thesis, effect of surface roughness, mechanical properties, adhesion force, and external parameters (applying normal load, scratching speed, and loading rate) on friction is identified and comparative studies with exiting models are done. Based on the experimental results and analyses of results, following conclusion may be drawn:

(1) Adhesion force linearly increases with size of adhering particle for smooth surfaces. This correlation can be described by the JRK model. The theoretical JKR adhesion force is higher than the experimental results due to exclusion of roughness factor in deriving the JKR model. The normalized adhesion force decreases with increasing roughness up to 0.0025 of rms/R and can be described by the Rabinovich model. At values higher than 0.0025 of rms/R, the normalized adhesion force is found to be increasing with surface roughness. Later case is usually observed for the particles smaller than or similar in size to the asperities, and the contact area increases due to the interaction of adhering particles with valley portion of asperities. On the basis of Rabinovich model, an equation for estimating adhesion that takes into account the interaction of adhering particle with valley portion of asperities is developed. A good correlation is found between theoretical and experimental results.

(2) In fully elastic contact load regime smooth surfaces, the deformation of the asperities is reversible or non-permanent and a decreasing friction coefficient is noticed at low level of applied load. In this load regime, friction coefficient follows the elastic Hertz contact theory ($\mu \propto (P)^{-1/3}$). The asperities start to deform plastically in higher load regime beyond the elastic contact load regime and the friction coefficient is found to be constant (Coulomb's law). In fully plastic contact load regime, the asperities deform permanently and an increase

in friction coefficient is seen load as per the relationship $\mu \propto (P)^{-1/2}$. In other words, at low loads a Hertzian contact behavior along with transition regime between elastic and plastic contact is observed, followed by a plastic deformation dominated normal load regime.

(3) At low level of applied load, wherein contact is elastic, the friction coefficient increases with radius of probe due to increasing the contact area with the probe size. In contrast at high level of applied load, wherein contact is predominantly plastic, the friction coefficient decreases with size of probes. This can be explained by contribution of plowing and the plowing component of friction force has a direct, but inverse relation with the radius of the probe. The critical load range for a transition from either predominantly elastic to elastic-plastic contact regime, from elastic-plastic to predominantly plastic contact regime, or predominantly elastic to predominantly plastic contact regime increases with radius of probe.

(4) At given applied load and probe size, the deformation of asperities increases on increasing the roughness of surface and friction coefficient increases. For rough surface and in elastic contact load regime, measured friction coefficient decreases with normal load as per $\mu \propto P^{-m}$. The results are compared with predictions by theoretical static KE, BKE, and CKE friction models, and friction model by Li et al.. General trend between the applied normal load and friction using these models is found very much similar with the experimental results. KE model is suitable only in certain range of applied load and beyond critical load, the predicting KE friction coefficient value will be negative because the contact cannot bear any additional tangential load above critical load. The BKE model is only suitable for samples those have very high E/Y_0 and this model also fails for rough samples due to non-consideration of surface roughness. The CKE model includes the roughness parameters in predicting friction coefficient values and shows the improved results than the BKE model for rough samples but this model is only limited when $\psi > 0.6$ and $\psi < 8$. However, Li et al. improved the prediction made by other models, but it cannot predict the actual end value of the friction coefficient for a realistic surface.

The critical load values decrease with surface roughness. The load boundaries predicted by Flores el al. significantly overestimate the ones that are experimentally found. In addition, that finding fails to reproduce the significant differences between the two same surfaces featuring different roughness. The results presented in this thesis show that till date the existing contact models are not able to simulate the contact behavior of the friction coefficient. Especially the influence of sample roughness is not well understood.

(5) The mechanical properties (hardness and elastic modulus) of contacting bodies have significant influence on the friction and critical load values as they determine the yield of plastic deformation, the actual contact area, and surface interactions. For smooth surfaces, high value of E/H means high degree of plastic deformation and high energy dissipation loss. For rough surfaces, the results are compared with predictions by the GW as well as the KE model. In both cases the models estimate a predominantly elastic contact for the tests on silica and predominantly plastic contact for DLCs and aluminum samples. This could not be verified by experiments as these samples show a transition from predominantly elastic to plastic contact.

(6) In elastic contact load regime and at low level of applied load, the role of surface force or adhesion force is important. Due to intrinsic adhesive force, the lateral force exists even at the zero normal loads. The true friction coefficient can be segmental calculated as slope of a linear fit to the lateral force vs. normal load. At a sufficiently low level of applied normal load, wherein the contact is elastic, the friction coefficient is constant. Here decreasing friction coefficient is not observed due to eliminating the adhesive term. However, at increased normal loads the contact involves plastic deformation and the friction coefficient increases with increasing normal load.

(7) The external parameters (scratch speed and loading rate) influence the tribological properties as they change the stress field. The friction coefficient increases on decreasing loading rate and it can be explained with that normal displacement of probe in to the sample increases with decreasing the loading rate. The friction coefficient increases with scratching speed. It can be explained using decompression rate. At high scratching speed and due to the high decompression rate, the sample plastically deforms earlier and thus friction coefficient increases with scratching speed. The critical load for transition from elastic to plastic contact regime increases with loading rate. The scratching speed also alters the critical load range and it decreases with scratching speed.

(8) In this thesis work, a relationship between surface roughness, mechanical properties, and external parameters (normal load, loading rate, and scratching speed) on adhesion force and friction, followed by a relationship between adhesion force and friction is established. Analytically individual materials and topographical contribution to the frictional response of the system is indentified. The stress field between indenter and sample during scratching process determines whether or not the contact is elastic or plastic. This local stress is function

of applying load, mechanical properties, adhesion force, surface roughness, and external parameters.

5.2 Future aspect

Aspects pertaining to the further development with several immediate possibilities of adhesion and tribological phenomena are discussed in the following:

(1) The nature of adhesion forces between fine particles and engineering surfaces are important for a variety of natural phenomena and industrial process. Examples are applications in process control, transportation, aerospace, data storage, and many other others. In present work, the adhesion forces for particle-particle and particle-rough surface are studied. Adhesion force and roughness relation can be extended for lower and higher size of adhering silica particle. The lowest size of adhering silica particle can go up to several tens of nm in the range of commercial standard silicon nitrate AFM tips, but gluing of these particles on tipless cantilever is extremely difficult. The silicon standard tips exhibiting flat apexes can be used to glue nano size particles. The flat apex of different size can be made by eroding fresh tips against a smooth surface. The apex size can be controlled by the erosion time as well as with the variation of the normal force. The bigger silica particles (> 10 μm in radius) can glue on very stiff cantilever; however, AFM setup cannot handle this. Therefore, Nanoindenter based colloidal probe can be prepared. A creator with defined geometry can be produced on diamond Nanoindenter tip using focus ion beam (FIB) and particle can be glued on these creators by employing manipulator. These particles are in turn used as probes to sample the mechanical interaction with other particles as well as plane surface.

(2) The adhesion force between flat tip (well defined contact area) and silica particles can be a subject of study. The method of making flat tip for AFM is described above and flat tip for Nanoindenter set can produce by FIB. Interaction between flat tip and single particle as well as particle-density-gradient samples can be performed. The idea is to obtain adhesion data by eliminating contact area effects and considering particles as ideal asperities. For a surface composed of hemispherical asperities, the expression for adhesion force has been formulated as (Katainen model) [55]

$$F_{ad} = \frac{A_H A}{6H_0^2}\left[\rho r + \frac{1}{\pi H_0\left(1+\frac{y_{max}}{H_0}\right)^3}\right] \tag{5.1}$$

where A is contact area and ρ is the number density of the asperities.

(3) The adhesion and tribological experiment can perform for other materials inspite of using silica. The polymer particles such as toner can also be a part of study because they interact elastically as well as plastically even in nN load range. In this thesis, the adhering particles or probes are considered a rigid body and they don't show any elastic-plastic deformation. Deformation of asperities on probes surface along with deformation of asperities on sample surface will be an interesting subject. It would become more interesting if one can study in-situ elastic-plastic deformation of asperities on sample and probes.

(4) In the present study, the friction coefficient is a function of applied normal load, mechanical properties, probe size, loading rate, scratching speed, adhesion force, and surface roughness. The present work is tried to normalize all these factors. However adhesion force, normal load, and surface roughness parameters are not independent with each others. In future this study can be extended for various surface energy systems such that adhesion dominated term can be identified. For a given surface energy, a material system (ideally silica) can be modified with FIB technique such that only topography effect on tribological phenomena can be identified.

(5) Relation between shear stress and applied load is crucial to understand the tribological phenomena. According to the fundamental law of friction given by Bowden and Tabor [156], the friction force is directly dependent on the real area of contact, for a single asperity contact.

$$F_{fr} = \tau \cdot A \tag{5.2}$$

Real contact area (A) is function of several parameters. In the present study, the real contact area is found as a function of applied normal load, mechanical properties, probe size, loading rate, scratching speed, adhesion force, and surface roughness. Presence of these parameters, it is extremely difficult to calculate the true contact area and hence the shear stress. Therefore it could be a motivation for further study.

(6) In the present work, it is studied the suitable homogeneous model systems (e.g. materials, surface topography, tip geometry) for the response of tribological properties. The findings of this thesis can be applied to ceramic composites such as diamond/carbide nanocomposites and other film systems. The main difficulty with composite materials is to identify a difference between materials and topographical contribution to the frictional response because of

complex surface topography. It is now possible that at given set of applied scratch condition, the topographical contribution as well as materials response can be identified. Such knowledge would allow for the design of tailor made surfaces featuring defined tribological properties. Therefore it is also a motivation for further study.

References

1. B. Bhushan, *Handbook of Micro/Nano Tribology*, CRC Press, New York, 1999.
2. K. L. Johnson, *Contact mechanics*, Cambridge University Press, Cambridge Cambridgeshire ; New York, 1985.
3. X. H. Shi, and Y. P. Zhao, *Comparison of various adhesion contact theories and the influence of dimensionless load parameter*, J Adhes Sci Technol, 18 (2004) 55-68.
4. I. N. Sneddon, *The relation between load and penetration in the axisymmetric Boussinesq problem for a punch of arbitrary profile*, Int. J. Engng. Sci., 3 (1965).
5. D. Tabor, *The hardness of solids*, Review of physics in technology, 1 (1970).
6. M. F. Doerner, and W. D. Nix, *A method for interpreting the data from depth-sensing indentation instruments*, J. Mater. Res., 1 (1986).
7. W. C. Oliver, and G. M. Pharr, *An Improved Technique for determining hardness and elastic modulus using load and displacement sensing indentation experiments*, J. Mater. Res. , 7 (1992).
8. G. M. Pharr, W. C. Oliver, and F. R. Brotzen, *On the Generality of the Relationship among Contact Stiffness, Contact Area, and Elastic-Modulus during Indentation*, J Mater Res, 7 (1992) 613-617.
9. R. B. King, *Elastic Analysis of Some Punch Problems for a Layered Medium*, Int J Solids Struct, 23 (1987) 1657-1664.
10. B. Bhushan, *Handbook of Micro/Nano Tribology*, CRC Press, New York, 2003.
11. K. W. McElhaney, J. J. Vlassak, and W. D. Nix, *Determination of indenter tip geometry and indentation contact area for depth-sensing indentation experiments*, J Mater Res, 13 (1998) 1300-1306.
12. R. B. King, *Elastic analysis of some punch problems for a layered medium*, Int. J. Solids Structures, 12 (1987).
13. H. J. Gao, C. H. Chiu, and J. Lee, *Elastic Contact Versus Indentation Modeling of Multilayered Materials*, Int J Solids Struct, 29 (1992) 2471-2492.
14. H. W. Bückle, J. W.; Conard, H. , *The science of hardness testing and its applications*, American Society for Metals, Metals Park, OH, 1973.

15. B. Jonsson, and S. Hogmark, *Hardness Measurements of Thin-Films*, Thin Solid Films, 114 (1984) 257-269.
16. P. J. Burnett, and D. S. Rickerby, *The Mechanical-Properties of Wear-Resistant Coatings .1. Modeling of Hardness Behavior*, Thin Solid Films, 148 (1987) 41-50.
17. P. J. Burnett, and D. S. Rickerby, *The Mechanical-Properties of Wear-Resistant Coatings .2. Experimental Studies and Interpretation of Hardness*, Thin Solid Films, 148 (1987) 51-65.
18. A. K. Bhattacharya, and W. D. Nix, *Finite-Element Simulation of Indentation Experiments*, Int J Solids Struct, 24 (1988) 881-891.
19. T. Y. Tsui, C. A. Ross, and G. M. Pharr, *A method for making substrate-independent hardness measurements of soft metallic films on hard substrates by nanoindentation*, J Mater Res, 18 (2003) 1383-1391.
20. D. Stone, W. R. Lafontaine, P. Alexopoulos, T. W. Wu, and C. Y. Li, *An Investigation of Hardness and Adhesion of Sputter-Deposited Aluminum on Silicon by Utilizing a Continuous Indentation Test*, J Mater Res, 3 (1988) 141-147.
21. S. J. Bull, *Modelling of the mechanical and tribological properties of coatings and surface treatments*, Mat. Res. Symp. Proc. , 750 (2003).
22. J. F. Archard, *Elastic Deformation and the Laws of Friction*, Proc R Soc Lon Ser-A, 243 (1957) 190-205.
23. J. A. Greenwood, and J. B. P. Williamson, *Contact of Nominally Flat Surfaces*, J. B. P. Proc. R. Soc. London A, 295 (1966).
24. J. A. Greenwood, J. H. Tripp, *The contact of two nominally flat rough surfaces*, Proc. Inst. Mech. Eng., 185 (1970, 1971).
25. W. R. Chang, I. Etsion, and D. B. Bogy, *An elastic–plastic model for the contact of rough surfaces*, J. Tribol. Trans. ASME 109 (1987).
26. W. R. Chang, I. Etsion, and D. B. Bogy, *Static friction coefficient model for metallic rough surfaces*, J. Tribol. Trans. ASME 110 (1988).
27. D. G. Evseev, B. M. Medvedev, and G. G. Grigoriyan, *Modification of the Elastic-Plastic model for the contact of rough surfaces*, Wear, 150 (1991).
28. W.-R. Chang, *An elastic-plastic contact model for a rough surface with an ion-plated soft metallic coating*, Wear, 212 (1997).
29. L. Kogut, and I. Etsion, *The Contact of a Compliant Curved and a Nominally Flat Rough Surfaces*, Trib. Trans., 43 (2000).

30. N. Yu, and A. A. Polycarpou, *Contact of Rough Surfaces with Asymmetric Distribution of Asperity Heights*, ASME Jour. of Trib., 124 (2002).
31. L. Kogut, and I. Estion, *Elastic–plastic Contact Analysis of a Sphere and Rigid Flat*, Trans. ASME J. Appl. Mech., 69 (2002).
32. L. Kpgut, and I. Etsion, *A finite element based elastic–plastic model for the contact of rough surfaces*, Tribol. Trans., 46 (2003).
33. K. L. Johnson, *contact mechanics*, Cambridge University Press, Cambridge, UK, 2001.
34. W. C. Wake, *Adhesion and the formulation of adhesives*, Sec. Ed., Applied Science Publishers, London,, 1982.
35. M. G. Scherge, S. N., *Biological Micro- and Nanotribology*, Springer, Berlin, (2001).
36. K. L. Johnson, K. L. Kendall, and A. D. Roberts, *Surface energy and the contact of elastic solids*, Proc. R. Soc. London A, 324 (1971).
37. B. V. Derjaguin, V. M. Muller, and Y. P. Toporov, *Effect of contact deformations on the adhesion of particles*, J. Colloid Interf. Sci., 53 (1975).
38. D. Maugis, and H. M. Pollock, *Surface Forces, Deformation and Adherence at Metal Microcontacts*, Acta Metall Mater, 32 (1984) 1323-1334.
39. D. M. Schaefer, M. Carpenter, R. Reifenberger, L. P. Demejo, and D. S. Rimai, *Surface Force Interactions between Micrometer-Size Polystyrene Spheres and Silicon Substrates Using Atomic-Force Techniques*, J Adhes Sci Technol, 8 (1994) 197-210.
40. S. Biggs, and G. Spinks, *Atomic force microscopy investigation of the adhesion between a single polymer sphere and a flat surface*, J Adhes Sci Technol, 12 (1998) 461-478.
41. B. Gady, R. Reifenberger, D. M. Schaefer, R. C. Bowen, D. S. Rimai, L. P. Demejo, and W. Vreeland, *Particle adhesion to elastomeric substrates and elastomeric substrates with semi-rigid coatings*, J Adhesion, 67 (1998) 19-36.
42. M. Reitsma, V. S. J. Craig, and S. Biggs, *Measurement of the adhesion of a viscoelastic sphere to a flat non-compliant substrate*, J Adhesion, 74 (2000) 125-142.
43. M. Reitsma, V. Craig, and S. Biggs, *Elasto-plastic and visco-elastic deformations of a polymer sphere measured using colloid probe and scanning electron microscopy*, Int J Adhes Adhes, 20 (2000) 445-448.
44. L. O. Heim, J. Blum, M. Preuss, and H. J. Butt, *Adhesion and friction forces between spherical micrometer-sized particles*, Phys Rev Lett, 83 (1999) 3328-3331.

45. S. Ecke, R. Raiteri, E. Bonaccurso, C. Reiner, H. J. Deiseroth, and H. J. Butt, *Measuring normal and friction forces acting on individual fine particles*, Rev Sci Instrum, 72 (2001) 4164-4170.

46. D. Tabor, *Surface Forces and Surface Interactions*, J Colloid Interf Sci, 58 (1977) 2-13.

47. B. J. Briscoe, and S. S. Panesar, *The Effect of Surface-Topography on the Adhesion of Poly(Urethane) Metal Contacts*, J Phys D Appl Phys, 25 (1992) A20-A27.

48. H. Krupp, *Particle Adhesion Theory and Experiment*, Adv. Colloid Interface Sci., 1 (1967) 111.

49. H. A. Mizes, *Advances in Particles Adhesion (D. S. Ramani and L.H. Sharpe, Eds.)*, Gordon & Breach, Sydney, 1996.

50. H. Rumpf, *Particle Technology*, Chapman & Hall, London/New York, 1990.

51. B. V. Derjaguin, Kolloid, Z. 69 (1934).

52. A. A. Polycarpou, and N. Yu, *Adhesive contact based on the Lennard-Jones potential: a correction to the value of the equilibrium distance as used in the potential*, J Colloid Interf Sci, 278 (2004) 428-435.

53. Y. I. Rabinovich, J. J. Adler, A. Ata, R. K. Singh, and B. M. Moudgil, *Adhesion between nanoscale rough surfaces - I. Role of asperity geometry*, J Colloid Interf Sci, 232 (2000) 10-16.

54. Y. I. Rabinovich, J. J. Adler, A. Ata, R. K. Singh, and B. M. Moudgil, *Adhesion between nanoscale rough surfaces - II. Measurement and comparison with theory*, J Colloid Interf Sci, 232 (2000) 17-24.

55. J. Katainen, M. Paajanen, E. Ahtola, V. Pore, and J. Lahtinen, *Adhesion as an interplay between particle size and surface roughness*, J Colloid Interf Sci, 304 (2006) 524-529.

56. Y. Ando, and J. Ino, *Friction and pull-off force on silicon surface modified by FIB*, Sensor Actuat a-Phys, 57 (1996) 83-89.

57. E. R. Beach, G. W. Tormoen, J. Drelich, and R. Han, *Pull-off force measurements between rough surfaces by atomic force microscopy*, J Colloid Interf Sci, 247 (2002) 84-99.

58. M. S. Esayanur, S. B. Yeruva, Y. I. Rabinovich, and B. M. Moudgil, *Interaction force measurements using atomic force microscopy for characterization and control of adhesion, dispersion and lubrication in particulate systems*, J Adhes Sci Technol, 19 (2005) 611-626.

59. K. Meine, K. Kloss, T. Schneider, and D. Spaltmann, *The influence of surface roughness on the adhesion force*, Surf Interface Anal, 36 (2004) 694-697.

60. A. Mendez-Vilas, M. L. Gonzalez-Martin, L. Labajos-Broncano, and M. J. Nuevo, *Experimental analysis of the influence of surface topography on the adhesion force as measured by an AFM*, J Adhes Sci Technol, 16 (2002) 1737-1747.

61. D. M. Schaefer, M. Carpenter, B. Gady, R. Reifenberger, L. P. Demejo, and D. S. Rimai, *Surface-Roughness and Its Influence on Particle Adhesion Using Atomic-Force Techniques*, J Adhes Sci Technol, 9 (1995) 1049-1062.

62. G. W. Tormoen, J. Drelich, and J. Nalaskowski, *A distribution of AFM pull-off forces for glass microspheres on a symmetrically structured rough surface*, J Adhes Sci Technol, 19 (2005) 215-234.

63. S. Yang, H. Zhang, and S. M. Hsu, *Correction of random surface roughness on colloidal probes in measuring adhesion*, Langmuir, 23 (2007) 1195-1202.

64. D. L. Liu, J. Martin, and N. A. Burnham, *Optimal roughness for minimal adhesion*, Appl Phys Lett, 91 (2007).

65. S. N. Ramakrishna, L. Y. Clasohm, A. Rao, and N. D. Spencer, *Controlling Adhesion Force by Means of Nanoscale Surface Roughness*, Langmuir, 27 (2011) 9972-9978.

66. W. A. Ducker, T. J. Senden, and R. M. Pashley, *Direct Measurement of Colloidal Forces Using an Atomic Force Microscope*, Nature, 353 (1991) 239-241.

67. J. A. Greenwood, and D. Tabor, *The Friction of Hard Sliders on Lubricated Rubber - the Importance of Deformation Losses*, P Phys Soc Lond, 71 (1958) 989-1001.

68. E. J. Abbott, and F. A. Pirestone, *Specifying surface quantity – a method based on accurate measurement and comparison*, Mech. Eng., 55 (1933).

69. G. M. Hamilton, Proc. Instn. Mech. Engrs. , 197 (1983).

70. R. Jackson, and I. Green, *A Finite Element Study of Elasto-Plastic Hemispherical Contact Against a Rigid Flat*, ASME Jour. of Trib., 127 (2005).

71. R. Jackson, and I. Green, *A Statistical Model of Elasto-Plastic Asperity Contact of Rough Surfaces*, Tribol. Int., 39 (2006).

72. J. F. Molinari, L. Pei, S. Hyun, and M. O. Robbins, *Finite element modeling of elasto-plastic contact between rough surfaces*, J Mech Phys Solids, 53 (2005) 2385-2409.

73. J. Abdo, and K. Farhang, *Elastic-plastic contact model for rough surfaces based on plastic asperity concept*, Int J Nonlinear Mech, 40 (2005) 495-506.

74. A. Hariri, J. W. Zu, and R. Ben Mrad, *Modeling of elastic/plastic contact between nominally flat rough surfaces using an n-point asperity model*, J Tribol-T Asme, 128 (2006) 876-885.

75. G. G. Adams, and H. Eid, *An elastic-plastic finite element analysis of interacting asperities in contact with a rigid flat*, J Phys D Appl Phys, 40 (2007) 7432-7439.

76. F. S. Wang, J. M. Block, W. W. Chen, A. Martini, K. Zhou, L. M. Keer, and Q. J. Wang, *A Multilevel Model for Elastic-Plastic Contact Between a Sphere and a Flat Rough Surface*, J Tribol-T Asme, 131 (2009).

77. A. A. Polycarpou, C. D. Yeo, and R. R. Katta, *Improved Elastic Contact Model Accounting for Asperity and Bulk Substrate Deformation*, Tribol Lett, 35 (2009) 191-203.

78. S. Ilincic, G. Vorlaufer, P. A. Fotiu, A. Vernes, and F. Franek, *Combined finite element-boundary element method modelling of elastic multi-asperity contacts*, P I Mech Eng J-J Eng, 223 (2009) 767-776.

79. A. Sepehri, and K. Farhang, *Closed-Form Equations for Three Dimensional Elastic-Plastic Contact of Nominally Flat Rough Surfaces*, J Tribol-T Asme, 131 (2009).

80. L. Kogut, and I. Etsion, *A Semi-Analytical Solution for the Sliding Inception of a Spherical Contact*, J. of Tribo., 125 (2003).

81. V. Brizmer, Y. Kligerman and I. Etsion, *Elastic-Plastic Spherical Contact under Combined Normal and Tengential Loading in Full Stick*, Tribol. Lett., 25 (2006).

82. I. Etsion, A. Ovcharenko, and G. Halperin, *Experimental study of adhesive static friction in a spherical elastic-plastic contact*, J Tribol-T Asme, 130 (2008).

83. Y. K. D. Cohen, and I. Etsion, *The Effect of Surface Roughness on Static Friction and Junction Growth of an Elastic-Plastic Spherical Contact*, J. of Tribo., 131 (2009).

84. D. Cohen, Y. Kligerman, and I. Etsion, *A model for contact and static friction of nominally flat rough surfaces under full stick contact condition*, J Tribol-T Asme, 130 (2008).

85. L. Li, I. Etsion, and F. E. Talke, *Contact Area and Static Friction of Rough Surfaces With High Plasticity Index*, J Tribol-T Asme, 132 (2010).

86. N. Yu, S. R. Pergande, and A. A. Polycarpou, *Static friction model for rough surfaces with asymmetric distribution of asperity heights*, J Tribol-T Asme, 126 (2004) 626-629.

87. L. Chang, and H. Zhang, *A mathematical model for frictional elastic-plastic sphere-on-flat contacts at sliding incipient*, J Appl Mech-T Asme, 74 (2007) 100-106.

88. E. L. Deladi, M. B. de Rooij, and D. J. Schipper, *Modelling of static friction in rubber-metal contact*, Tribol Int, 40 (2007) 588-594.

89. Y. R. Jeng, and S. R. Peng, *Static Friction Model of Elastic-Plastic Contact Behavior of Surface With Elliptical Asperities*, J Tribol-T Asme, 131 (2009).

90. W. W. Chen, and Q. J. Wang, *A Numerical Static Friction Model for Spherical Contacts of Rough Surfaces, Influence of Load, Material, and Roughness*, J Tribol-T Asme, 131 (2009).

91. A. C. Frisher-Cripps, *Nanoindentation*, Springer, New York, 2004.

92. A. Gouldstone, N. Chollacoop, M. Dao, J. Li, A. M. Minor, and Y. L. Shen, *Indentation across size scales and disciplines: Recent developments in experimentation and modeling*, Acta Mater, 55 (2007) 4015-4039.

93. S. E. Flores, M. G. Pontin, and F. W. Zok, *Scratching of Elastic/Plastic Materials With Hard Spherical Indenters*, J Appl Mech-T Asme, 75 (2008).

94. S. D. Mesarovic, and N. A. Fleck, *Spherical indentation of elastic-plastic solids*, P Roy Soc Lond a Mat, 455 (1999) 2707-2728.

95. S. Labdi, A. Jellad, and O. Maciejak, *Loading rate effect on lateral force measurements on nanostructured Ti and TiN thin films*, Surf Coat Tech, 201 (2006) 113-119.

96. C. J. Wong, and J. C. M. Li, *Wear Behavior of an Amorphous Alloy*, Wear, 98 (1984) 45-61.

97. T. Imura, K. Hasegawa, M. Moori, T. Nishiwaki, M. Takagi, and Y. Kawamura, *Cyclic Deformation and Tribological Behavior of an Amorphous Iron-Based Alloy Film*, Mat Sci Eng a-Struct, 133 (1991) 332-336.

98. E. Rabinowicz, *Friction and wear of materials*, New York, Wiley, 1965.

99. A. M. Hodge, and T. G. Nieh, *Evaluating abrasive wear of amorphous alloys using nanoscratch technique*, Intermetallics, 12 (2004) 741-748.

100. Y. J. Huang, Y. L. Chiu, J. Shen, Y. Sun, and J. J. J. Chen, *Mechanical performance of metallic glasses during nanoscratch tests*, Intermetallics, 18 (2010) 1056-1061.

101. R. Gassilloud, C. Ballif, P. Gasser, G. Buerki, and J. Michler, *Deformation mechanisms of silicon during nanoscratching*, Phys Status Solidi A, 202 (2005) 2858-2869.

102. B. J. Briscoe, E. Pelillo, and S. K. Sinha, *Scratch hardness and deformation maps for polycarbonate and polyethylene*, Polym Eng Sci, 36 (1996) 2996-3005.

103. H. A. Samra, A. Kumar, J. Xia, T. Staedler, X. Jiang, R. Verucchi, and I. Aronov, *Development of a new generation of amorphous hard coatings based on the Si-B-C-N-O system for applications in extreme condition* in: Surface Engineering, 2011.

104. B. G. Prevo, and O. D. Velev, *Controlled, rapid deposition of structured coatings from micro- and nanoparticle suspensions*, Langmuir, 20 (2004) 2099-2107.

105. Y. Wang, L. Chen, H. Yang, Q. Guo, W. Zhou, and M. Tao, *Spherical antireflection coatings by large-area convective assembly of monolayer silica microspheres*, Sol Energ Mat Sol C, 93 (2009) 85-91.

106. P. K. Hansma, V. B. Elings, O. Marti, and C. E. Bracker, *Scanning Tunneling Microscopy and Atomic Force Microscopy - Application to Biology and Technology*, Science, 242 (1988) 209-216.

107. D. A. Walters, J. P. Cleveland, N. H. Thomson, P. K. Hansma, M. A. Wendman, G. Gurley, and V. Elings, *Short cantilevers for atomic force microscopy*, Rev Sci Instrum, 67 (1996) 3583-3590.

108. C. A. Clifford, and M. P. Seah, *The determination of atomic force microscope cantilever spring constants via dimensional methods for nanomechanical analysis*, Nanotechnology, 16 (2005) 1666-1680.

109. G. A. Matei, E. J. Thoreson, J. R. Pratt, D. B. Newell, and N. A. Burnham, *Precision and accuracy of thermal calibration of atomic force microscopy cantilevers*, Rev Sci Instrum, 77 (2006).

110. J. E. Sader, and L. White, *Theoretical-Analysis of the Static Deflection of Plates for Atomic-Force Microscope Applications*, J Appl Phys, 74 (1993) 1-9.

111. J. M. Neumeister, and W. A. Ducker, *Lateral, Normal, and Longitudinal Spring Constants of Atomic-Force Microscopy Cantilevers*, Rev Sci Instrum, 65 (1994) 2527-2531.

112. Y. I. Rabinovich, and R. H. Yoon, *Use of Atomic-Force Microscope for the Measurements of Hydrophobic Forces between Silanated Silica Plate and Glass Sphere*, Langmuir, 10 (1994) 1903-1909.

113. D. Scholl, M. P. Everson, and R. C. Jaklevic, *In-Situ Force Calibration of High Force-Constant Atomic-Force Microscope Cantilevers*, Rev Sci Instrum, 65 (1994) 2255-2257.

114. C. T. Gibson, G. S. Watson, and S. Myhra, *Determination of the spring constants of probes for force microscopy/spectroscopy*, Nanotechnology, 7 (1996) 259-262.

115. A. Torii, M. Sasaki, K. Hane, and S. Okuma, *A method for determining the spring constant of cantilevers for atomic force microscopy*, Meas Sci Technol, 7 (1996) 179-184.

116. M. Tortonese, and M. Kirk, *Characterization of application specific probes for SPMs*, Proc. SPIE, 3009 (1997).

117. J. D. Holbery, V. L. Eden, M. Sarikaya, and R. M. Fisher, *Experimental determination of scanning probe microscope cantilever spring constants utilizing a nanoindentation apparatus*, Rev Sci Instrum, 71 (2000) 3769-3776.

118. R. S. Gates, and J. R. Pratt, *Prototype cantilevers for SI-traceable nanonewton force calibration*, Meas Sci Technol, 17 (2006) 2852-2860.

119. M. G. Reitsma, *Lateral force microscope calibration using a modified atomic force microscope cantilever*, Rev Sci Instrum, 78 (2007).

120. E. D. Langlois, G. A. Shaw, J. A. Kramar, J. R. Pratt, and D. C. Hurley, *Spring constant calibration of atomic force microscopy cantilevers with a piezosensor transfer standard*, Rev Sci Instrum, 78 (2007).

121. J. L. Hutter, and J. Bechhoefer, *Calibration of Atomic-Force Microscope Tips*, Rev Sci Instrum, 64 (1993) 1868-1873.

122. T. J. Senden, and W. A. Ducker, *Experimental-Determination of Spring Constants in Atomic-Force Microscopy*, Langmuir, 10 (1994) 1003-1004.

123. J. P. Cleveland, S. Manne, D. Bocek, and P. K. Hansma, *A Nondestructive Method for Determining the Spring Constant of Cantilevers for Scanning Force Microscopy*, Rev Sci Instrum, 64 (1993) 403-405.

124. H. J. Butt, P. Siedle, K. Seifert, K. Fendler, T. Seeger, E. Bamberg, A. L. Weisenhorn, K. Goldie, and A. Engel, *Scan Speed Limit in Atomic Force Microscopy*, J Microsc-Oxford, 169 (1993) 75-84.

125. Z. C. Ying, M. G. Reitsma, and R. S. Gates, *Direct measurement of cantilever spring constants and correction for cantilever irregularities using an instrumented indenter*, Rev Sci Instrum, 78 (2007).

126. H. J. Butt, and M. Jaschke, *Calculation of Thermal Noise in Atomic-Force Microscopy*, Nanotechnology, 6 (1995) 1-7.

127. R. Proksch, T. E. Schaffer, J. P. Cleveland, R. C. Callahan, and M. B. Viani, *Finite optical spot size and position corrections in thermal spring constant calibration*, Nanotechnology, 15 (2004) 1344-1350.

128. T. E. Schaffer, *Calculation of thermal noise in an atomic force microscope with a finite optical spot size*, Nanotechnology, 16 (2005) 664-670.

129. R. G. Cain, N. W. Page, and S. Biggs, *Microscopic and macroscopic effects of surface lubricant films in granular shear*, Phys Rev E, 62 (2000) 8369-8379.

130. I. C. H. Berg, M. W. Rutland, and T. Arnebrant, *Lubricating properties of the initial salivary pellicle - an AFM Study*, Biofouling, 19 (2003) 365-369.

131. M. Varenberg, I. Etsion, and G. Halperin, *Nanoscale fretting wear study by scanning probe microscopy*, Tribology Letters, 18 (2005) 493-498.

132. A. A. Feiler, P. Jenkins, and M. W. Rutland, *Effect of relative humidity on adhesion and frictional properties of micro- and nano-scopic contacts*, J Adhes Sci Technol, 19 (2005) 165-179.

133. T. Pettersson, A. Naderi, R. Makuska, and P. M. Claesson, *Lubrication properties of bottle-brush polyelectrolytes: An AFM study on the effect of side chain and charge density*, Langmuir : the ACS journal of surfaces and colloids, 24 (2008) 3336-3347.

134. M. Cardenas, J. J. Valle-Delgado, J. Hamit, M. W. Rutland, and T. Arnebrant, *Interactions of hydroxyapatite surfaces: Conditioning films of human whole saliva*, Langmuir : the ACS journal of surfaces and colloids, 24 (2008) 7262-7268.

135. S. J. Oshea, M. E. Welland, and T. Rayment, *Atomic Force Microscope Study of Boundary-Layer Lubrication*, Appl Phys Lett, 61 (1992) 2240-2242.

136. R. G. Cain, S. Biggs, and N. W. Page, *Force calibration in lateral force microscopy*, J Colloid Interf Sci, 227 (2000) 55-65.

137. R. W. Carpick, D. F. Ogletree, and M. Salmeron, *Lateral stiffness: A new nanomechanical measurement for the determination of shear strengths with friction force microscopy*, Appl Phys Lett, 70 (1997) 1548-1550.

138. M. A. Lantz, S. J. OShea, A. C. F. Hoole, and M. E. Welland, *Lateral stiffness of the tip and tip-sample contact in frictional force microscopy*, Appl Phys Lett, 70 (1997) 970-972.

139. E. Liu, B. Blanpain, and J. P. Celis, *Calibration procedures for frictional measurements with a lateral force microscope*, Wear, 192 (1996) 141-150.

140. G. Bogdanovic, A. Meurk, and M. W. Rutland, *Tip friction - torsional spring constant determination*, Colloid Surface B, 19 (2000) 397-405.

141. A. Feiler, P. Attard, and I. Larson, *Calibration of the torsional spring constant and the lateral photodiode response of frictional force microscopes*, Rev Sci Instrum, 71 (2000) 2746-2750.

142. D. F. Ogletree, R. W. Carpick, and M. Salmeron, *Calibration of frictional forces in atomic force microscopy*, Rev Sci Instrum, 67 (1996) 3298-3306.

143. I. E. M. Varenberg, and G. Halperin, *An improved wedge calibration method for lateral force in atomic force microcopy*, Rev. Sci. Instrum., 74 (2003).

144. H. A. Rothbart, *Mechanical Design Handbook*, McGraw-Hill, New York, 1996.

145. H. A. Samra, A. Kumar, J. Xia, T. Staedler, X. Jiang, R. Verucchi, and I. Aronov, *Development of a new generation of amorphous hard coatings based on the Si-B-C-N-O system for applications in extreme condition* in: Surface Engineering, 2011.

146. G. M. Oliver, and W. C. Pharr, *An Improved Technique for determining hardness and elastic modulus using load and displacement sensing indentation experiments*, J. Mater. Res. , 7 (1992).

147. F. J. Li, S. Zhang, J. H. Kong, Y. J. Zhang, and W. L. Zhang, *Multilayer DLC coatings via alternating bias during magnetron sputtering*, Thin Solid Films, 519 (2011) 4910-4916.

148. S. Zhang, X. L. Bui, Y. Q. Fu, D. L. Butler, and H. Du, *Bias-graded deposition of diamond-like carbon for tribological applications*, Diam Relat Mater, 13 (2004) 867-871.

149. D. L. Joslin, and W. C. Oliver, *A New Method for Analyzing Data from Continuous Depth-Sensing Microindentation Tests*, J Mater Res, 5 (1990) 123-126.

150. R. Saha, and W. D. Nix, *Effects of the substrate on the determination of thin film mechanical properties by nanoindentation*, Acta Mater, 50 (2002) 23-38.

151. K. Kendall, N. M. Alford, and J. D. Birchall, *A New Method for Measuring the Surface-Energy of Solids*, Nature, 325 (1987) 794-796.

152. R. G. Horn, D. T. Smith, and W. Haller, *Surface Forces and Viscosity of Water Measured between Silica Sheets*, Chem Phys Lett, 162 (1989) 404-408.

153. C. J. Vanoss, M. K. Chaudhury, and R. J. Good, *Monopolar Surfaces*, Adv Colloid Interfac, 28 (1987) 35-64.

154. C. J. Vanoss, M. K. Chaudhury, and R. J. Good, *Interfacial Lifshitz-Vanderwaals and Polar Interactions in Macroscopic Systems*, Chem Rev, 88 (1988) 927-941.

155. C. Jacquot, and J. Takadoum, *A study of adhesion forces by atomic force microscopy*, J Adhes Sci Technol, 15 (2001) 681-687.

156. F. P. Bowden, and D.Tabor, *The Friction and Lubrication of Solids*, Oxford univ. Press, Oxford, 1958.

157. E. S. Yoon, R. A. Singh, H. J. Oh, and H. Kong, *The effect of contact area on nano/micro-scale friction*, Wear, 259 (2005) 1424-1431.

158. K. L. Johnson, K. Kendall, and A. D. Roberts, *Surface Energy and Contact of Elastic Solids*, Proc R Soc Lon Ser-A, 324 (1971) 301.

159. B. Bhushan, and S. Sundararajan, *Micro/nanoscale friction and wear mechanisms of thin films using atomic force and friction force microscopy*, Acta Mater, 46 (1998) 3793-3804.

160. B. Bhushan, and C. Dandavate, *Thin-film friction and adhesion studies using atomic force microscopy*, J Appl Phys, 87 (2000) 1201-1210.

161. F. P Bowden, and D. Tabor, *The friction and lubrication of solids*, Clarendon Press, Oxford, 1950.

162. L. Kogut, and I. Etsion, *A Static Friction Model for Elastic-Plastic Contacting Rough Surfaces*, ASME Jour. of Trib., 126 (2004).

163. J. Skinner, and N. Gane, *Sliding Friction under a Negative Load*, J Phys D Appl Phys, 5 (1972) 2087.

Appendix

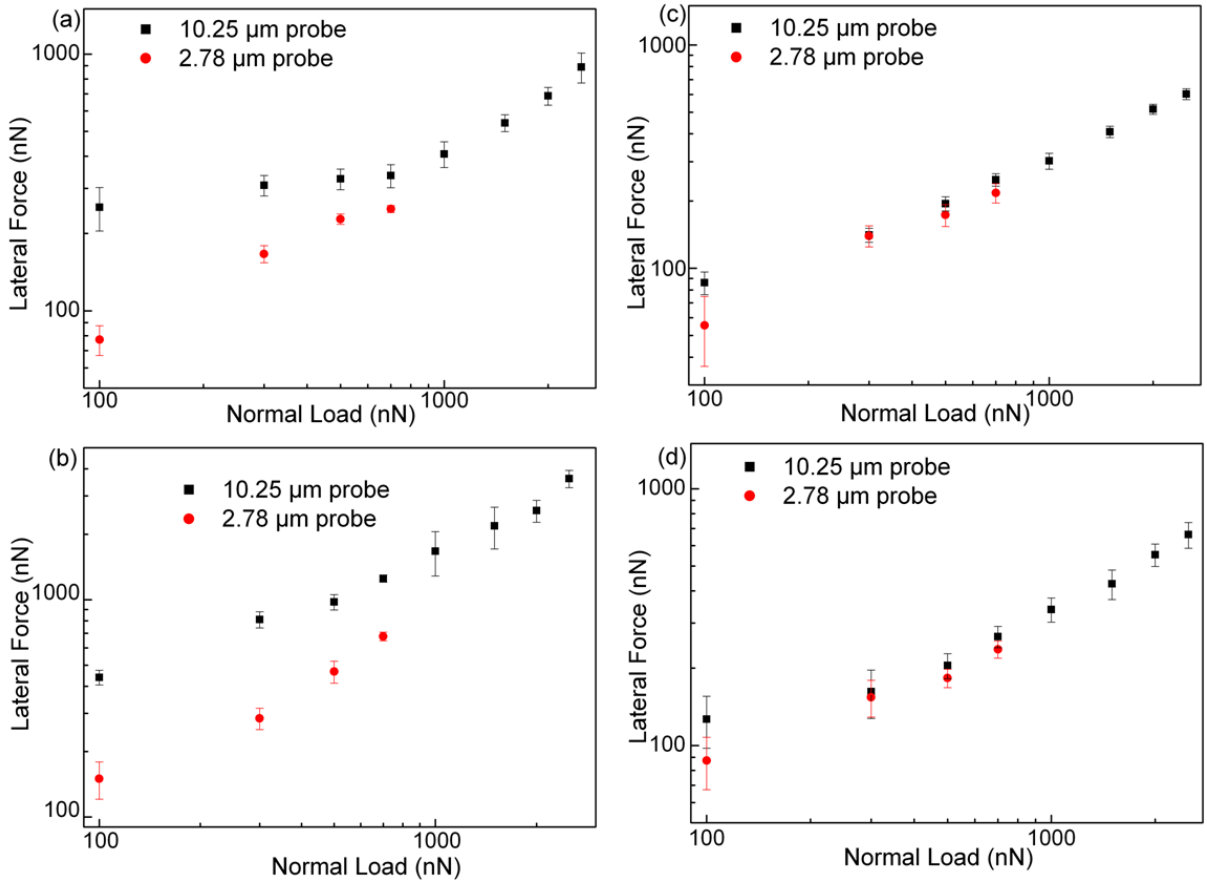

Figure A1: Logarithmic plot of lateral force vs. normal load for (a) silica, (b) aluminum, (c) smooth DLC, and (d) rough DLC using 2.78 and 10.25 µm colloidal probes. These results are obtained using AFM.

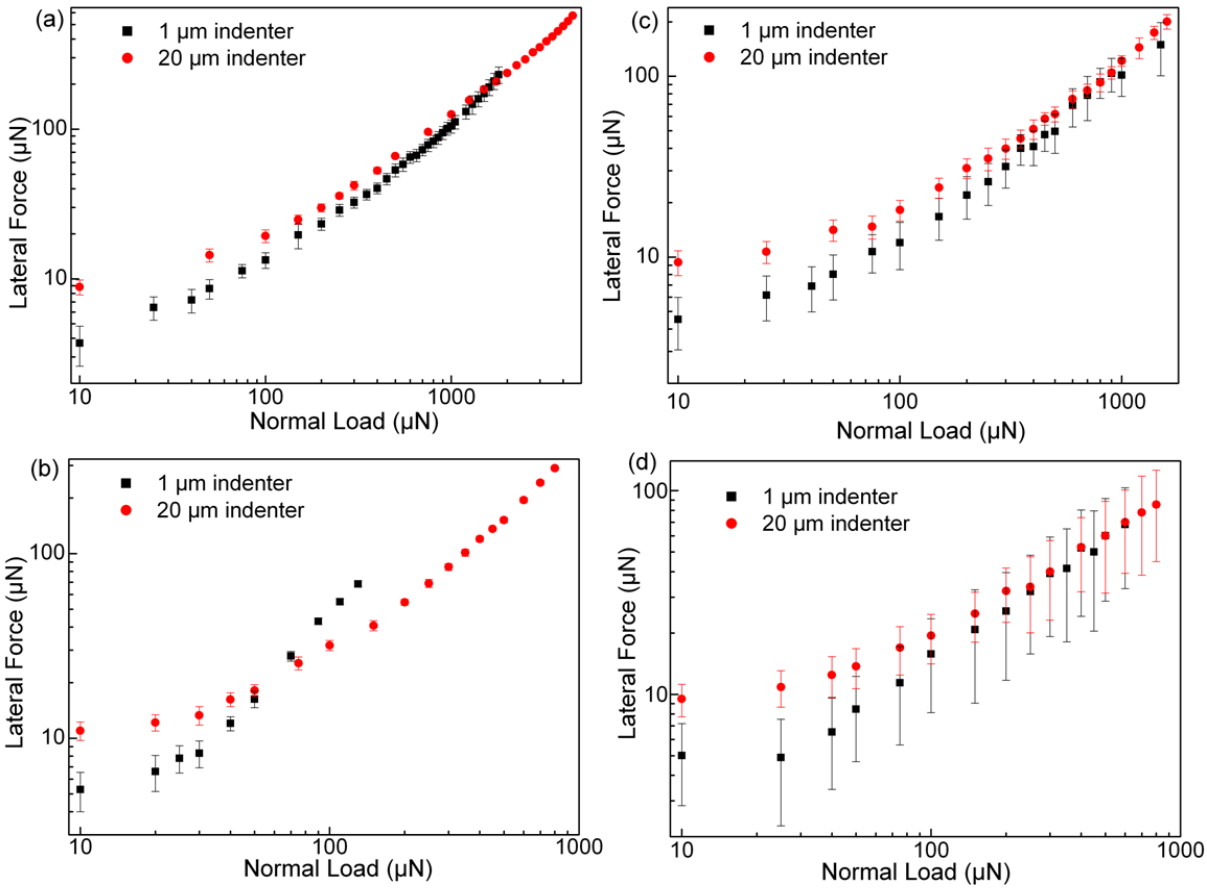

Figure A2: Logarithmic plot of lateral force vs. normal load for (a) silica, (b) aluminum, (c) smooth DLC, and (d) rough DLC using 1 and 20 μm diamond indenters. These results are obtained using Nanoindenter.

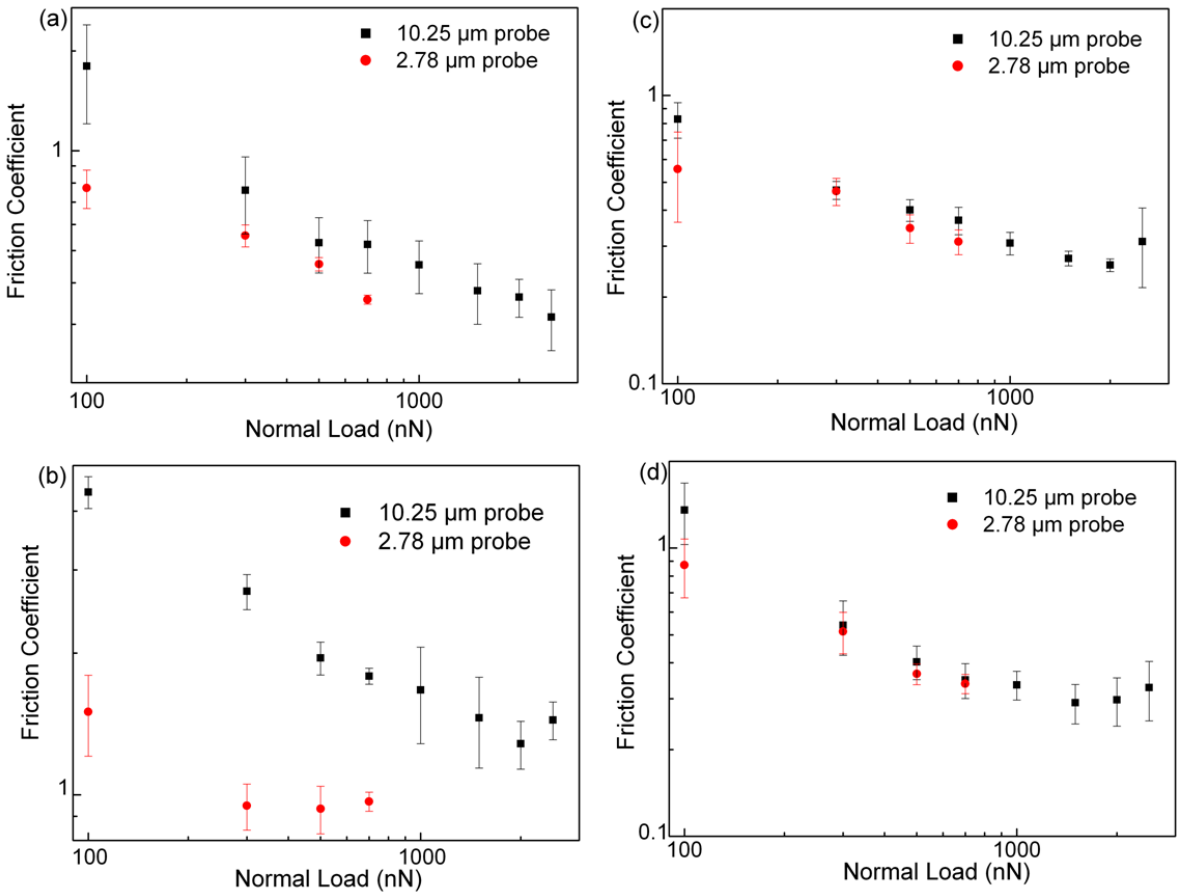

Figure A3: Logrithim plot of friction coefficient vs. normal load for (a) silica, (b) aluminum, (c) smooth DLC, and (d) rough DLC using 2.78 and 10.25 µm colloidal probes. These results are obtained using AFM.

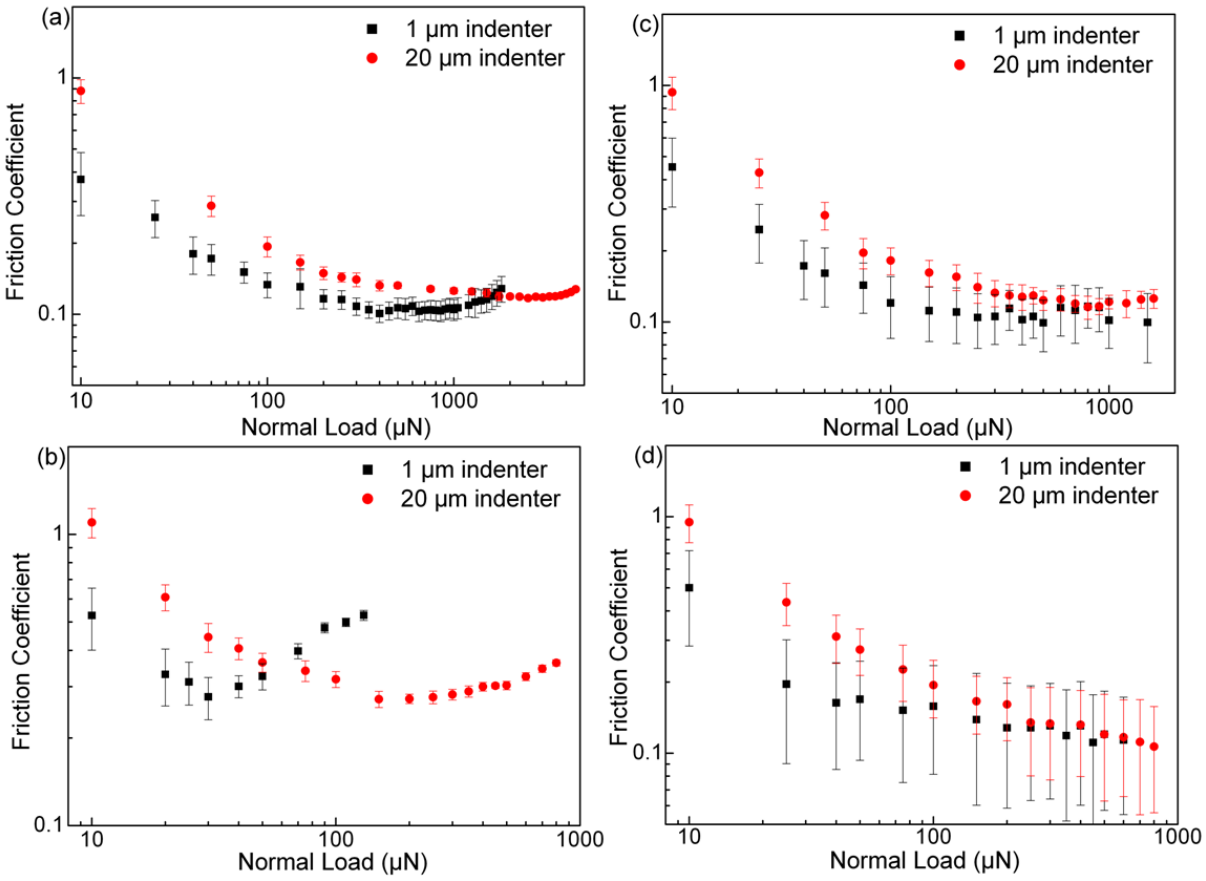

Figure A4: Logrithim plot of friction coefficient vs. normal load for (a) silica, (b) aluminum, (c) smooth DLC, and (d) rough DLC using 1 and 20 μm diamond indenters. These results are obtained using Nanoindenter.

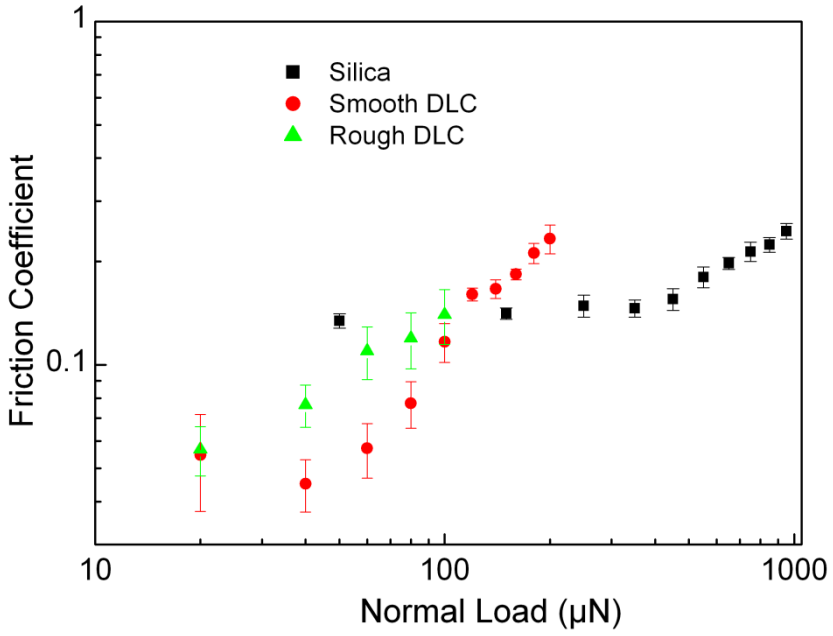

Figure A5: Friction coefficient vs. normal load at logarithmic scale for silica and DLCs samples derived with 1μm indenter.

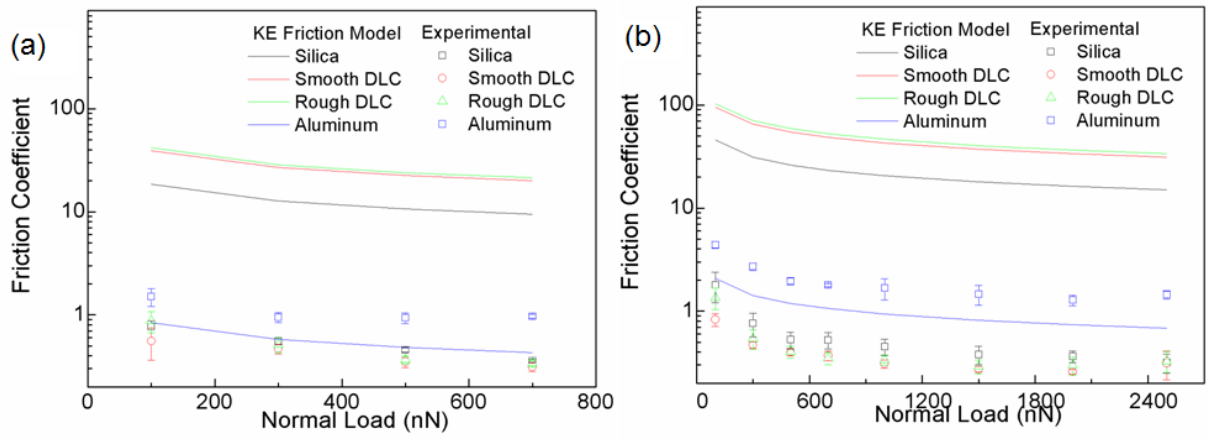

Figure A6: Comparision of the friction coefficient between theoritical (KE model) and experimenatal results for fused silica, and DLCs samples derived with (a) 2.78 µm and (b) 10.25 µm colloidal probes. These results are obtained using AFM.

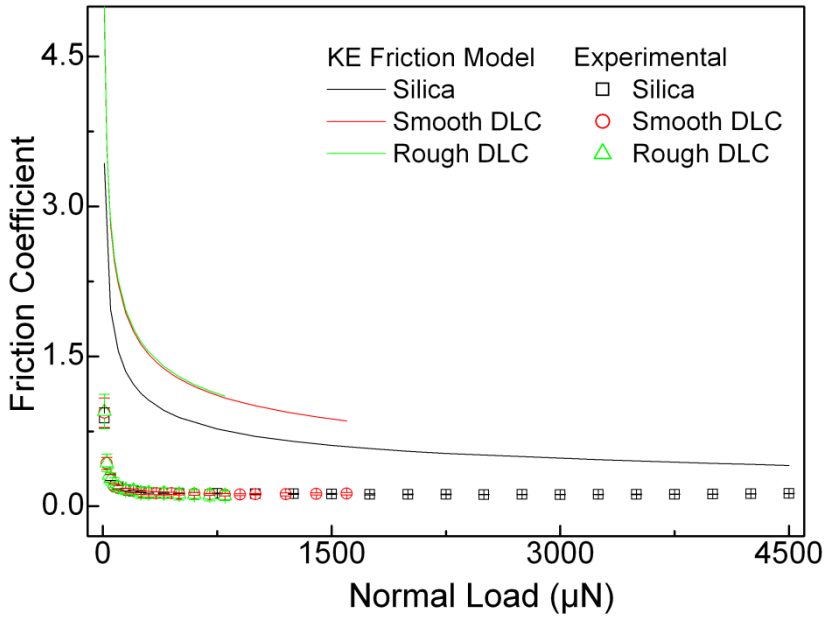

Figure A7: Comparision of the friction coefficient between theoritical (KE model) and experimenatal results for fused silica, and DLCs samples derived with 20 µm indenter. These results are obtained using Nanoindenter.

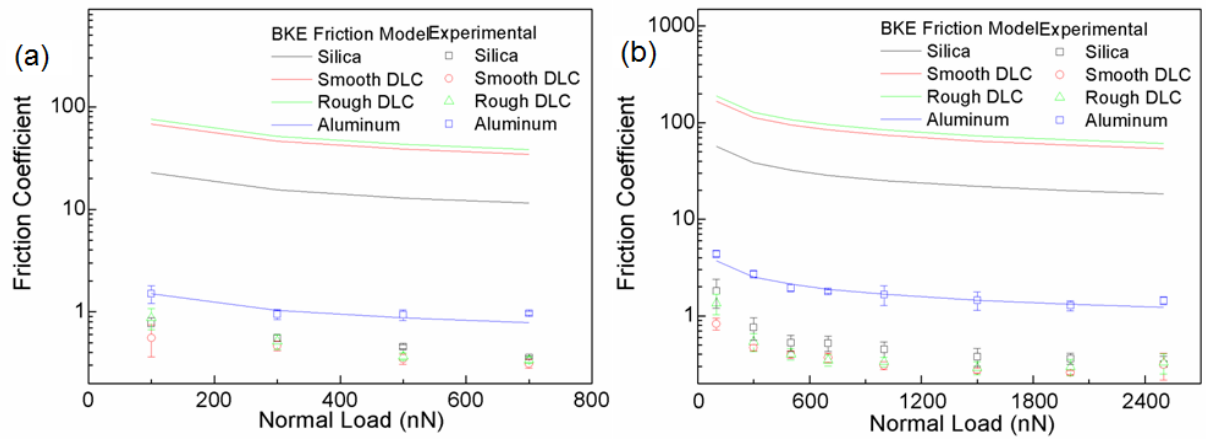

Figure A8: Comparision of the friction coefficient between theoritical (BKE model) and experimenatal results for silica, aluminum, and DLC samples derived with 2.78 and 10.25 µm colloidal probes. These results are obtained using AFM.

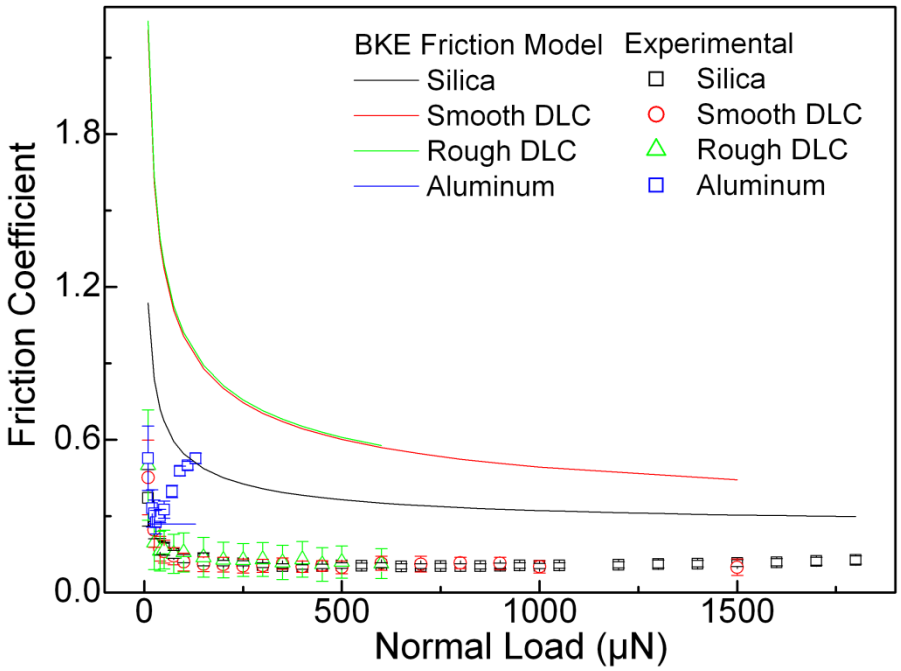

Figure A9. Comparision of the friction coefficient between theoritical (BKE model) and experimenatal results for fused silica, aluminum, and DLCs samples derived with 1 µm indenter. These results are obtained using Nanoindenter.

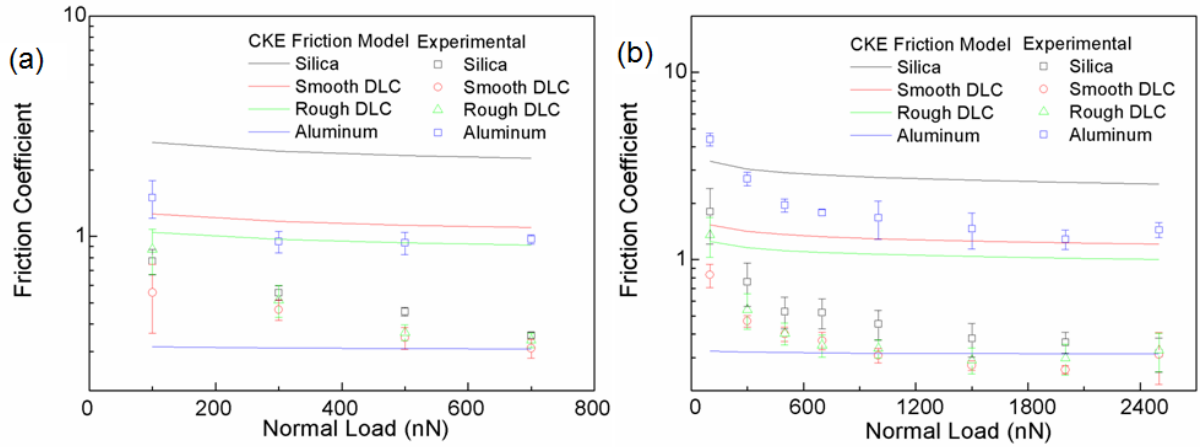

Figure A10: Comparision of the friction coefficient between theoritical (CKE model) and experimenatal results for silica, aluminum, and DLC samples derived with 2.78 and 10.25 µm colloidal probes. These results are obtained using AFM.

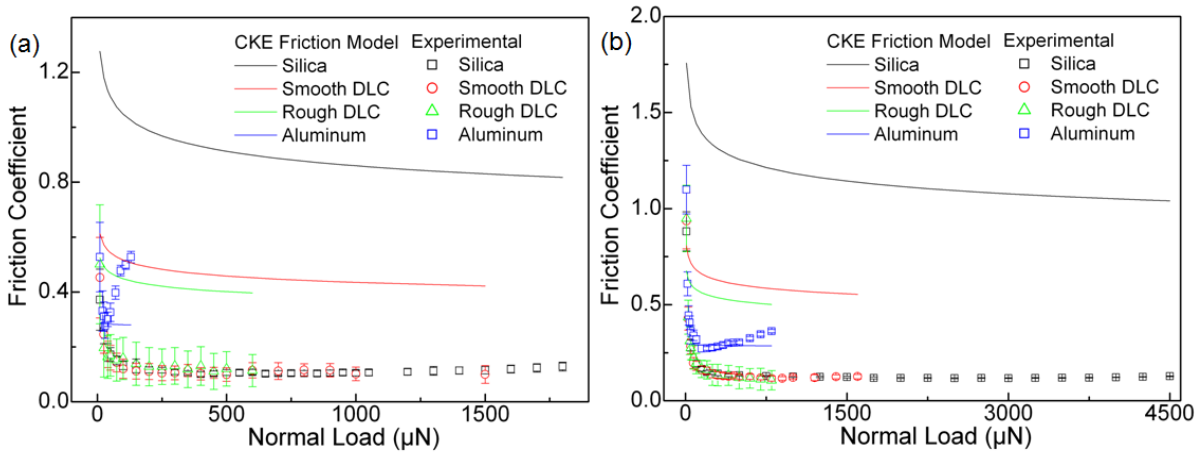

Figure A11: Comparision of the friction coefficient between theoritical (CKE model) and experimenatal results for fused silica, aluminum, and DLCs samples derived with (a) 1 µm indenter and (b) 20 µm indenter. These results are obtained using Nanoindenter.

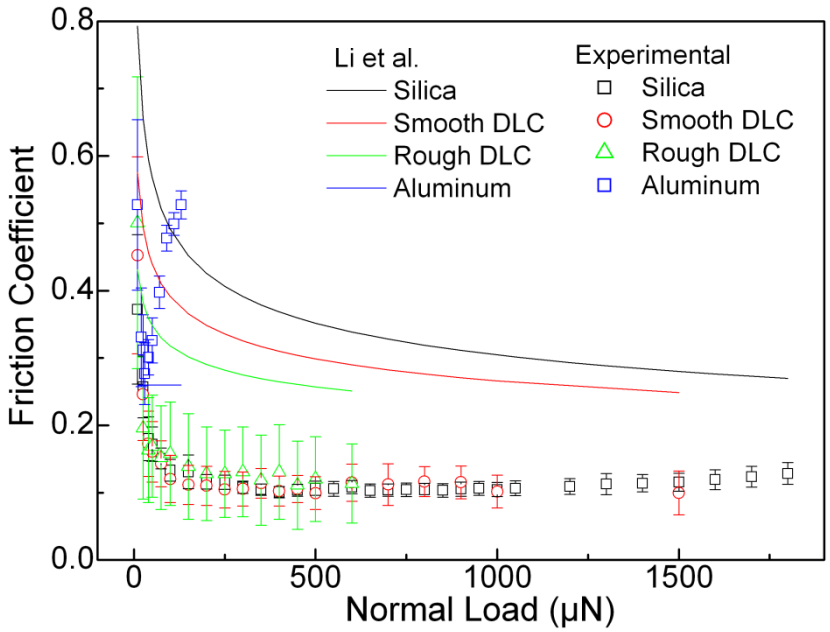

Figure A12: Comparision of the friction coefficient between theoritical (Li et al.) and experimenatal results for fused silica, aluminum, and DLCs samples derived with (a) 1 μm indenter and (b) 20 μm indenter. These results are obtained using Nanoindenter.

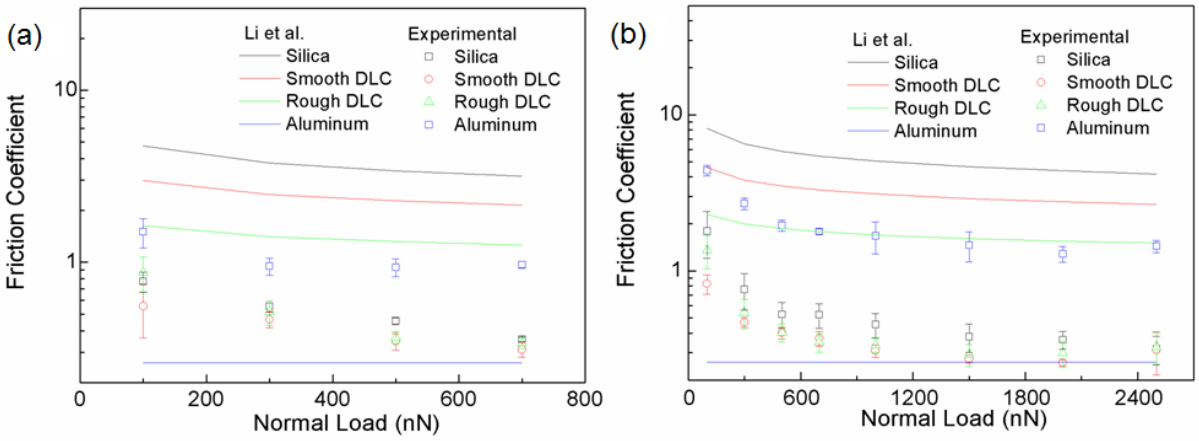

Figure A13: Comparision of the friction coefficient between theoritical (Li et al.) and experimenatal results for silica, aluminum, and DLC samples derived with 2.78 and 10.25 μm colloidal probes. These results are obtained using AFM.

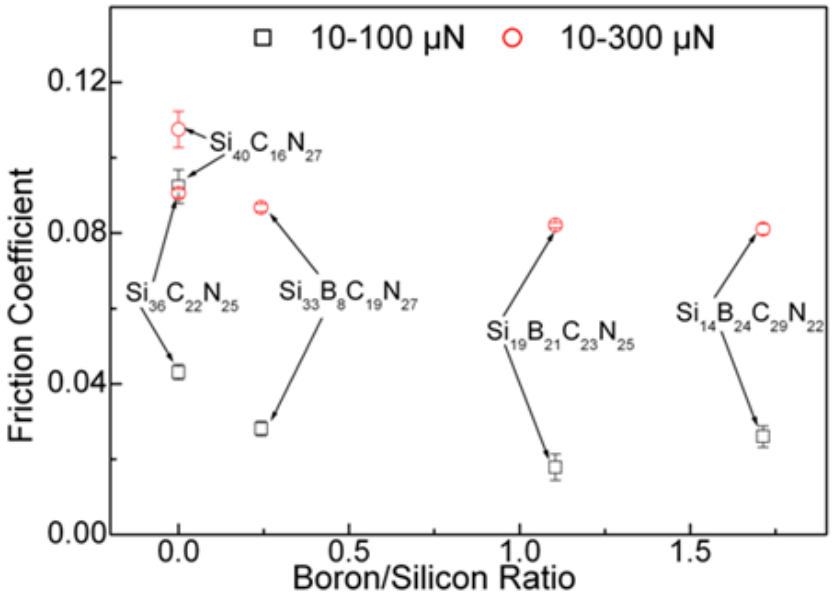

Figure A14: Friction coefficient of SiCN and SiCBN films.